A Particle Engineering Approach to the Development of Microparticles Suitable for Enteric Delivery of Biologics

by

Shabab Bin Karim

A thesis submitted in partial fulfillment of the requirements for the degree of

Master of Science

Department of Mechanical Engineering

University of Alberta

Abstract

Despite tremendous advances in the field of medical science, enteric infections still account for millions of deaths globally each year. Inaccessibility to clean drinking water, sanitation systems and proper healthcare infrastructure in developing parts of the world remains a huge obstacle to mitigating the impact of these infections. The emergence of antibiotic-resistant strains of bacteria and the insufficient development of new small-molecule antibiotics with which to combat them call for the exploration of new avenues in the treatment of infectious enteritis and serve as the main motivation behind this work. Delivering bacteriophages to the enteric region to act against invading bacteria can be a viable treatment option, but the survival of the phages through the mechanical and environmental stresses of processing conditions and then through the hostile chemical conditions of the stomach is a major problem to resolve. Using spray drying to create bacteriophage-carrying microparticles with a stabilizing core and a shell capable of withstanding shifts in pH is a potential solution to these issues. This thesis details the implementation of a particle engineering approach to understanding the previously unexplored particle formation process of Eudragit-trehalose microparticles using an improved monodisperse droplet chain. It then evaluates the effectiveness of the particle shells using a new shadowgraphic technique.

To gain a better understanding of the particle formation process, modifications were made to an existing monodisperse droplet chain instrument. Integrating interferometric laser imaging for droplet sizing into the instrument improved the reliability of initial droplet diameter measurement. The particle collection efficiency of the instrument was also improved by the addition of a custom-built single-nozzle impactor. Using the

information gathered from the instrument, initial droplet diameter can be measured with less than 1% error. The density of particles collected from the instrument can also be measured, but the accuracy depends heavily on the morphology of the particle. For spherical, solid particles like trehalose, the average density of the particle can be measured with only a small margin of error (<3%). However, for particles exhibiting irregular size and internal voids, density calculations may be subject to a significantly higher margin of error. Improved particle collection efficiency results in the accumulation of enough particles for macro-Raman spectroscopy measurements. These new modifications make the monodisperse droplet chain an effective tool for investigating particle formation processes and morphology prior to mass production for inhalable and oral administration.

Next, the monodisperse droplet chain and particle formation model were used to examine the formation process of Eudragit-trehalose composite microparticles from two different solvent systems — an ethanol-water co-solvent system and water. The results of this study showed that Eudragit formed the shell of the particles with trehalose as the core irrespective of the choice of solvent. The formulations were spray-dried and their survival in acidic and alkaline environments was studied using a new shadowgraphic imaging technique. The results showed that the outer shell made of Eudragit was capable of protecting the particles from extremely acidic pH. The trehalose core of the particles with >5% w/w Eudragit remained intact after one hour’s exposure at pH 2, a result that was verified by the Raman spectrum of the formulation cured from the acidic medium. The particles suspended in an alkaline medium showed slow dissolution,

indicating the time-dependent release pattern of the spray-dried particles and therefore their suitability for enteric delivery of biologics.

Preface

The research presented in this thesis is original work conducted under the supervision of Dr. Reinhard Vehring.

For the work detailed in Chapter 2, I was responsible for apparatus design and assembly, software code development, method development, design of experiment, data collection, data analysis, and chapter composition. Chester Jar helped with apparatus design and method development. Mani Ordoubadi assisted with method development, design of experiment and data analysis. Hui Wang provided important insight into apparatus design, method development and data analysis. Mellissa Gomez helped with apparatus design, data collection and data analysis. Isobel Tetreau aided in data analysis. Reinhard Vehring provided input concerning concept formation and discussion of results.

Chapter 3 of the thesis is a manuscript titled “On the Feasibility of Spray-Dried Eudragit-Trehalose Microparticles for Enteric Delivery of Biologics” submitted for publication under the coauthorship of Shabab Bin Karim, Mani Ordoubadi, Hui Wang, Mellissa Gomez and Reinhard Vehring. For this chapter, I was responsible for concept development, design of experiment, theoretical analysis, data collection, data analysis and manuscript composition. Mani Ordoubadi assisted with theoretical analysis, data analysis and manuscript editing. Hui Wang assisted with the design of experiment, data analysis and manuscript editing. Mellissa Gomez assisted with data collection and manuscript editing. Reinhard Vehring was the supervisory author and was involved in concept development, discussion of results and manuscript composition.

I met a traveller from an antique land
Who said: "Two vast and trunkless legs of stone
Stand in the desert . . . Near them, on the sand,
Half sunk, a shattered visage lies, whose frown,
And wrinkled lip, and sneer of cold command,
Tell that its sculptor well those passions read
Which yet survive, stamped on these lifeless things,
The hand that mocked them, and the heart that fed:
And on the pedestal these words appear:
'My name is Ozymandias, king of kings:
Look on my works, ye Mighty, and despair!'
Nothing beside remains. Round the decay
Of that colossal wreck, boundless and bare
The lone and level sands stretch far away."

"Ozymandias"
Percy Bysshe Shelley

To my beloved parents, A.K.M. Fazlul Karim Chowdhury and Rehena Akhter Yasmeen; and my dear brother, Sadeen Bin Karim - my only shades of color in this grim monochromatic world.

Acknowledgements

This work could never have been accomplished without the help, guidance and patience of many wonderful people. I would like to express my utmost gratitude to Professor Reinhard Vehring for his unfailing patience with me and for the opportunity he extended to me to gain experience in the marvelous world of particle engineering. Thank you for your calm demeanor in every situation, for having taught me the correct methods of scientific research and for having supported me through my highest of highs and lowest of lows. You are the best mentor one could ask for.

No man is an island, and I am not an exception. Throughout this journey, my colleagues in the Particle Engineering group have always been by my side through thick and thin. I am proud to be a small part of such a talented cohort. Special thanks to David Barona Arias, Hui Wang, Mani Ordoubadi and Mellissa Gomez for their generous and unconditional support, their willingness to answer my out-of-the-blue questions, and the hours they spent trying to help me solve my problems when they did not have to. My gratitude to Luba Slabyj for her help with the editing of my manuscripts for Chapters 2 and 3. It has been an honor and privilege working with all of you, and I hope our paths cross again in the future.

All resources and facilities provided by the University of Alberta and the National Resource Council of Canada are also gratefully acknowledged.

Table of Contents

List of Tables

List of Figures

Chapter 1. Introduction

1.1. The scenario of Enteric Infections Around the World

The achievements of medical science in the last century have been remarkable, ranging from the invention of antibiotics and the eradication of diseases like smallpox and polio to new treatments for diseases once thought incurable, like cancer, and most recently, the development of vaccines to fight the COVID-19 global pandemic. However, these achievements sometimes overshadow less visible epidemics still in existence. Enteric infections have for decades been among the leading causes of death around the world. In 2016, diarrhoea was the eighth leading cause of death in all age groups (1.6 million) and the fifth leading cause of death among children under the age of five (Troeger et al., 2018). The World Health Organization reports 1.3 to 4 million cases of cholera each year, with an estimated death toll of 21,000 to 143,000 (WHO and UNICEF, 2019). Although enteric infections are predominant in the developing countries of Asia and Africa, more highly developed regions like North America are not immune to the effects of these infections. In 2014, an estimated 7.15 million cases of waterborne enteric infections caused 6,600 deaths and incurred US $3.33 billion in healthcare costs in the USA (Collier et al., 2021). Although advances have been made in the form of vaccines and drugs to treat these infections, the lack of access to clean water and sanitation systems along with inadequate healthcare infrastructure in developing countries nevertheless leave whole populations susceptible to infection. According to the WHO, 29% of the world's population in 2017 did not have access to safely managed drinking water services, with 2 billion lacking basic sanitation services and 3 billion lacking even basic handwash facilities (WHO and UNICEF, 2019).

Enteric infections like cholera, shigella, amoebiasis and campylobacteriosis are treated with antibiotics. However, studies show that the bacteria responsible for these infections are becoming resistant to the antibiotics currently available for their treatment (Chiu et al., 2002; Glass et al., 1980; Mwansa et al., 2007; Reinthaler et al., 2003; van den Bogaard et al., 2001; Yoke-Kqueen et al., 2008). This fact is alarming given that the development of new small-molecule antibiotics has failed to keep pace with the emergence of resistant strains of bacteria. Biological entities, bacteriophages in particular, have the potential to fill the void and offer alternative options for the treatment of enteric infections. However, as biological entities, bacteriophages need protection from the mechanical stress of processing conditions (Jończyk et al., 2011) and the harsh chemical environment of the gastrointestinal tract, both of which may render them inactive (Abdelsattar et al., 2019; Koo et al., 2001, 2000). Therefore, the selection of production method, processing parameters and excipients is a very important step in the early stages of developing a platform for phage delivery.

1.2. Overview of Eudragit®, the Enteric Polymer

Eudragit® is the commercial name of a range of polymethacrylate polymers marketed by Evonik Industries Inc. The polymers are synthesized through polymerization of acrylic acid and methacrylic acid or their esters at varying proportions (Rowe et al., 2009). Eudragit is commercially available in different forms, such as dry powder, granules, aqueous dispersions, and organic solutions. The types of Eudragit can be divided into 3 broad classes according to their solubility profile (Thakral et al., 2013). Cationic Eudragit

E, which is soluble below pH 5.5, is used as a film coating for taste-masking applications (Cerea et al., 2004; Drašković et al., 2017). Anionic Eudragit L and S, which are soluble above pH 6 and 7, respectively, have widespread application as enteric coatings for colon-specific drug delivery (El-Malah and Nazzal, 2008). Neutral Eudragit RL and RS, whose solubility is pH-independent, and Eudragit NE and NM, which exhibit pH-dependent swelling and permeability, are used for sustained drug delivery (Das et al., 2010; Lunter and Daniels, 2012). The glass transition temperature, T_g , of the polymer varies with its molecular structure. The anionic polymers (Eudragit L and S) have the highest T_g at >150 ˚C, whereas cationic Eudragit E has a relatively low T_g of 48 ˚C. The neutral, insoluble Eudragit RS and RL undergo the transition at 65 ˚C to 70˚ C. Another important property of Eudragit is its water vapor transmission rate (WVTR), which impacts the storage stability of formulations with high moisture sensitivity. Compared to other controlled-delivery polymers like Hypromellose (WVTR = 900 g/m^2.day), polymethacrylate polymers show effective moisture barrier property (WVTR = 100-350 g/m^2.day) (Thakral et al., 2013).

1.2.1. Coating Methodology of Eudragit

In the last 50 years, several methods have been used to employ Eudragit for delayed drug release, taste masking and protection against the harshly acidic environment of the gastrointestinal tract. Film coating technology has evolved significantly in terms of both composition and manufacturing processes. Sequentially, the dry powder coating process begins with the pretreatment of the coating material, followed by application of the coating material to the substrate. The uniformity of the coating depends heavily on the adhesive nature of the formulation (Sauer et al., 2013). Formation of the film may occur by a process of coalescence, evaporation, or sintering. Other than evaporation, these processes do not require the use of any volatile solvents, which is advantageous in cases where the active pharmaceutical ingredient is sensitive to water or organic solvents (Sauer et al., 2013). The glass transition temperature of the polymer plays an important role, as it impacts the coalescence and adhesive properties. Usually, plasticizers are added to the polymers with a higher T_g in order to decrease the value and thereby facilitate adhesion. Present-day dry powder coating processes can be classified into three major types: liquid-assisted coating, thermal adhesion, and electrostatic coating. All of these processes are widely used to apply enteric coatings to pellets and tablets. Liquid-assisted coating, as the name suggests, uses solvents for the coating process. However, unlike conventional coating processes, it limits the use of these solvents and often uses a liquid phase excipient that serves as an adhesive and provides functionality in forming the film. (Pearnchob and Bodmeier, 2003) used liquid-assisted coating to coat drug-layered pellets with micronized Eudragit RS. Propranolol HCl was used as the model drug, and the coating was applied using a modified fluidized-bed Wurster process. The process was evaluated with different plasticizers (Acetyl tributyl citrate, AMG and TEC) and, to complete the film formation process, the coated pellets were oven-cured at 60 ˚C for two hours. The curing process improved the drug release capability of the pellets, showing a consistent release pattern even after three years of storage.

Thermal adhesion eliminates the use of solvents from the film formation process altogether. Instead, it relies solely on the complex thermal adhesive properties of the coating powder. The first extensive use of this technique was reported by (Cerea et al., 2004). Micronized Eudragit E PO was used as the coating material, and a laboratory-scale spheronizer with a smooth stainless-steel disc was used for the process. The heat required to perform the process was generated using an infrared lamp placed approximately 3 cm above the spheronization chamber. The coating powder was fed to the rotating disc using a motorized single-screw powder feeder. After the initial powder layering, the tablets were cured in a static oven at 80 ˚C for 12 hours. (Wang et al., 1997) replicated the process with Eudragit RS 30D, adding talc to the plasticizers as an anti-sticking agent, a technique that demonstrably improved the blending of the coating and prevented agglomeration during storage. (Sauer and McGinity, 2009) used a mixture of Eudragit E PO and Eudragit L 100-55 along with talc and plasticizers to coat the tablets. Eudragit L 100-55 was pre-plasticized to reduce the glass transition temperature and melt viscosity. In all the above-mentioned cases, the adhesion, surface spreading and mobility of the polymer were improved, leading to enhanced film formation.

Electrostatic coating is used mostly in metal finishing industries to coat corrosive metal surfaces. Application of this method in pharmaceutical industries is not common, but several studies have shown it to provide production output comparable to that of large commercial units. The process requires specialized equipment to coat both sides of the tablet cores separately. The process mimics the ink toner deposition in photocopying. (Qiao et al., 2010b) used a laboratory-scale electrostatic powder pan coating system to coat ibuprofen cores with micronized Eudragit E PO. The coating process consisted of preheating and spraying the plasticizer, feeding charged polymer particles to the coating bed and curing the layer at an elevated temperature. Polyethylene glycol and a glycerol/water mixture were used as plasticizers, and curing was done at 40-60 ˚C for two hours. The same process was used to evaluate the performance of Eudragit RS and RL (Qiao et al., 2010a). As in the previous study, ibuprofen was used as the model drug, but the plasticizer was changed to TEC, and talc was used as an anti-tacking agent.

Solvent evaporation is one of the most popular methods used for micro- and nanoencapsulation of particles. In this technique, the coating polymer is dissolved in a volatile organic solvent, and the drug core is dissolved or dispersed to form a solution, a suspension, or an emulsion. An emulsifying medium, immiscible in the dispersing phase, is added under agitation. Once the mixture is stabilized, agitation is continued and the solvent evaporates after diffusing through the continuous phase, resulting in the formation of solid spheres with the polymer as a protective coating. Different studies have explored the effectiveness of this process in encapsulating microparticles using different grades of Eudragit. (Sahoo et al., 2005) used Eudragit RS 100 and RL 100 to coat stavudine, an orally administered drug for HIV treatment, by employing an acetone/liquid paraffin system along with magnesium stearate as a stabilizer. (Basu and Adhiyaman, 2008) used Eudragit RL 100 to coat nitrendipine in an ethanol/liquid paraffin system; span 80 (sorbitan monooleate) was used as an additional emulsifier in this case. (Deshmukh and Naik, 2014) used Eudragit RS 100 as a coating for aceclofenac, employing methanol/water and dichloromethane/water as the emulsion solvents. (Lee et al., 2000) used a double-solvent emulsion system (water/dichloromethane/corn oil) to coat theophylline with Eudragit S100; span 80 was used as a surfactant in this case. The particles were collected by filtration and then rinsed with n-hexane and oven-dried. All of these studies characterized the drug release profile of the microencapsulated particles at varying pH. The profile was highly dependent on pH, with acidic media showing lower release rates than alkaline media (Lee et al., 2000). (Dai et al., 2015) used a modified version of solvent evaporation to coat cyclosporine A with different grades of Eudragit. Ethanol was used to dissolve cyclosporine A and Eudragit, with silica used as dispersed material in the solution. The mixture was agitated and ultra-sonicated and a rotary evaporator was used to remove ethanol from the solution. An *in-vitro* dissolution study showed an elevated release profile for cyclosporine A at pHs higher than 7.4.

1.3. Applications of Eudragit in Spray Drying

Spray drying has long been widely used in the pharmaceutical and biomedical industries because of its ability to process delicate excipients in substantial quantities. The process involves the atomization of a liquid feed (solution, suspension, or emulsion) into small droplets inside a chamber using a flow of hot drying gas. The temperature difference leads to flash drying of the droplets, removing the solvent to form solid particles. The particles are then separated from the drying gas using a cyclone chamber. The properties of the final product, such as particle size, morphology and residual moisture content, can be regulated with relative ease by manipulating process parameters like the feed flow rate, the drying gas flow rate and the inlet temperature (Vehring et al., 2007).

The application of Eudragits in spray drying is relatively new. Because of their insolubility in water, organic solvents like methanol, ethanol and dichloromethane, or their combinations, are used to dissolve the Eudragit along with other suitable excipients and deliverable active ingredients. (Rassu et al., 2008) used dichloromethane to dissolve Eudragit RS100 and Eudragit RL 100 along with ketoprofen and then spray-dried microspheres from the formulations. (Sóti et al., 2015) dissolved itraconazole and Eudragit E in dichloromethane: methanol (4:1) to spray dry microparticles. Instead of organic solvents, some studies have used aqueous dispersions of Eudragits to spray dry the active ingredients. (Esposito et al., 2002) used aqueous dispersions of Eudragit RL, RS and L to encapsulate Ascorbic acid by spray drying. (Garekani et al., 2013) used both ethanol and aqueous dispersions of Eudragit RS 30D to spray dry theophylline. The aqueous dispersion resulted in a higher process yield; however, the efficiency of the resulting product's sustained drug release was low.

The spray drying of Eudragits has also been used to encapsulate biological material within particles, but these applications are scarce. Rhizobacteria (*Pseudomonas fluorescens-putida*), spray-dried with an aqueous dispersion of Eudragit RS 30D at 60 ˚C and 80 ˚C showed the presence of bacteria encapsulated within the particles at a 2 logarithmic unit loss in 15% alcohol solution (Amiet-Charpentier et al., 1998). An inactivated strain of *Vibrio cholerae* spray-dried with an aqueous dispersion of Eudragit L 30D and FS 30D has shown successful encapsulation of the bacteria within the particles and delayed releasing properties for particles collected at low outlet temperature (Año et al., 2011). A recent study focused on spray drying *Myoviridae* bacteriophage Felix O1 with Eudragit S100 and trehalose at different inlet temperatures (Vinner et al., 2019). Analysis of the produced powders showed a higher phage concentration in pure trehalose particles, but the survival of phages in the simulated gastric fluid was much higher in particles containing Eudragit (Vinner et al., 2019).

Despite these reported successes, however, few insights into the actual formation process of the particles, their specific core-shell morphology, and the mechanisms underlying their ability to withstand exposure to the acidic pH of the stomach can be found in the published studies. A better understanding of the particle formation process is needed for a rational design of such particles.

1.4. Particle Engineering to Create Suitable Carrier Particles

The initial size and composition of droplets and their drying conditions play a very important role in dictating the transition of the droplets into dried particles as well as their internal and external morphology (Hoe et al., 2014). Thus, fundamental investigation of particle formation from solution droplets is important prior to mass production. Studying single evaporating droplets or a series of monodisperse droplets falling through a drying medium is the most effective approach for this purpose. The single droplet evaporation technique provides steady measurement of droplet evaporation throughout its lifetime, thus allowing for instant measurement of microscopic and spectroscopic properties (Kalume et al., 2018). On the other hand, the monodisperse droplet chain technique is capable of dispensing droplets continuously through the use of an on-demand droplet generator, thus producing particles for physical analysis like scanning electron microscopy. However, the efficiency of particle collection is usually not sufficient for more detailed solid-state analysis like macro-Raman spectroscopy.

This thesis explores the potential of microparticles formed by the combination of Eudragit S100, a methacrylic acid-methyl acrylate copolymer capable of pH-dependent dissolution, and trehalose, a glass-forming disaccharide, as a potential platform for delivering bacteriophages in the treatment of enteric infections. Chapter 2 discusses the modifications made to an existing monodisperse droplet chain instrument to increase its functionality. The addition of an interferometric laser imaging system for droplet sizing in order to measure initial droplet diameter and the incorporation of a single-nozzle impactor for particle collection increased the accuracy of calculation and broadened the instrument's scope of use. Chapter 3 explores the formation process of carrier particles with a polymer shell and a disaccharide core to understand how the morphology of the particles can be controlled with the help of a monodisperse droplet chain. The particle formation process was investigated for two different solvent combinations—an ethanol-water co-solvent system in which both trehalose and Eudragit had high solubility, and an aqueous system which dissolved both components using a pH shifting technique. The release characteristics of the spray-dried powder were investigated using a new shadowgraphic imaging technique. The results reported in the thesis establish the monodisperse droplet chain as a powerful tool in preliminary investigation of the particle formation process and in the quantifying of important properties before initiating mass production. The results also shed light on previously unexplored aspects of the particle formation process of the Eudragit-trehalose system and the viability of spray-dried particles as a delivery platform for biologics intended for gastrointestinal delivery in humans and animals.

Chapter 2. Improved Monodisperse Droplet Chain as An Effective Tool to Investigate Particle Formation Parameters

2.1. Introduction

Spray drying is a widely used manufacturing process that converts the liquid phase of a formulation to the solid phase by breaking down the liquid into small droplets and drying them to forms particles of the solutes. This technique has been in use for over a century in the food, ceramic, polymer, and chemical industries (Bora et al., 2008; Kim et al., 1996; Schuck, 2002; Thaker et al., 2010; Walz et al., 2018). Spray drying has also been successfully used in the pharmaceutical industry, with applications including the enhancement of bio-stabilization in oral administration (Davis and Walker, 2018), glass stabilization of biologics within particles, the development of particles suitable for respiratory drug delivery, and drug encapsulation for modified release (LeClair et al., 2016; Walz et al., 2018).

Since the shape and size of the spray-dried particles directly affect their properties, it is important to investigate the drying process of droplets containing the excipients and the active pharmaceutical particles. The time for a droplet to evaporate is proportional to the square root of its initial diameter (Fuchs, 2013), which makes the drying kinetics and particle properties susceptible to a change in droplet diameter. Thus, fundamental investigation of particle formation from solution droplets is important prior to mass production. The investigation is usually carried out by studying single evaporating droplets or a series of monodisperse droplets falling through a drying medium. Both techniques allow for precise control of the initial droplet diameter. The single droplet evaporation technique allows measurement throughout the droplet lifetime and is useful in investigating microscopic and spectroscopic properties (Kalume et al., 2018). However, it does not produce a sufficient quantity of particles for physical evaluation. The monodisperse droplet chain technique uses on-demand droplet generators, which are capable of dispensing liquid droplets continuously at specific time intervals, thereby forming a straight chain of falling droplets through the drying medium. Depending on the efficiency of collection at the outlet, particle production in a monodisperse droplet chain is usually large enough to study morphology using microscopy techniques but is insufficient for solid-state analysis using processes like macro-Raman spectroscopy.

The following sections discuss the modifications made to a monodisperse droplet chain to improve the accuracy and precision of initial droplet diameter measurement and to increase particle collection efficiency. Studies were performed to verify the effects and limitations of the changes.

2.2. Unmodified Setup

The monodisperse system prior to modification consisted of a double-walled cylindrical Pyrex glass flow tube connected to a circular heating gas flow pipe at the inlet. The shape of the flow tube facilitated the smooth transition of hot air flow at the inlet from the circular heating tube. Calculations showed that for a flow tube with a 35 mm diameter, the laminar flow inside the tube can be maintained for a maximum air flow of 10 L/min. An imaging system consisting of a camera (GO-5000M-USB, JAI Inc., San Jose, CA, USA), a strobe light (M530L3-C1 Collimated LED, Thorlabs Inc., Newton, NJ, USA) and a zoom lens (Optem FUSION 12.5:1 lens, Excelitas Technologies Corp.,Waltham, MA,USA) was mounted on a platform to capture images of the droplets falling through the drying gas flow. The platform was capable of moving vertically using a motorized stage (Velmex BiSlide, Velmex Inc, Bloomfield, NY, USA). A custom-designed dispensing system was used to supply the stock solution to a piezoelectric droplet dispenser (Microfab Technologies Inc., Plano, Texas, USA) to dispense the droplets inside the flow tube. The frequency and pulse width of droplet generation was controlled by an electric controller (MD-E-3000, Microdrop Technologies GmbH, Germany). As the droplets fell through the flow tube, the drying gas evaporated the solvent, and the remaining solids reached the bottom of the tube as particles. The particles were collected through the side of the tube directly onto aluminum stubs (Ted Pella, Inc.; Redding, CA, USA) using a vacuum. The whole system was supported by an aluminum support assembly. The imaging system was used to determine the diameter of the droplets at the point of dispensation. The frequency of the camera was matched with the dispensation frequency using a dual-channel function generator to produce images of stationary droplets. The shadowgraphic images of the single droplets were processed in MATLAB to calculate the diameter of the droplets. Figure 1 shows a simple schematic of the setup.

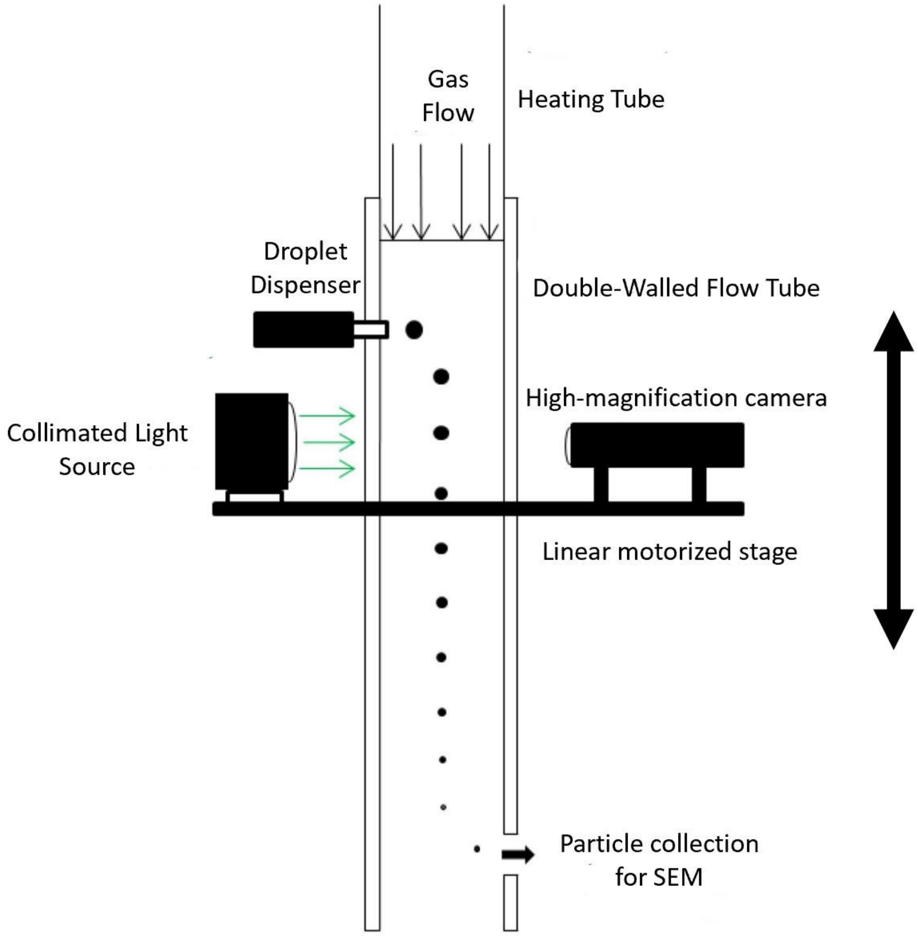

Figure 1: Schematic of the monodisperse droplet chain instrument before modification (Gomez et al., 2018)

Since the images were taken through a double-layered glass wall, the curvature of the wall formed two separate shadows along with the original shadowgraph. The MATLAB code created a profile around the region with the darkest circle based on the pixel values in order to identify the original position of the droplet. However, at higher magnification, the depth of field of the focal plane shrank considerably. As a result, even the slight movement of a droplet from the focal plane gave rise to a relatively high margin of error in diameter measurement. The particle collection system allowed the collection of enough particles for imaging with a scanning electron microscope, a process that took about 1.5 to 2 hours. However, it was not possible to collect enough particles for any solid-state analysis technique like Raman spectroscopy. An attempt to accumulate sufficient particles for a single macro-Raman spectroscopy run was made but failed after five hours of particle collection.

2.3. New Setup after Modification

Modifications were made to the existing setup to eliminate the sources of error in measuring the initial droplet diameter, reduce the collection time, and increase the particle collection efficiency.

2.3.1. Flow Tube Selection

Although the cylindrical flow tube helped stabilize the drying gas flow, the curvature of the wall and the presence of two glass layers caused inaccuracy in the initial droplet diameter calculation. To mitigate this issue, the previously used flow tube was replaced by a new single-walled glass flow tube with a square cross-section. However, the junction of the circular cross-section of the heating tube and the square cross-section of the flow tube created flow instability at the entrance, thereby affecting the stability of the gas flow within the flow tube. To counteract this effect, a flow straightener was attached at the entrance of the flow tube. The flow straightener eliminated the lateral component of flow velocity at the junction caused by the swirling motion of air and created a stable, laminar flow at the inlet of the flow tube.

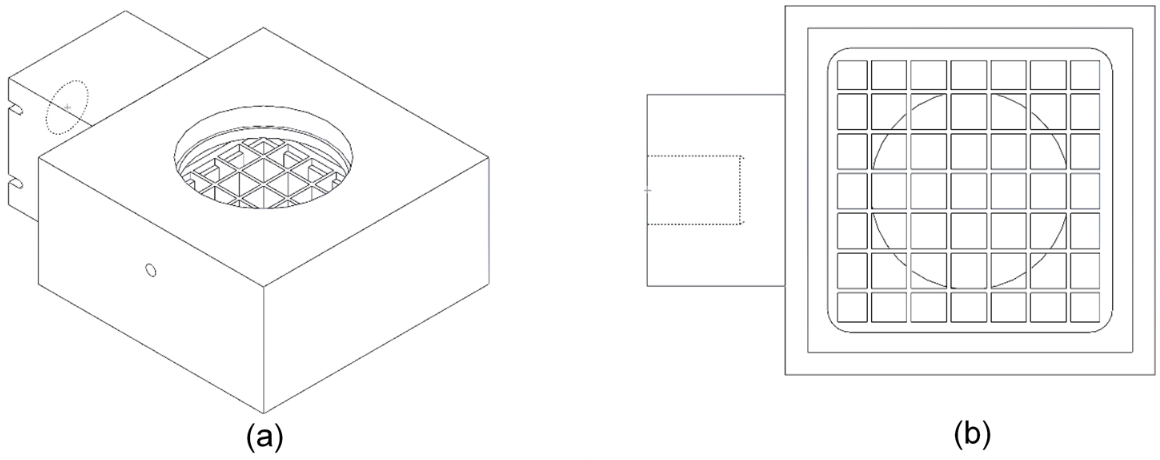

Figure 2: (a) Isometric view and (b) top view of flow straightener used to reduce turbulence at the entrance of the flow tube.

To select a suitable cross-section of the tube, calculations were done to determine the effect of varying flow rate and tube size on the Reynolds number. The Reynolds number, Re, is expressed as the ratio of the inertial forces in a fluid to the viscous force,

$$\mathrm{Re} = \frac{4\rho Q}{\mu \pi D}, \qquad 1$$

where *ρ* is the density of the air, *μ* is the viscosity of the air, *Q* is the volumetric flow rate and *D* is the hydraulic diameter of the tube. Table 1 shows the results of the calculation of the Reynolds number at various flow rates and tube diameters. The drying gas was assumed to have properties of dry air at standard ambient temperature and pressure (25˚ C and 1 bar). For all the combinations, the value of the Reynolds number is considerably smaller than 2300, indicating the flow inside to be laminar.

Table 1 Calculated Reynolds number and velocity of drying gas leaving the flow straightener and entering the flow tube at different air flow rates.

Air flow (L//min)	Hydraulic Diameter of the flow tube (mm)	Velocity (m/s)	Reynolds Number
1	41	0.01	33
2		0.03	66
5		0.07	165
10		0.14	329

To increase the temperature of the drying gas and ensure a fully developed flow at the entrance of the flow straightener, a copper tube with an internal diameter of 35 mm, wrapped with heating tape, was used to connect the in-house air supply line and the flow straightener. To measure the required entrance length of the tube at the entrance of the flow straightener, the following equation was used (Bergman et al., 2011)

$$l_{\mathrm{Laminar}} = 0.05\ \mathrm{Re}\ D = 0.05 \frac{4\rho}{\pi\mu}. \qquad 2$$

For an air flow of 10 standard L/min, measured with a flow meter (TSI Series 4100, TSI Incorporated, Minnesota, USA), which defined the standard condition as 21.1˚ C and 101.325 kPa, the entrance length was calculated as 820 mm. Figure 3 shows the flow tube along with the position of the dispenser and the assembly of the heating tube, the flow straightener and the flow tube.

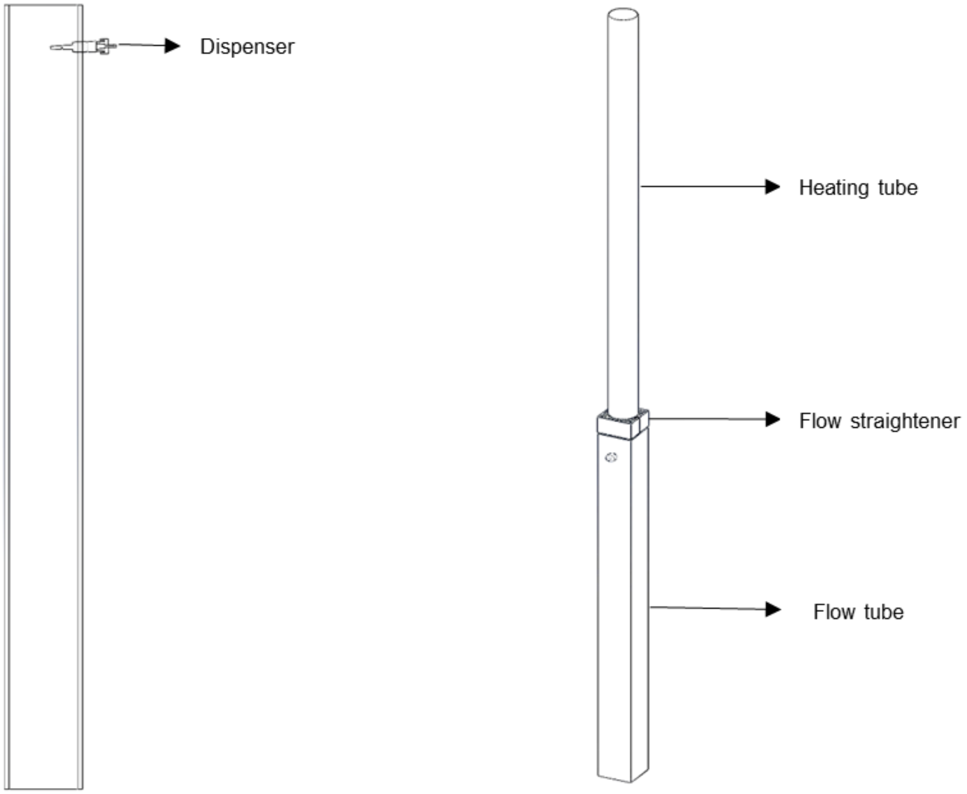

Figure 3: (a) Side view of the new flow tube (b) isometric view of the heating tube-flow straightener-flow tube assembly. The piezoelectric dispenser is inserted through an inlet at the side of the tube.

The calculations did not account for the presence of the dispenser within the flow, which can create disturbances and give rise to turbulence within the flow tube. To obtain a better visualization of the drying gas flow within the flow tube, the flows were simulated using ANSYS fluent software, adding the dispenser within the flow. Figure 4 shows the horizontal and vertical cross-sections of the flow-through the tube at 10 L/min. Installing the flow straightener successfully eliminated the formation of an eddy at the junction of the circular heating tube and square flow tube. The presence of the droplet dispenser within the flow created a disturbance, but its effect was negligible. The most stable velocity profile is observed at the center of the tube, which emphasizes the need for the chain of droplets to fall through that region.

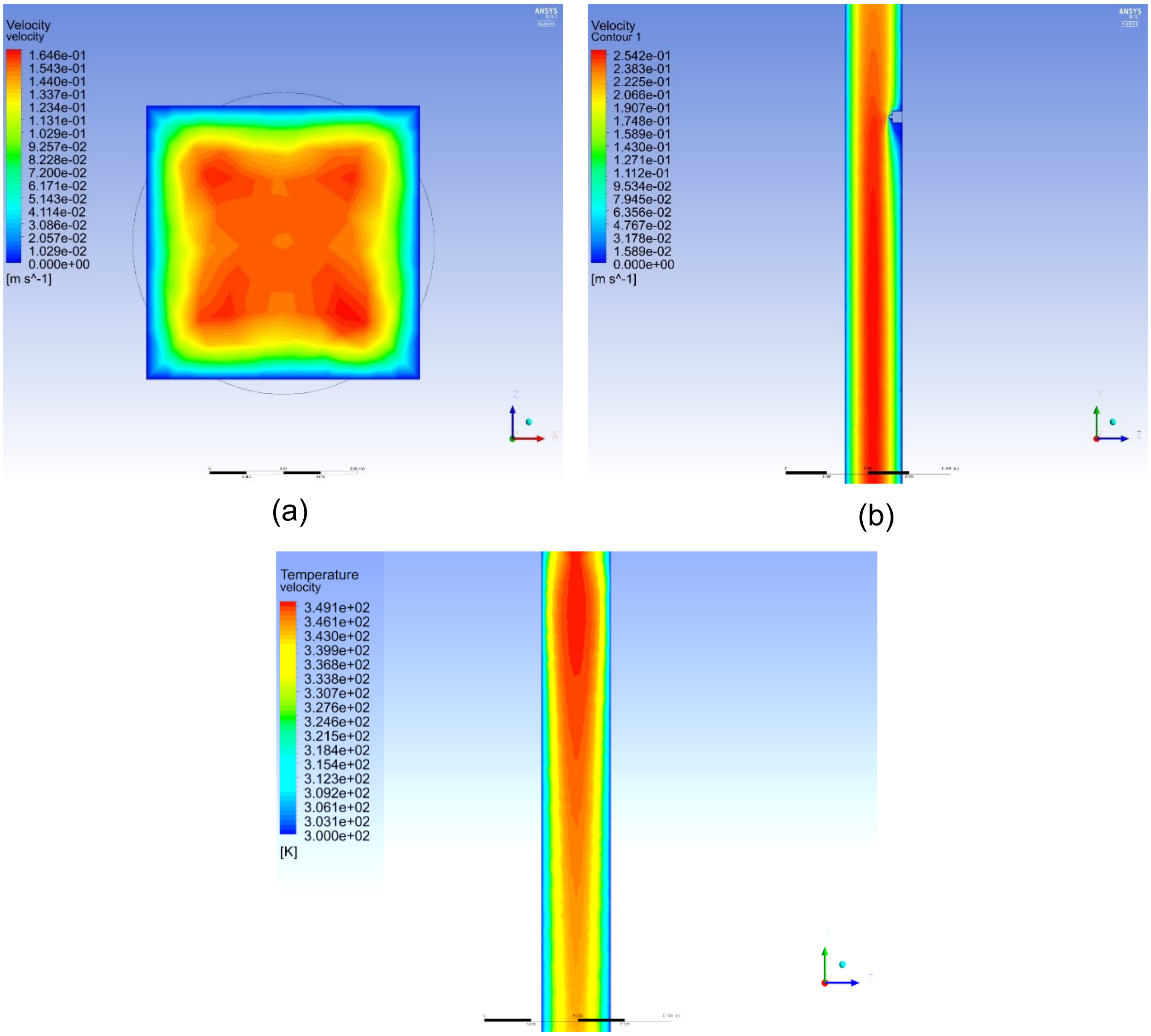

(a) (b)

(c)

Figure 4: (a) Horizontal and (b) vertical cross-section of the velocity profile of drying gas through the flow tube. (c) Temperature profile of the flow through the tube.

A caveat to using a single-walled flow tube is that heat may be lost to the surrounding environment in high-temperature applications. Unlike the unmodified version, the modified monodisperse setup makes no provision for an intermediated heating gas flow between the main flow tube and the environment. The heat radiation profile of the structure is visualized in Figure 4 (c). A simulation was run assuming the inlet air temperature to be 70 ˚C. Although heat loss close to the wall is significant, the flow maintains a relatively stable temperature profile at the mid-section. Both the velocity and temperature profiles show the importance of a stable droplet chain. Apart from the nature of the drying gas flow, chain stability can be interrupted by the accumulation of charge on the flow tube surface. This issue was resolved by grounding the flow tube with anti-static straps, which resulted in a steady droplet chain in the tube.

2.3.2. Imaging Setup

Although highly magnified shadowgraphic images of the falling droplets captured by a high-speed camera can be used successfully to calculate the droplet diameter, the process can at times be prone to inaccuracy and uncertainty. In the unmodified setup, the frequency of image acquisition was matched with the frequency of droplet generation, producing a live feed of stationary droplets on the screen. The focal plane of the camera was changed accordingly to bring the droplets within focus. Due to the presence of two glass walls between the lens and the droplet, the resulting images contained three distinct shadows. A custom-made MATLAB code capable of predicting the original droplet shadow by reading the darkest pixel data calculated the droplet diameter by converting the pixel readings into physical distance. The accuracy of the result was highly dependent on the stability of the droplets and the quality of focus. At high magnification, the depth of field of the lens was reduced in the range of 0.1 -1 mm. Even the slightest movement of the droplet within the field of view resulted in out-of-focus images of the droplet and consequent overestimations of droplet diameter. The calculated values had high precision, but the accuracy of the result was low. To obtain more accurate results, a new measurement technique less dependent on the stability of the droplet chain was required.

Laser interferometric imaging has been successfully used in the last few decades to calculate the droplet size distribution of polydisperse sprays (Glover et al., 1995; Hardalupas et al., 2010; Skippon and Tagaki, 1996). The process uses a collimated laser beam to illuminate the region of interest. As light passes through the droplets, rays are scattered in every direction because of reflection and refraction. The intensity distribution of the scattered light across a scattering angle of theta depends on the complex refractive index of the droplet component and the size parameter of the particle, the relationship between which can be expressed as

$$\alpha = \frac{\pi d}{\lambda}\ , \tag{3}$$

where α is the size parameter, *d* is the droplet diameter and λ Is the wavelength of the incident light. For $\alpha \rightarrow 0$, the elastic scattering intensity distribution is uniform in all directions and is known as Rayleigh scattering. As the size parameter increases, the intensity distribution exhibits more oscillations, which can be explained using the Lorenz-Mie theory (Slimani et al., 1984) for $\alpha \approx 1$. For larger droplets, $\alpha > 50$, light scattering can be explained using ray optics. Since the calculation using Mie theory requires complex numerical procedures, it is advantageous to use ray optics to predict the phenomena for finite values of α (Glantschnig and Chen, 1981).

One important aspect of droplet sizing using laser interferometry is selecting the scattering angle. Depending on the diameter of the droplets and the value of α, the number of fringes within an angular range changes drastically. For very small values of α, as in Figure 5 (a), the number of visible fringes is very low and no discernible change in intensity can be seen. Figure 5 (b) shows the change in intensity for larger values of α (α = 23). The peaks of intensity change become more distinct, with more visible regular peaks in the wide-angle forward scattering region. For values of α approaching infinity, the peaks at low scattering angles (narrow-angle forward scatter) are dominated by diffraction. The backscattered light shows uneven changes in intensity and is responsible for phenomena like the rainbow and the glory effect (Lock et al., 1994; Nussenzveig, 1979). Figure 5 (c) shows the change in scattering intensity in the wide-angle forward scattering region, which ranges from 20˚ to 70˚, is regular and therefore results in fringes with regular intensity.

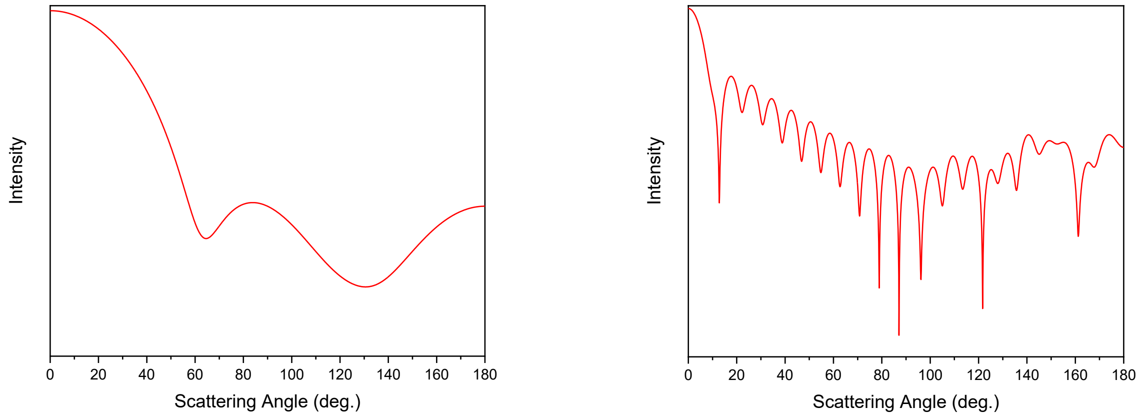

(a)

(b)

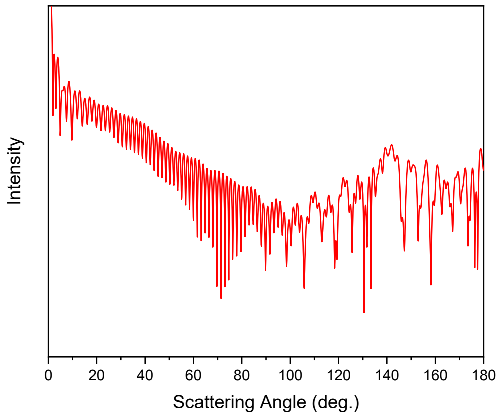

(c)

Figure 5: Angular intensity distribution of scattered light for (a) α=1, (b) α=23 and (c) α=100 obtained using Mieplot. Higher α values generate more regular peaks in the wide-angle forward scattering zone.

The formation of these fringes can be explained using geometric assumptions. The fringes originate from the interference between reflected and refracted light rays of order p=0 and p=1 (Glantschnig and Chen, 1981). The angular frequency of the observed fringes is directly proportional to the diameter of the droplet, which helps in determining the diameter accurately. To capture images of the interference fringes, a modified technique was adopted whereby only the glare points of the illuminated droplet could be seen. To observe the interference pattern, out-of-focus images of the droplet in a plane slightly displaced from the focal plane were processed. The diameter of the droplet could then be calculated using the following equation (Hesselbacher et al., 1991) based on geometric approximation (König et al., 1986):

$$d = \frac{2\lambda}{\Delta\theta_c}\left(\cos\left(\frac{\theta}{2}\right) + \frac{m\sin\left(\frac{\theta}{2}\right)}{\sqrt{m^2 - 2m\cos\left(\frac{\theta}{2}\right) + 1}}\right)^{-1} . \qquad 4$$

Here λ is the wavelength of the illumination source, $\Delta\theta_c$ is the angular spacing of the fringes, θ is the scattering angle, m is the refractive index of the droplet and d is the diameter of the droplet.

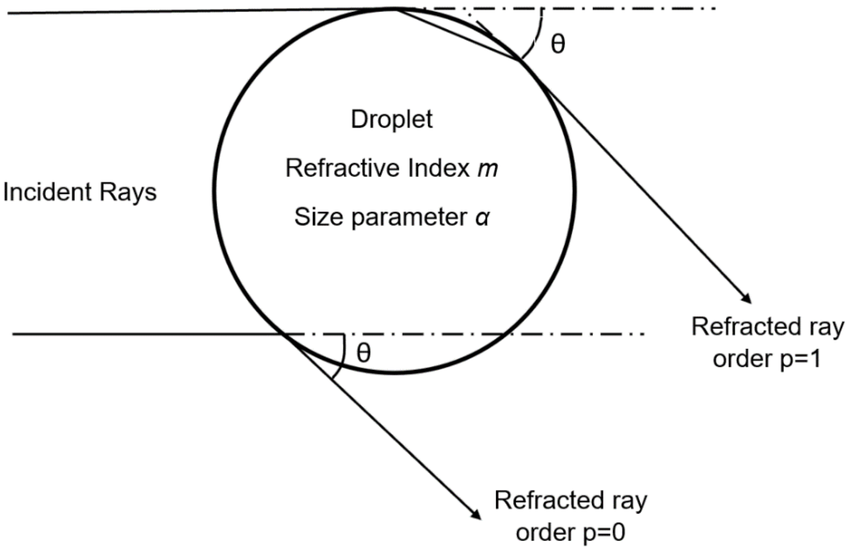

Figure 6: Geometric approximation of reflection and refraction of incident rays in a droplet by successive air-water and water-air interfaces

The monodisperse droplet chain was modified to incorporate the interferometric droplet imaging technique for droplet sizing. A 671 nm diode laser (Process Instruments, Salt Lake City, Utah, USA) was used as the illumination source. The output laser beam of the source was vertically polarized, but it was divergent and not collimated. The beam was passed through an iris diaphragm (SM1D12C, Thorlabs Inc., Newton, NJ, USA) to eliminate any diffused rays, and the beam size was reduced and collimated using two convex lenses. A mirror assembly was then used to direct the beam towards the droplet chain. The final reflector was attached to a stage capable of moving vertically with the camera. The direction of the beam was adjusted to change the direction of the scattering angle as needed. A camera (GO-5000M-USB, JAI Inc., San Jose, CA, USA) with a high aperture manual lens was mounted on a platform which was attached to a motorized stage (Velmex BiSlide, Velmex Inc, Bloomfield, NY, USA) capable of moving vertically. The movable stage and the camera assembly are shown in Figure 7.

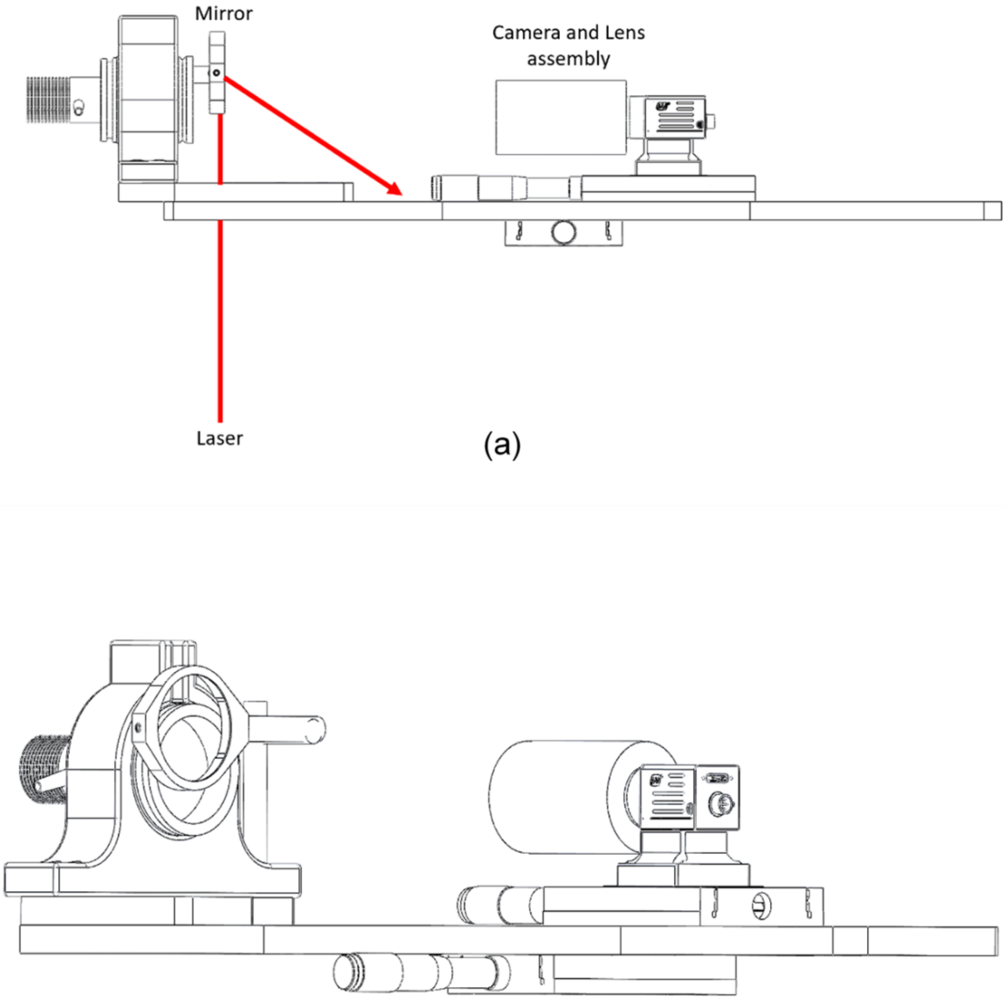

Figure 7: (a) Side view and (b) isometric view of the modified imaging system.

The terms θ and m in Equation 4 are constants based on the selected scattering angle and the solvent used in preparing the formulations. To calculate the remaining variable, the angular fringe spacing or $\Delta\theta_c$, images of the scattering pattern of the droplets were required (see Figure 8). It is possible to calculate the angular spacing of the fringes using the following equation,

$$\Delta\theta_c = \frac{\phi}{N} , \qquad 5$$

where ϕ is the collection angle of the camera lens and *N* is the number of observed fringes. However, a potential problem with using this equation lies in determining the number of fringes; i.e., since *N* is an integer, it fails to account for the fractional fringes within the frame, resulting in a relatively high margin of error. For example, for a 40 μm droplet, a change of 1 in the value of *N* adds 4% to the margin of error. Therefore, instead of using Equation 5, the angular spacing of the fringes was determined by finding the angular distance between adjacent fringes. To process the images, a MATLAB graphic user interface capable of converting the image into greyscale and plotting the phase function against the pixel position in the horizontal direction was created. Figures 8 (a) and (b) show an example of a raw image of captured scattering pattern and the corresponding generated greyscale image.

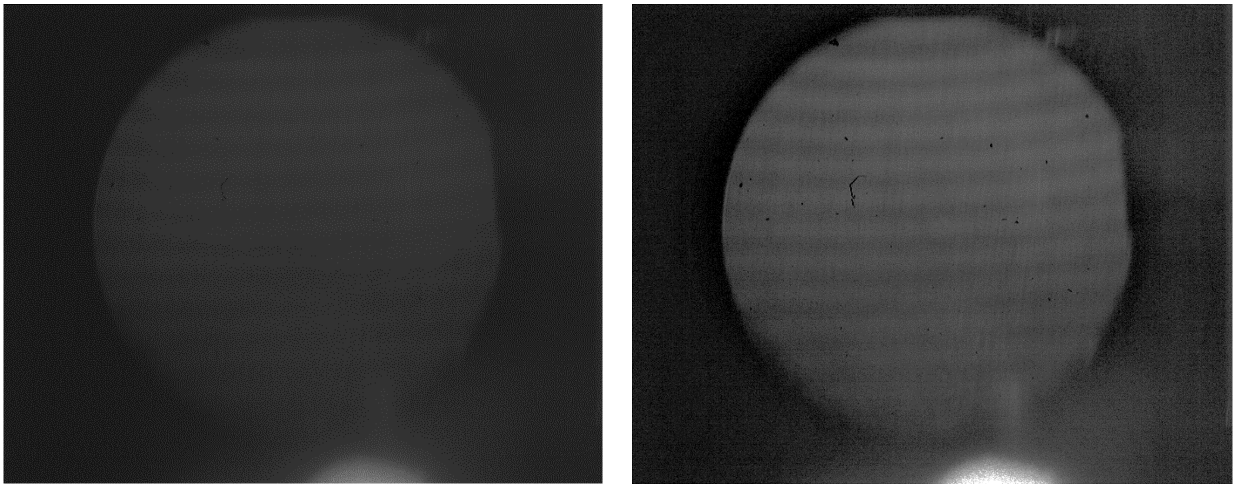

(a) (b)

Figure 8: (a) Raw unprocessed image of angular scattering pattern, (b) processed image using custom-built MATLAB graphic user interface

The phase function was curve-fitted using the default curve-fitting tool in MATLAB. The angular resolution of each pixel, β, can be expressed as

$$\beta = \frac{\phi}{x_{image}} , \tag{6}$$

where ϕ is the aperture angle of the camera and x_{image} is the horizontal length of the aperture in pixels. The angular fringe spacing can be expressed with the help of angular resolution as

$$\Delta\theta_c = \mu_{peak}\beta , \tag{7}$$

where μ_{peak} is the average peak-to-peak distance between two consecutive fringes in pixels. The process of calculating the fringe spacing using the GUI is explained in further detail in Appendix A.

2.3.3. Particle Collection

One advantage of the monodisperse droplet chain is its low formulation requirements. For example, in the original monodisperse chain setup, 4-5 mL of formulation with a moderate solids content (8-10 mg/mL) was sufficient to produce enough particles for scanning electron microscopy. However, the process of particle collection itself was inefficient, taking on average 1.5 to 2 hours to collect enough particles for imaging. The setup used modified aluminum stubs covered in sticky carbon tapes to collect particles. The stubs were bored in the middle and connected to a vacuum and the carbon tapes were covered with filter papers. The assembly was placed at the side of the flow tube. As the dried particles fell, they moved towards the stub because of the pressure difference created by the vacuum. Particles were deposited on the surface of the filter on the stub, which was kept in a dry box after collection for future characterization. One of the key objectives of modifying the setup was to increase the particle collection efficiency. Although the vacuum was strong enough to draw particles to the collection stubs, the positioning of the stub was not ideal for particle collection. Since the dried particles were considerably smaller and less dense than the droplets and the open end of the flow tube caused mild turbulence, a significant number of particles were released to the environment by gravity deposition. The new square flow tube eliminated the horizontal collection port and instead employed a custom-designed single nozzle impactor for particle collection (Wang et al., 2017b).

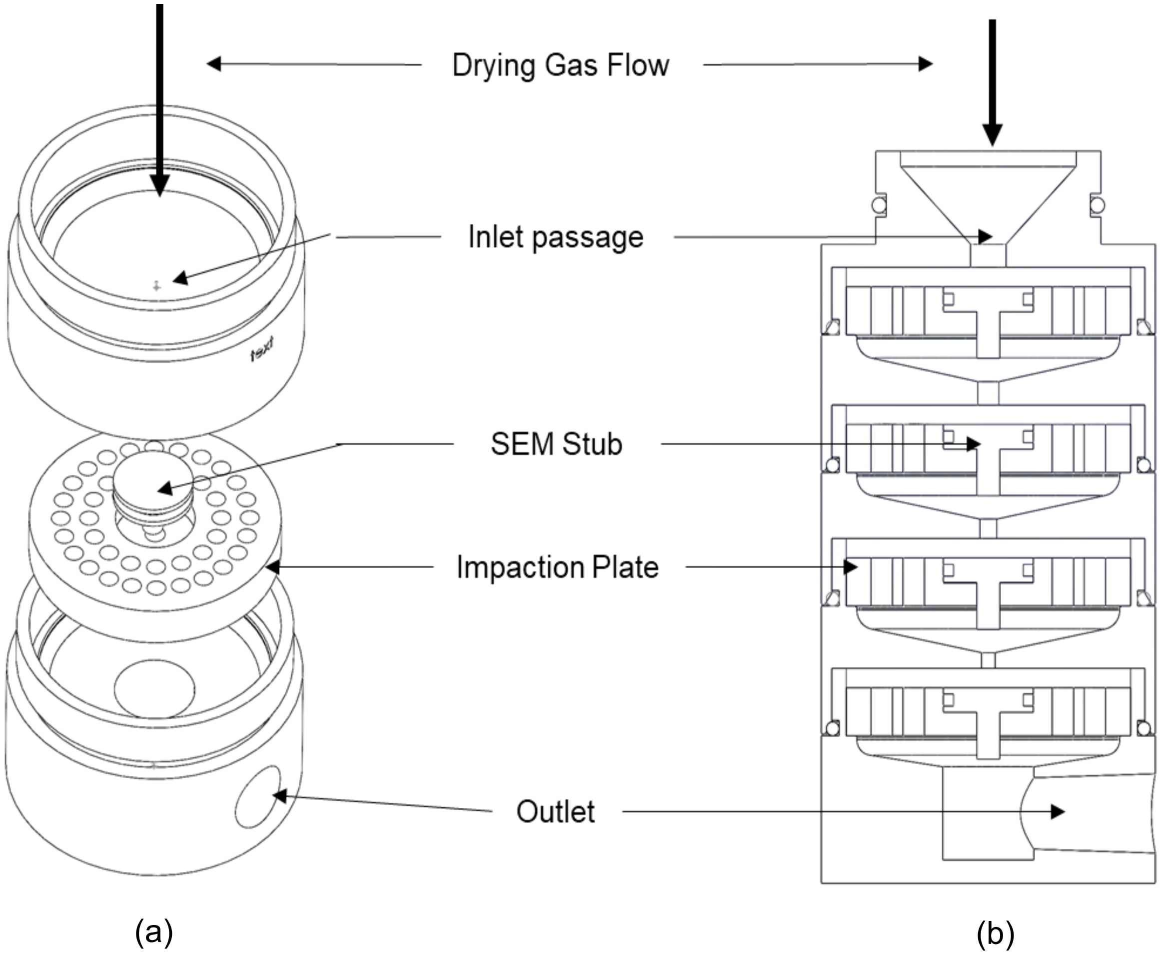

Figure 9: (a) Isometric view and (b) Vertical cross section of different stages of the single-nozzle impactor used for collection of dried particles.

The impactor consists of multiple stages with different cutoff diameters ranging from 21.1 μm to 0.6 μm. As the particles are directed toward the flat plate along with the gas flow, they are accelerated through the narrow nozzle passage. When the flow jet hits the impaction plate, it is forced to redirect by 90˚ because of the obstruction. The particles within the downstream flow are subjected to drag and inertial force. For larger particles, the inertial force overcomes the drag force generated by the abrupt change in flow. As a result, the particles impact and accumulate on the surface. The smaller particles pass through the perforations in the impaction plate and follow the flow to the downstream stage with the smaller cutoff until they are collected. The stages are removable and can be rearranged as needed. The mounting hole in the center of the plate is compatible with standard aluminum SEM stubs, which can be removed and used directly for microscopy and other solid-state analysis techniques.

Depending on the estimated particle size, two stages of the impactor are assembled. The first stage acts as the main collector, with a cutoff diameter slightly lower than the predicted particle diameter. The second stage is positioned to detect the formation of any satellites during the particle formation process. The cutoff diameter of this stage is much smaller than that of the primary stage. The downstream end of the impactor is connected to a vacuum port with the entrance of the impactor placed at the open end of the flow tube to ensure maximum collection efficiency. The vacuum flow is matched with the flow rate of the gas in the flow tube to avoid excessive pressure buildup inside the impactor. For an arrangement like this, the particle collection efficiency should be sufficient to collect enough particles for solid-state analysis, like Raman spectroscopy.

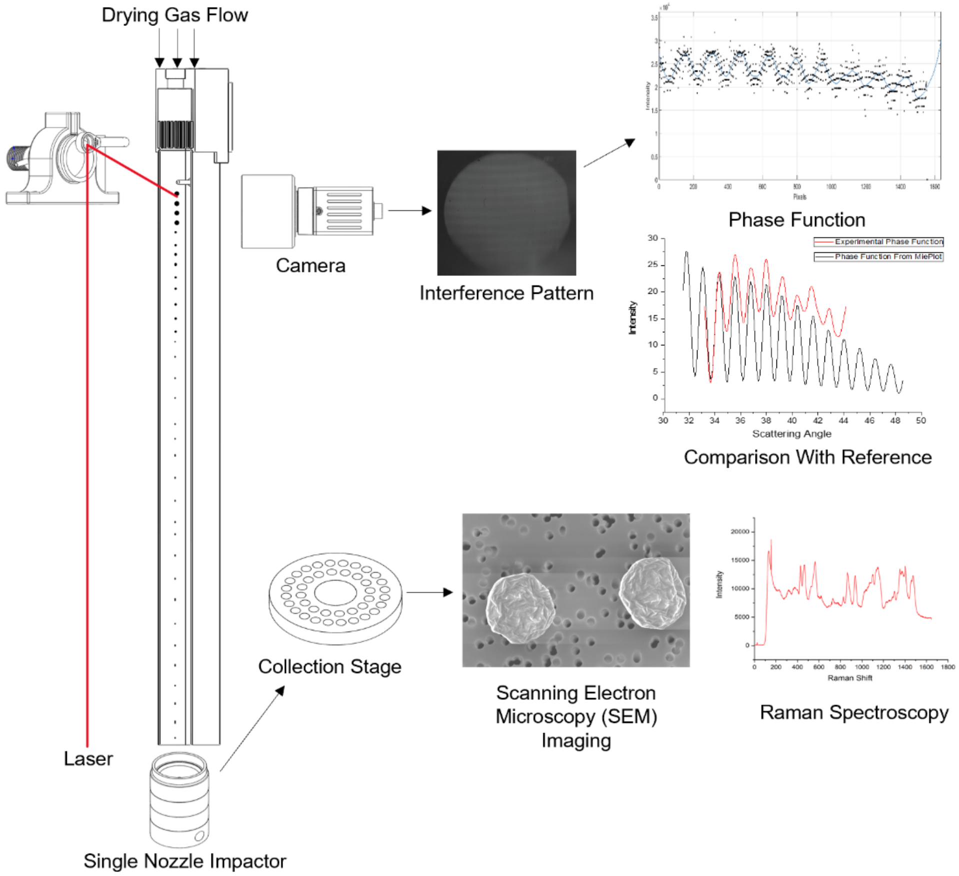

Figure 10: Schematic showing the monodisperse droplet chain with added modifications and their functionality.

2.4. Application of New Modifications

Trehalose, a disaccharide formed by a 1,1-glycosidic bond between two α-glucose units, has been widely used in the pharmaceutical industry as a glass stabilizer and as a stabilizer for biological materials because of its high glass transition temperature (Carrigy et al., 2019; Jain and Roy, 2010; Lins et al., 2004; López-Díez and Bone, 2004). Commercially, trehalose is available as a dihydrate in its crystalline form. However, upon spray drying at temperatures below its glass transition point, trehalose forms amorphous solid particles. Leucine, a non-polar aliphatic amino acid, has been used as a stabilizer for biologics alongside trehalose (Leung et al., 2018b). In a spray-dried formulation, leucine forms a fully crystalline, rugose outer shell, which improves the dispersibility of the powder (Feng et al., 2011; Li et al., 2016) and enhances aerosol performance at elevated moisture content (Li et al., 2016). Because of their ability to release drugs systematically at a targeted pH level, Eudragits are widely used as enteric coatings for tablets (Cerea et al., 2004; Drašković et al., 2017; Pearnchob and Bodmeier, 2003; Qiao et al., 2010b, 2010a; Sauer and McGinity, 2009). On spray drying, Eudragit forms wrinkled amorphous particles that are capable of protecting encapsulated bacteria from extremely acidic conditions (Año et al., 2011; Vinner et al., 2019). These three excipients were used to carry out experiments to verify the efficiency and effectiveness of the newly employed modifications to the monodisperse droplet chain instrument. The first set of experiments tested the accuracy of the interferometric droplet sizing technique by measuring the density of pure trehalose particles. The effectiveness of calculating single-particle density using the data gathered from the instrument was assessed for dried particles of different combinations of trehalose-leucine and Eudragit-trehalose, which showed different external morphologies. The second set of experiments tested the efficiency of particle collection by collecting particles for macro-Raman spectroscopy.

2.4.1. Materials and Methods

2.4.1.1 Chemicals

Trehalose dihydrate (Fisher Scientific Ottawa, ON, Canada), L-leucine (Fisher Scientific Ottawa, ON, Canada) and polymethacrylate polymer Eudragit® S100 (Evonik Industries AG, Darmstadt, Germany) were used to make formulations at different concentrations. Formulations of trehalose and leucine were prepared in deionized water at 100/0, 90/10, 80/20, 50/50 (w/w) compositions. Since Eudragit S100 is insoluble in water but highly soluble in ethanol, a mixture of ethanol and water (76.3% ethnol+23.7% water) was used as the solvent. Formulations of trehalose and Eudragit were prepared at 100/0, 90/10, 80/20 and 50/50 (w/w) compositions.

2.4.1.2 Monodisperse Droplet Chain

The modified monodisperse droplet chain was used to produce particles of similar size and morphology in order to arrive at a clearer understanding of the particle formation mechanism. The modifications and newly added features are discussed in the previous section. A 40 µm microjet orifice (Microfab Technologies Inc., Plano, Texas, USA) was used to generate droplets inside the flow tube. The drying gas flow was fixed at 3 L/min and the air was heated to 60 ˚C, with droplets generated at a rate of 60 Hz. The images of the interference pattern were processed using a MATLAB graphic user interface to determine the angular fringe spacing, which was eventually used to calculate the initial droplet diameter. The dried particles directly impacted onto the surface of removable aluminum SEM pin mounts (Ted Pella, Inc.; Redding, CA, USA) covered by carbon tape, which was used for scanning electron microscopy imaging without further sample transfer. Prior to imaging, the samples were coated with a mixture of 80% gold and 20% palladium to a thickness of approximately 10-15 nm using a sputter coater (Leica ACE600 Carbon/Metal Coater; Concord, ON, Canada). The particles were imaged by a field emission scanning electron microscope (Zeiss Sigma FESEM, Oberkochen, Germany) with an immersion lens (in-lens) detector operated at an accelerating voltage of 3.00 to 5.00 kV and using magnifications of 1000x to 5000x at a working distance of 5 mm to 6 mm.

2.4.1.3 Calculation of Particle Properties

The monodisperse droplet chain uses a stream of heated air to remove the solvent from droplets suspended in the flow. As the solvent evaporates, the dissolved solutes precipitate at the receding surface to form the desired particle. The droplet lifetime, τ_{D}, can be approximated using Equation 8 (Vehring et al., 2007),

$$\tau_{\mathrm{D}} = \frac{d_0^2}{\kappa}\ , \qquad (8)$$

where d_o is the initial droplet diameter and κ is the evaporation rate of the solvent. The initial droplet diameters were measured using the interferometric laser imaging technique described in the previous section. To calculate the evaporation rate of the droplets, a multi-solvent microdroplet evaporation model first described by (Ordoubadi et al., 2019) was used. The model used the Maxwell and Stefan-Fuchs models to measure the evaporation rate of the droplets. At each time step, the droplet temperature and compositions were measured, which aided in measuring the evaporation rate (Ordoubadi et al., 2019).

The time required for co-solidification to occur at the surface of a multi-component amorphous system in a uniformly evaporating droplet is defined by (Carrigy et al., 2020) as

$$t_{\mathrm{t,mix}} = \tau_{\mathrm{D}} \left[1 - \left(\sum_{\mathrm{i}} E_{\mathrm{i}} \frac{C_{0,\mathrm{i}}}{\rho_{\mathrm{t,i}}} \right)^{\frac{2}{3}} \right]\ , \qquad (9)$$

where $C_{0,\mathrm{i}}$ is the initial solids concentration of component i and $\rho_{\mathrm{t,i}}$ is the true density of component i.

The term E_{i}, surface enrichment, is the ratio of the concentration of component i, $C_{\mathrm{s,i}}$, to its mean concentration within the droplet, $C_{\mathrm{m,i}}$. In a multi-component system, surface enrichment dictates which component will form the shell and core of the particle, respectively. Surface enrichment is directly related to a dimensionless term, the Péclet number. As the droplet evaporates, the radial concentration of the components depends on the recession rate of the droplet and the diffusion of the solutes from the droplet surface to the center (Vehring et al., 2007). The two mechanisms are responsible for controlling the surface concentration of the solutes. The Péclet number is the ratio of the evaporation rate of the solute, *κ,* to the diffusion coefficient of the solute, *D,* in the solvent:

$$Pe_{\mathrm{i}} = \frac{\kappa}{8D_{\mathrm{i}}} \, . \qquad 10$$

For *Pe*≈1, the diffusivity of the solvent is more rapid than the recession of the droplet surface, causing even distribution of the solute throughout the particle. For a larger *Pe,* where the evaporation rate dominates, the component does not diffuse as quickly, causing it to accumulate near the receding droplet surface. The surface enrichment of a component with a *Pe* smaller than 20 can be approximated using Equation 11 (Vehring et al., 2007), assuming that the solute concentration within the droplet changes at the same rate as the mean concentration:

$$E_i = \frac{c_{\mathrm{s,i}}}{c_{\mathrm{m,i}}} \approx 1 + \frac{Pe_{\mathrm{i}}}{5} + \frac{Pe_{\mathrm{i}}^2}{100} - \frac{Pe_{\mathrm{i}}^3}{4000} \, . \qquad 11$$

Surface enrichment can be used to predict the time required for non-crystalizing solute concentration to reach true density and start forming the shell of the particle. For a component that is expected to crystalize during the drying process, the time at which the shell forms is the time at which the component reaches supersaturation at the surface, $\tau_{\mathrm{s,i}}$, defined as

$$\tau_{s,i} = \tau_{\mathrm{D}} \left[1 - \left(\sum_{\mathrm{i}} \frac{C_{0,\mathrm{i}}}{C_{sol,\mathrm{i}}} E_{\mathrm{i}} \right)^{\frac{2}{3}} \right] , \qquad 12$$

where $C_{0,\mathrm{i}}$ is the initial concentration of component i and $C_{\mathrm{sol,i}}$ is the solubility of component i.

The particle density, ρ_{P}, can be predicted using mass balance Equation 13,

$$\rho_{\mathrm{P}} = C_{\mathrm{f}} \left(\frac{d_0}{d_{\mathrm{v}}} \right)^3 , \qquad 13$$

where C_{f} is the total solids concentration of the formulation, d_0 is the initial droplet diameter, and d_{v} is the volume-equivalent diameter of the dried particle. The volume-equivalent diameter can be calculated from the mass median aerodynamic diameter obtained using an aerodynamic particle sizer. However, the production rate of the monodisperse droplet chain is not large enough for that purpose. Instead, the area-equivalent diameter, d_{p}, was calculated from the scanning electron microscopy images and used to measure the particle density.

The evaporation rate of a pure water droplet at 60 ˚C was calculated to be 3.4×10^{-9} m^2/s. The diffusion coefficients of trehalose and leucine were calculated using the Einstein-Stokes equation; the approximated values were 3×10^{-10} m^2/s and 6.3×10^{-10} m^2/s, respectively. The diffusion coefficient and solubility of Eudragit in the ethanol-water co-solvent system was predicted using a numerical model. The density and solubility of trehalose and leucine in water are considered as 1580 kg/m^3, 690 mg/mL and 1293 kg/m^3, 23 mg/mL, respectively. For Eudragit, the considered density was 841 kg/m^3. Tables 2 and 3 summarize the different particle formation parameters. For simplicity of calculation, the effects of variable viscosity and the evaporation rate were ignored. For trehalose and Eudragit, only the time to reach true density was calculated, since they do not crystalize under normal drying conditions. Since leucine crystalizes and forms the shell within the system, the time to reach supersaturation was calculated. From the calculations, it is apparent that trehalose reaches its true density late in the drying window (>90%) in all the formulations. Formulations containing leucine reached the critical saturation point relatively early in the drying window, actively forming the particle shell with sufficient time for crystal growth. The area-equivalent diameter of the particle, d_p, was calculated by analyzing the scanning electron microscopy images using ImageJ (Schneider et al., 2012). The average diameter of 15 particles was considered for each sample. The standard deviation from the mean was calculated using the variance formula.

Table 2 Calculated Péclet number, surface enrichment, time to reach true density and saturation time for trehalose-leucine formulations. Notations: DC = Droplet Chain, T = trehalose, L = Leucine. Numbers following the letters represent the percentage mass fraction of the respective solute in the formulation.

Formulation	**Concentration (mg/mL)**	Pe_{Tre}	Pe_{Leu}	$E_{\mathrm{ss,Tre}}$	$E_{\mathrm{ss,Leu}}$	$\frac{t_{\mathrm{t,mix}}}{\tau_{\mathrm{D}}}$	$\frac{\tau_{\mathrm{sat}}}{\tau_{\mathrm{D}}}$
DC100T	10	1.4	0.7	1.3	1.1	95.9%	-
DC90T10L						96.2%	86.8%
DC80T20L						96.5%	79.0%

DC50T50L						97.4%	61.5%

Table 3 Calculated Péclet number, surface enrichment and time to reach true density for Eudragit-trehalose formulations. Notations: DC = Droplet Chain, T = trehalose, E = Eudragit. Numbers following the letters represent the percentage mass fraction of the respective solute in the formulation.

Formulation	**Concentration (mg/mL)**	Pe_{Tre}	Pe_{Eud}	$E_{\mathrm{ss,Tre}}$	$E_{\mathrm{ss,Eud}}$	$\frac{t_{\mathrm{t,mix}}}{\tau_{\mathrm{D}}}$
DC100T	10	1.7	13.3	1.4	4.7	95.9%
DC90T10E						96.3%
DC80T20E						95.2%
DC50T50E						92.5%

2.4.1.4 Raman Spectroscopy

Particles were collected directly on the bare surface of SEM stubs for four hours prior to Raman spectroscopy. The particles were scraped from the stub and mounted in the conical cavity of a rectangular metallic slide. The slide was then placed within an enclosed signal collection chamber of a custom-designed dispersive Raman spectroscopy system (Wang et al., 2017a). The setup used a 670 nm diode-pumped solid-state laser. A continuously variable neutral density filter was used to control the laser beam power, and a cryogenically cooled CCD sensor array was used to collect the signal. All the resulting Raman spectra were measured at temperatures of 20 ˚C to 22 ˚C and less than 2% RH.

2.5. Results and Discussion

2.5.1. Calculation of Initial Droplet Diameter

Initial droplet diameters were calculated using the information obtained from the processed images of the interference fringes. For a stationary droplet, the interference pattern appears with constant intensity for fixed droplet size. However, in a moving droplet chain, the intensity can change with even the slightest movement of the droplets from the focal plane, thereby causing minuscule changes in the fringe spacing. The uncertainties of the calculations are expressed as errors, which stayed below 1% of the calculated value. To compare the accuracy of measurement, the phase function of the 100% trehalose formulation, DC100T, obtained from the images was compared to the standard phase function of a droplet of equal diameter generated in Mieplot. The intensity of the experimental phase function was not uniform because of background noise, but the peaks of the function coincided in the generated phase function, confirming the accuracy and precision of this method.

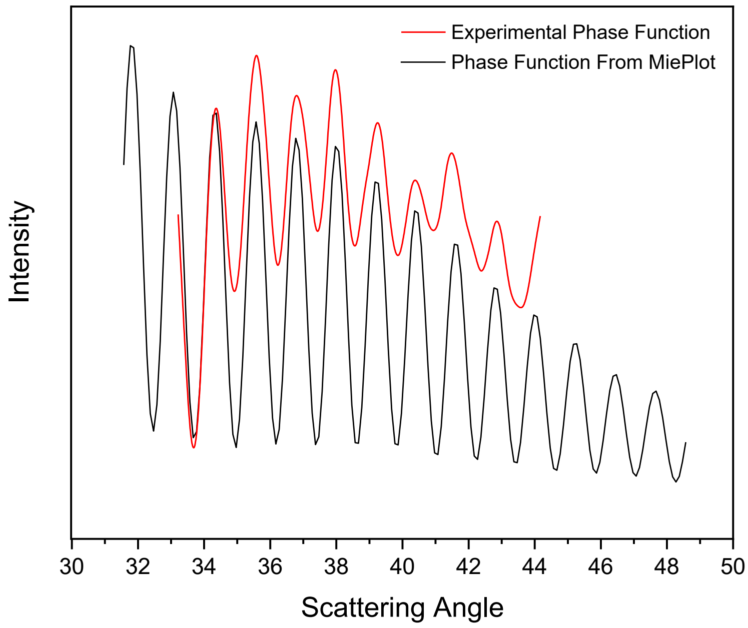

Figure 11: Theoretical angular intensity distribution and experimental phase function for *d_0* =35.07 µm. Differences in peak intensity are caused by background noise in the experimental setup.

2.5.2. Calculation of Particle Density

Since trehalose has a low Péclet number, it usually forms spherical particles with solid centers. The scanning electron microscopy image of the particles, shown in Figure 12, reveals the external surface morphology to be rough with increased buckling and folding at higher leucine content. Individual crystal patches of leucine at the surface can be seen on DC50T50L. The area-equivalent diameter of the particles was measured using ImageJ. Table 4 shows the initial droplet diameter and the area-equivalent diameter and calculated density of the trehalose-leucine particles at different compositions and compares the results with the compressed bulk density of the same particles at 5 kPa and 35.3 kPa (Feng et al., 2011). The calculated density of pure trehalose particles is significantly higher than the compressed bulk density because of the highly cohesive nature of trehalose, which caused it to adhere to the micrometer piston head of the bulk density tester and resulted in high fluctuations in observed density (Feng et al., 2011). Since this technique takes an average of the densities of multiple individual particles, the calculated density varies from the compressed bulk density measurements, as it provides the bulk density of powders under different levels of applied load (Shamsaddini-shahrbabak and Vehring, 2008).

Table 4 Initial droplet diameter, area-equivalent diameter of the particles, calculated particle density and reported compressed bulk density of trehalose-leucine microparticles. Notations: DC = Droplet Chain, T = trehalose, L = Leucine. Numbers following the letters represent the percentage mass fraction of the respective solute in the formulation.

Formulation	**Concentration (mg/mL)**	**Initial Droplet Diameter (μm)**	**Area-Equivalent Diameter of Particle (μm)**	**Calculated Density (kg/m^3)**	**Compressed Bulk Density (kg/m^3) [At 5 kPa] [At 35.3 kPa]**
DC100T	10	35.07±0.31	6.55±0.03	1530± 45	430
					544
DC90T10L		33.24±0.19	7.25±0.18	960±70	788
					853
DC80T20L		33.47±0.38	7.59±0.16	860±60	595
					738
DC50T50L		33.03±0.57	9.65±0.43	400±60	305
					345

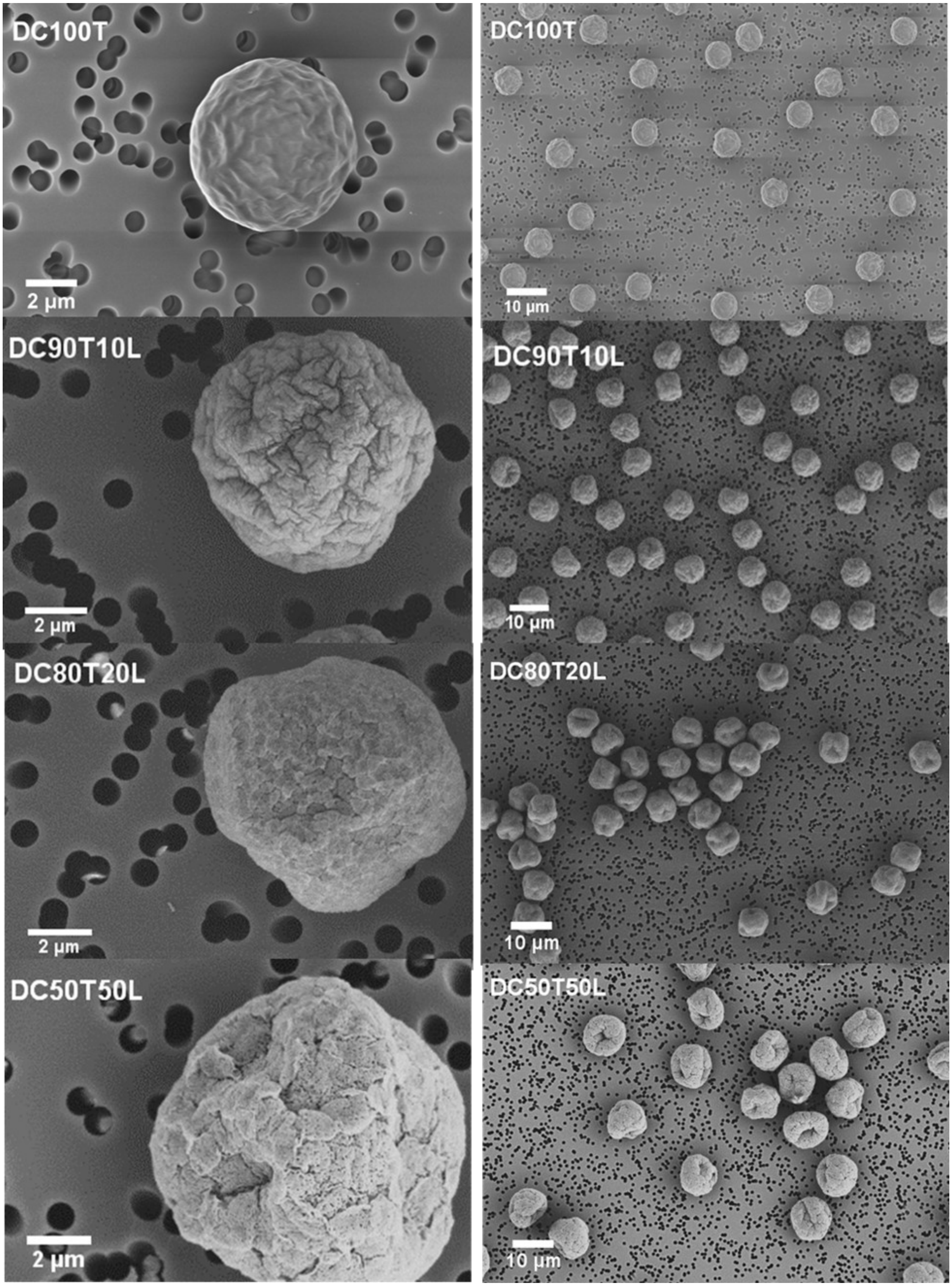
DC100T
2 µm
DC100T
10 µm
DC90T10L
2 µm
DC90T10L
10 µm
DC80T20L
2 µm
DC80T20L
10 µm
DC50T50L
2 µm
DC50T50L
10 µm

Figure 12: Scanning electron microscopy images of particles dried from trehalose-leucine formulations in the monodisperse droplet chain. Preceding numbers denote the percentage fraction of component dissolved in the solvent with respect to total solids content (10 mg/mL). The external particle morphology changed with changing fractions of the solutes, but the sphericity of the particles was preserved. Scale bars are shown separately for each image. Notations: DC = droplet chain, T = trehalose, L = leucine.

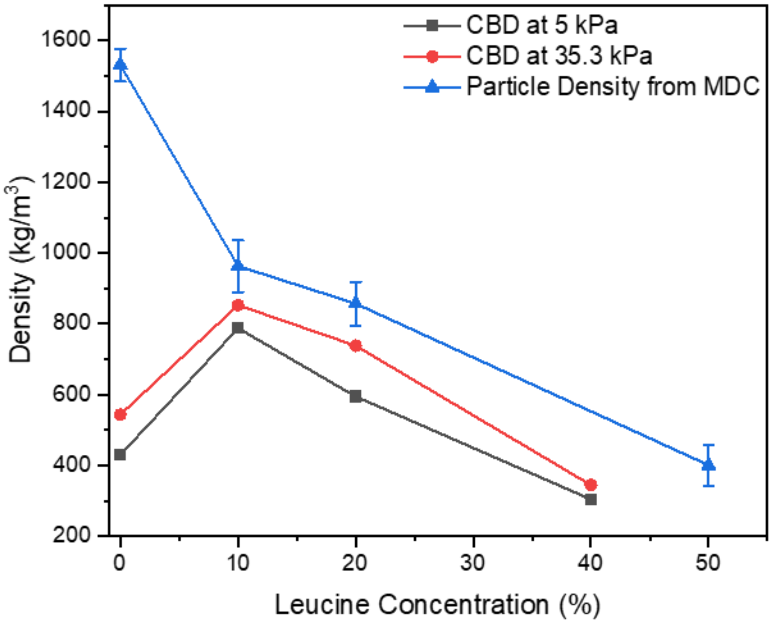

Figure 13: Comparison of calculated particle density and bulk density data from the compressed bulk density tester. Notations: CBD = compressed bulk density, MDC = monodisperse droplet chain.

Figure 14 shows the scanning electron microscopy images of particles formed from Eudragit-trehalose formulations. Eudragit, being a large molecule with a high Péclet number, moves toward the droplet periphery and thus acts as the shell former for the particles. The addition of Eudragit caused the particles to fold and buckle externally, with the degree of deformation depending on the mass fraction of Eudragit in the formulations. Table 5 shows the initial droplet diameter, area-equivalent diameter and calculated density of the Eudragit-trehalose microparticles.

The particles formed from trehalose-leucine formulations exhibited a regular shape with high sphericity, albeit with a visible buckling point at the surface at higher leucine content. The microscopy images at lower magnification showed consistency in particle shape and aspect ratio, which validated the assumption that the area-equivalent diameter of the particles was equal to the volume-equivalent diameter. Although the bulk density of a powder sample is not expected to be the same as single-particle density, Figure 13 shows that the trend of change in density due to the addition of leucine in both measurement techniques move in the same direction. However, measuring the particle density of the Eudragit-trehalose microparticles presented some challenges. Particles with a high Eudragit content (>20%) showed an angular morphology with very low sphericity. Upon examination of the microscopy images, it was observed that the aspect ratio of the particles was dependent on the orientation of the particles resting on the aluminum stubs. As a result, the area-equivalent diameter measured from the images was predicted to overestimate or underestimate the actual volume-equivalent diameter of the particles.

Table 5 Initial droplet diameter, area-equivalent diameter of the particles and calculated particle density of Eudragit-trehalose microparticles. Notations: DC = Droplet Chain, T = trehalose, L = Leucine. Numbers following the letters represent the percentage mass fraction of the respective solute in the formulation.

Formulation	**Concentration (mg/mL)**	**Initial Droplet Diameter (µm)**	**Area-Equivalent Diameter of Particle (µm)**	**Calculated Density (kg/m^3)**

DC100T	10	35.07±0.31	6.55±0.03	1530± 45
DC90T10E		35.99±0.63	10.32±0.64	425± 80
DC80T20E		32.36±0.27	9.86±0.50	350± 55
DC50T50E		30.04±0.61	12.92±2.15	125±65

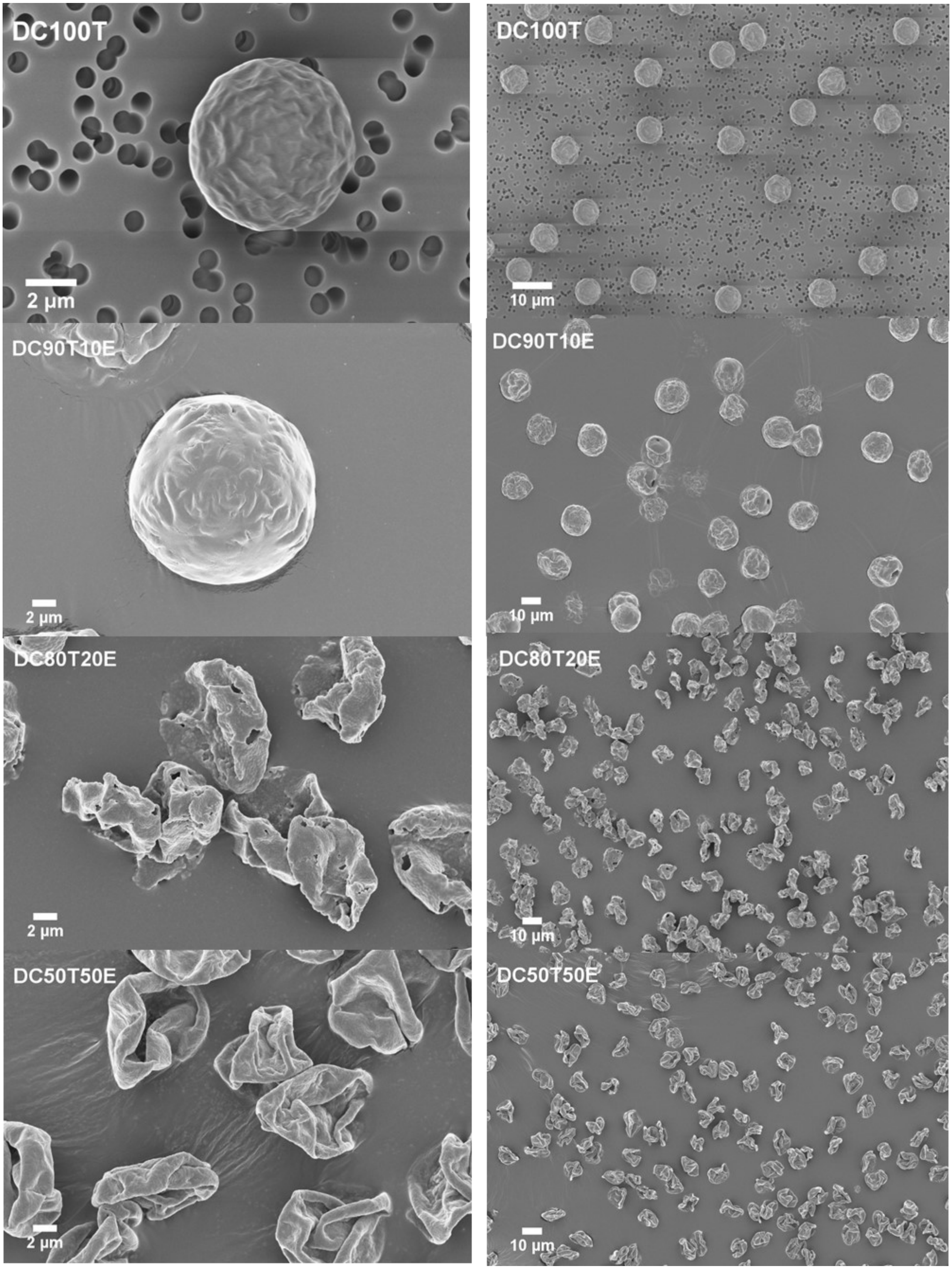
DC100T
2 µm
DC100T
10 µm
DC90T10E
2 µm
DC90T10E
10 µm
DC80T20E
2 µm
DC80T20E
10 µm
DC50T50E
2 µm
DC50T50E
10 µm

Figure 14: Scanning electron microscopy images of particles dried from Eudragit-trehalose formulations made from an iso-compositional ethanol-water mixture and collected from the monodisperse droplet chain. Notations: DC = droplet chain, T = trehalose, E = Eudragit. Particle sphericity and external morphology changed dramatically with increasing Eudragit content in the particles. Scale bars are shown separately for each image.

2.5.3. Raman Spectroscopy

One of the drawbacks of using a monodisperse droplet chain is its low production rate. Theoretically, for a 10 mg/mL formulation, the droplet chain running at 60 Hz is capable of producing 50 µg powder per hour. Dried particles of formulation DC100T were collected for four hours using the impactor. The mass of collected particles was too small to measure accurately, but it was sufficient to be comfortably used for a single measurement by the macro-Raman spectroscopy instrument. Figure 15 shows the Raman spectra of the particles collected from the droplet chain alongside the spectra of spray-dried amorphous trehalose and crystalline trehalose. The spectrum of the particles collected from the droplet chain revealed the presence of both amorphous and crystalline trehalose, which might have been caused by accidental exposure of the particles to ambient conditions.

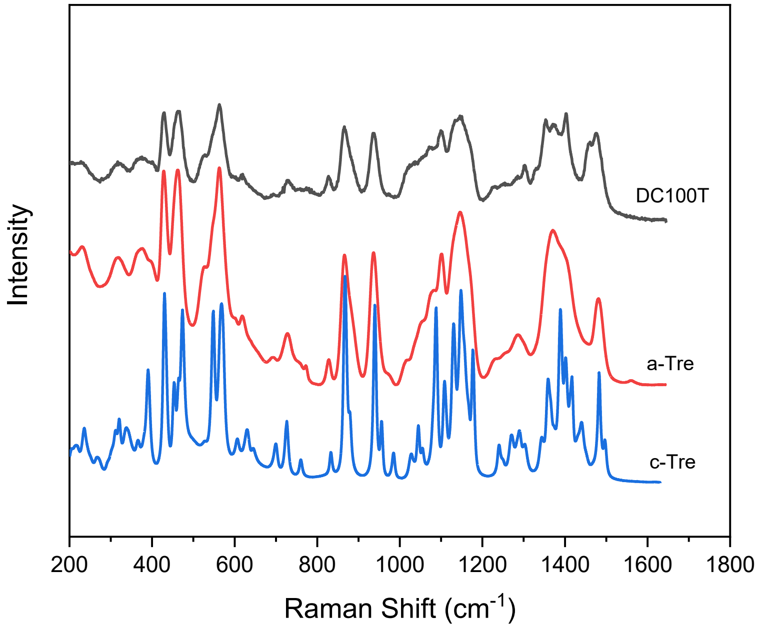

Figure 15: Reference spectra of amorphous and crystalline trehalose and measured spectrum of trehalose particles collected from the droplet chain. The measured spectrum is in good agreement with the reference spectra, showing the presence of a small amount of crystalline component.

Figure 16 shows the Raman spectrum of Eudragit-trehalose composite particles collected from the droplet chain alongside the spectra of spray-dried Eudragit-trehalose microparticles for purposes of comparison. The two sets of spectra show a similarity in the positions of the marker peaks at 865 cm^{-1} and 935 cm^{-1} for amorphous trehalose, and at 835 cm^{-1} and 990 cm^{-1} for amorphous Eudragit.

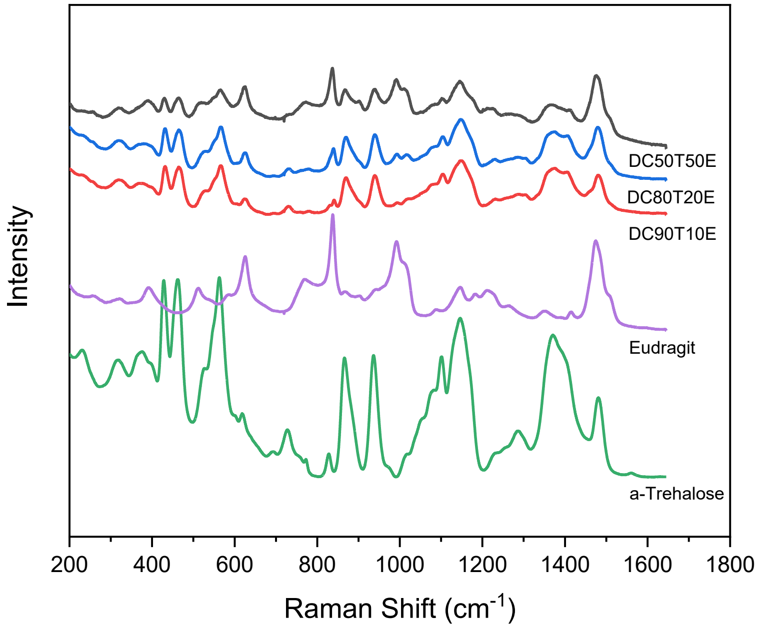

Figure 16: Reference spectra of amorphous trehalose and amorphous Eudragit along with the measured spectra of Eudragit-trehalose formulations at different solids concentrations.

2.6. Conclusion

The capability of the monodisperse droplet chain to investigate particle formation and morphology has been presented above. The instrument is capable of running at a moderately high drying temperature and can be used to measure initial droplet diameter, evaporation rate and particle size, which, along with the help of a particle formation model, can be successfully used to predict the nature of the resulting particles. The integration of interferometric laser imaging into the instrument increased the accuracy and precision of initial droplet diameter measurement. Through the addition of a single-nozzle cascade impactor, the particle collection efficiency of the instrument was also improved, greatly reducing the time required to collect the necessary volume of particles for scanning electron microscopy and Raman spectroscopy. The information obtained from the instrument can be successfully used to predict the density of single particles. However, the accuracy of the measurement depends heavily on the morphology of the particle. For particles with high sphericity, particle density can be predicted accurately, whereas for particles exhibiting low sphericity and the presence of voids such prediction will show some degree of error.

All the modifications to the previous setup make the monodisperse droplet chain a reliable preliminary testing instrument to understand the particle formation process for both pulmonary and enteric drug delivery. Although the process of density calculation is still in its infancy and may present some challenges because of its limitations, the addition of dimensionless shape factors to mitigate the effect of low sphericity would be an interesting next step in the future development of the instrument.

Chapter 3. On the Feasibility of Spray-Dried Eudragit-Trehalose Microparticles for Enteric Delivery of Biologics

3.1. Introduction

Since their commercialization in the 1940s, antibiotics have been widely used to treat and prevent bacterial infections, but the emergence of antibiotic-resistant strains of various bacteria has become a serious global health threat. The World Health Organization has identified antimicrobial resistance as a growing public health threat of broad concern. Multidrug-resistance in *Mycobacterium tuberculosis* and malaria has been detected in multiple countries, and under-reporting of the cases compromises control efforts and jeopardizes recent advances (World Health Organization, 2014). *Escherichia coli, Salmonella* sp.*, Shigella* sp. and *Vibrio cholerae*, bacteria that are responsible for different gastrointestinal infections in humans and animals, have also shown alarming increases in their resistance to antibiotic use (Ashkenazi et al., 2003; Chiu et al., 2002; Glass et al., 1980; Mwansa et al., 2007; Reinthaler et al., 2003; Trung et al., 2005; van den Bogaard et al., 2001; Yoke-Kqueen et al., 2008). Since the development of new small-molecule antibiotics has failed to keep pace with the emergence of resistant strains of bacteria, alternative approaches are badly needed. Biologics, in particular bacteriophages, have the potential to fill the void and become a powerful tool in the treatment of antibiotic-resistant infections, including infectious enteritis. However, bacteriophages require protection from stresses arising from manufacturing and storage conditions in order to maintain potency (Jończyk et al., 2011). With respect to biological formulations for enteric delivery, bacteriophages require protection from the harsh chemical environment of the human stomach caused by the presence of hydrochloric acid and various digestive enzymes, as exposure to these substances can render biologics inactive (Abdelsattar et al., 2019; Koo et al., 2000; Koo et al., 2001).

Eudragit® is the commercial name for a range of polymethacrylate polymers marketed by Evonik Industries Inc. It is synthesized by the polymerization of acrylic acid and methacrylic acid or their esters at varying proportions (Rowe et al., 2009). Depending on their solubility profile, the different types of Eudragit can be divided into three broad classes (Thakral et al., 2013). Cationic Eudragit E, which is soluble below pH 5.5, is used as a film coating for taste-masking applications (Cerea et al., 2004; Drašković et al., 2017). Anionic Eudragit L and S, which are soluble above pH 6 and 7, respectively, have widespread application as enteric coatings for colon-specific drug delivery (El-Malah and Nazzal, 2008). Neutral Eudragit RL, RS (with pH-independent solubility) and NE, NM (with pH-dependent swelling and permeability) are used for sustained drug delivery (Das et al., 2010; Lunter and Daniels, 2012). Because of their ability to release drugs systematically at a targeted pH level, Eudragits are widely used as enteric coatings for tablets (Sauer et al., 2013). Historically, the coating process has employed conventional methods like dry powder coating (Sauer et al., 2013) and solvent evaporation (Perumal, 2001), both of which require heating the polymers for an extended period of time in order for them to coalesce and form the protective coating. When applied to biological dosage forms, any defect or inadequacy in this coating can cause biologics to be inactivated. The survival of biologics can also be threatened by the tablet-making process itself, which involves multiple compressing stages and considerable exposure to environmental and mechanical stress.

Spray drying is an alternative method of producing a dosage form that, unlike conventional multi-step coating processes, requires a single step of droplet drying to form the protective outer shell of the particles. Spray drying is a process used to produce dry powder from a liquid feedstock, usually a solution or a suspension. The liquid feedstock containing dissolved or suspended solids is atomized into small droplets inside a drying chamber, and the droplets are then dispersed in a drying gas flow, where they evaporate and form particles. The dried particles are typically separated from the flow using a cyclone. Spray drying has been successfully applied in the food processing industry for the production of dried dairy and protein products and in taste-masking applications (Bora et al., 2008; Kim et al., 1996; Schuck, 2002). Spray drying is also often used in the pharmaceutical industry to encapsulate active ingredients within dried particles, a process that can provide protection from potentially hazardous environmental factors like temperature and humidity (Carrigy and Vehring, 2019). Spray drying also allows for the design of particles with specific properties suitable for oral and respiratory delivery (Año et al., 2011; De Smet et al., 2014; Kunda et al., 2015; Saboo et al., 2016; Sou et al., 2015). The spray drying of Eudragit on a laboratory scale to encapsulate different small molecule drugs for delivery into the gastrointestinal tract has been reported. Because of its insolubility in water, organic solvents like ethanol, methanol, dichloromethane, or mixtures of them, and aqueous suspensions or dispersions of Eudragit (Amiet-Charpentier et al., 1998) have been used to spray dry in conjunction with active pharmaceutical ingredients such as itraconazole

(Sóti et al., 2015), diltiazem (Kristmundsdóttir et al., 1996), ketoprofen (Rassu et al., 2008), valsartan (Pradhan et al., 2016) and buspirone (Al-Zoubi et al., 2008).

The spray drying of biological actives like bacteriophages for pulmonary delivery has been successfully achieved in the past (Leung et al., 2018a; Matinkhoo et al., 2011; Vandenheuvel et al., 2014). By comparison, studies on powder formulations encapsulating biologics for enteric delivery are relatively scarce. One such study reported the encapsulation of Rhizobacteria (*Pseudomonas fluorescens-putida*) when it was spray-dried using an aqueous dispersion of Eudragit RS 30D without other excipients. A room-temperature stability study showed that the polymer allowed the survival of bacteria for as long as one year in storage (Amiet-Charpentier et al., 1998). However, the ability of Eudragit to protect against an acidic environment was not tested. In another study, an inactivated strain of *Vibrio cholerae* was spray-dried using an aqueous dispersion of Eudragit L 30D and FS 30D without any additional stabilizing agent. *In vitro* release studies showed that less than 5% of the encapsulated bacteria were released in an acidic medium, whereas 80% of the bacteria were released in a neutral medium over 24 hours (Año et al., 2011). A recent study focused on spray drying *Myoviridae* bacteriophage Felix O1 with Eudragit S100 and trehalose at different inlet temperatures (Vinner et al., 2019). Analysis of the produced powders showed a higher phage concentration in pure trehalose particles, but the survival of phages in simulated gastric fluid was much higher in particles containing Eudragit (Vinner et al., 2019). Despite these reported successes, few insights into the actual formation process of the particles, their specific core-shell morphology, and the mechanisms underlying their ability to withstand exposure to the acidic pH of the stomach can be found in the published studies. A better understanding of the particle formation process is needed for a rational design of such particles.

The present study dried solutions of Eudragit® S100 and trehalose to explore the formation process of carrier particles with a polymer shell and a disaccharide core. Since Eudragit has high solubility in organic solvents and a pH-dependent solubility in water, two different feedstocks were prepared for drying at two different solvent formulations: an ethanol-water co-solvent system in which both Eudragit and trehalose had high solubility, and an aqueous system which dissolved both components by using a pH-shifting technique. The results of this study shed light on previously unexplored details of the particle formation process of Eudragit-trehalose systems and the viability of spray-dried Eudragit-trehalose particles as a potential enteric delivery platform for biologics, including bacteriophages, intended for gastrointestinal delivery in humans and animals.

3.2. Material and Methods

3.2.1. Chemicals and Formulations

Three different sets of feed solutions of trehalose dihydrate (Fisher Scientific Ottawa, ON, Canada) and poly (methacrylic acid-co-methyl methacrylate) (Eudragit® S100, Evonik Industries AG, Darmstadt, Germany) were prepared in different solvent compositions in this study. The first set of experiments assessed the influence of different ethanol (Commercial Alcohols, Winnipeg, Canada) and deionized water co-solvent ratios (0.6:0.4, 0.7:0.3, 0.75:0.25 and 0.76:0.24 [w/w]) on particle morphology. Feed solutions of trehalose and Eudragit with a fixed total solids concentration of 10 mg/mL were prepared at a 50:50 ratio. For the second set of formulations, feed solutions of trehalose and Eudragit were prepared using mixtures of ethanol and water at 0.76:0.24 (w/w), the iso-compositional point of the ethanol-water co-solvent system (Ordoubadi et al., 2019). Six formulations of trehalose/Eudragit were prepared with mass fractions of 0.50/0.50, 0.67/0.33, 0.80/0.20, 0.85/0.15, 0.90/0.10, and 0.95/0.05, keeping the total solids concentration fixed at 10 mg/mL. The third set consisted of different Eudragit-trehalose formulations spray-dried with water as the sole solvent. At neutral pH, Eudragit® S100 is insoluble in water. To make the water-based formulations, the pH of the water was initially shifted to the alkaline range (pH = 11) by adding 1M NaOH solution, which facilitated the dissolution of the Eudragit in the solvent. After the Eudragit had dissolved, the pH was readjusted to 7 by adding 0.01M HCl to neutralize the dissolved NaOH, since high alkalinity can be fatal for desired deliverable biologics. Necessary amount of trehalose was dissolved in the neutral solution. Six formulations with mass fractions of trehalose and Eudragit similar to formulations at the iso-compositional point were prepared in water. The pH of the formulations was monitored using a pH meter (Orion ROSS Ultra Semi-micro pH Electrode, Thermo Fisher Scientific, Waltham, MA, USA) at each step in the pH-shifting process.

3.2.2. Monodisperse Droplet Chain

A monodisperse droplet chain, an instrument capable of producing particles of nearly identical size, was used to gain insight into particle formation mechanisms and particle morphology. A simplified schematic is shown in Figure 10; the details of the instrument are described elsewhere (Ordoubadi et al., 2019). Individual droplets of the feed solutions were dispensed inside a transparent, square tube using a piezoelectric droplet generator (Microfab Technologies Inc., Plano, Texas, USA) with a 40 µm orifice.

Droplets were generated at a fixed frequency of 60 Hz. A laminar flow of air at 3 L/min was introduced at one end of the tube to dry the droplets, keeping the temperature at the inlet constant at 21 ˚C. The setup was improved for this study by using a laser interferometry technique to measure the initial droplet diameter more accurately at the inlet. A collimated laser beam (Process Instruments, Salt Lake City, Utah, USA) with a wavelength of 671 nm was passed through the stream of falling droplets at the inlet. A camera (GO-5000M-USB, JAI Inc., San Jose, CA, USA) placed at a fixed distance from the droplet chain was used to collect the angular phase function generated by the light scattered by the droplets. Captured phase functions were processed using MATLAB (MathWorks Inc., Natick, MA, USA) to determine the average spacing between the consecutive maxima of the angular scattering patterns. The initial droplet diameter was calculated using Equation 14 (Hesselbacher et al., 1991),

$$d = \frac{2\lambda}{\Delta\theta_c}\left(\cos\left(\frac{\theta}{2}\right) + \frac{m\sin\left(\frac{\theta}{2}\right)}{\sqrt{m^2 - 2m\cos\left(\frac{\theta}{2}\right) + 1}}\right)^{-1}, \qquad 14$$

where λ is the laser wavelength, $\Delta\theta_c$ is the angular spacing of the maxima in the angular scattering pattern, θ is the scattering angle, m is the refractive index of the droplet material, and d is the diameter of the droplet. In this study, the scattering angle was set at 43˚. Ethanol and water have similar refractive indices at room temperature (1.361 and 1.333), therefore, the change in refractive index of the solvent with varying proportions of ethanol and water was assumed to be insignificant. The refractive index of all the formulations was assumed to be equal to the refractive index of water at 25 ˚C.

3.2.3. Polydisperse Spray Drying

Spray drying was used to produce larger batches of powder (2-3 g per batch) for the dissolution analysis. Six feed solutions were prepared, each with a fixed total solute concentration of 20 mg/mL. Combinations of mass fractions of trehalose/Eudragit of 0.80/0.20, 0.85/0.15, 0.90/0.10, 0.95/0.05, 0.97/0.03 and 0.99/0.01 were dissolved in water by using the pH-shifting technique described in the previous section. A custom research spray dryer (Ivey et al., 2016) along with a custom twin-fluid atomizer was used to spray dry the formulations. The atomizer was operated at an air-to-liquid ratio of 20, which corresponded to a mass median initial droplet diameter of approximately 5.5 µm (Hoe et al., 2014). The relevant spray drying parameters were calculated using a mass and energy balance model (Ivey and Vehring, 2010). The drying gas temperature was set to 100 ˚C for efficient drying of the droplets. The outlet temperature was limited to 58.4 ˚C to reduce thermal stress at the outlet of the cyclone. Similarly, outlet humidity was limited to 3.4% to prevent crystallization of the powder during collection. The feedstocks were supplied to the atomizer using a peristaltic pump (Cole-Parmer, Montreal, QC, Canada) at 1.7 mL/min, with a fixed drying gas flow rate of 400 SLPM. The collected powders were bottled in airtight glass vials and stored under dry conditions at ambient temperature for subsequent analysis. The morphology of the spray-dried particles was examined using scanning electron microscopy.

3.2.4. Computation of Particle Formation Parameters

Particle formation in a co-solvent system with two solutes is a complex process. As multiple solvents evaporate, the dissolved solutes are precipitated sequentially according to their solubility, solid phase, density, and diffusivity, leaving behind the solid particles. To understand the particle formation process in the studied co-solvent systems, a numerical model for multi-solvent microdroplet evaporation first described by Ordoubadi et al. (2019) was used. The internal distribution of solutes in the evaporating droplets dictates the morphology of the dried particles (Boraey and Vehring, 2014; Vehring et al., 2007). This distribution depends on both the rate of evaporation of the droplet over time, and the rate of diffusion of the solutes inside the droplet. The effect of these counteracting mechanisms can be expressed by the Péclet Number, which is defined as the ratio of evaporation rate to the diffusion coefficient of each component, $D_{i,}$ as shown below (Vehring, 2008):

$$Pe_i = \frac{\kappa}{8D_i}\,. \qquad 15$$

The evaporation rate, κ, which describes the instantaneous rate of shrinkage of the droplet surface area, was calculated from the numerical model for the multi-solvent system studied here. For small Péclet numbers, the diffusional motion of the solute molecule within an evaporating droplet, i, is relatively fast compared to the recession speed of the droplet surface. This ensures uniform distribution of solute throughout the droplet, resulting in solid, spherical particles, provided that the solutes are not surface-active and do not have low solubility (Ordoubadi et al., 2021b). Large Péclet numbers of solute molecules, as in the case of polymers like Eudragit, are caused by their large size, which restricts the movement of the molecules within the droplet and slows diffusion compared to the recession of the droplet surface. As a result, the solute enriches near the surface of the droplet and typically forms particles with hollow centers and thick shells.

The Einstein-Stokes equation was used to approximate the diffusion coefficient of the components in a single solvent based on molecular size. Assuming spherical molecules, the molecular radius of Eudragit was approximated from its bulk density data to be 3.15 nm. The molecular radius of trehalose, obtained from its molecular volume (Edward, 1970), was calculated to be 0.41 nm. To approximate the diffusion coefficient of each solute in a well-mixed co-solvent system, a mass-weighted average of the binary diffusivities in different solvents was considered. This assumption does not provide an accurate molecular diameter of the polymer; however, the approximation is suitable for predicting the Péclet number of the large polymer molecule (125 kDa), which is almost an order of magnitude higher than that of trehalose.

Due to surface enrichment, the component with a higher Péclet number will typically solidify first near the droplet surface, whereas the component with a lower Péclet number will solidify throughout the droplet, including the core, at a later stage. In a co-solvent system with a highly volatile component, such as ethanol, the evaporation rate and the diffusion coefficients do not remain constant over time, resulting in a time-varying Péclet number (Ordoubadi et al., 2019). Therefore, in this study, the internal solute profiles during drying were predicted through a numerical solution of the internal mass transfer equation as explained elsewhere (Ordoubadi et al., 2019).

The shell thickness is a critical parameter for assessing how well the core of a particle will be protected within an acidic environment. For droplets containing high Péclet number solutes, the shell thickness of the dried particles can be approximated using particle formation theory (Boraey and Vehring, 2014). At the predicted instance of shell formation, the droplet diameter is considered to equal the volume-equivalent diameter of the particle, assuming that the remaining solvent in the interior evaporates through the shell without causing further shrinkage. The remaining solutes on the interior of the droplet will increase the shell thickness due to mass flux towards the interior of the wall during continuing evaporation. Assuming that all of the solute mass concentrates as a thin shell at the end of the evaporation process, and estimating the average shell density, ρ_{sh}, from the true density of the solute, the internal particle diameter, d_{sh}, can be expressed as (Boraey and Vehring, 2014)

$$d_{\mathrm{sh}} = d_{\mathrm{v}}\left(\sqrt[3]{1-\frac{\rho_{\mathrm{p}}}{\rho_{\mathrm{sh}}}}\right), \qquad 16$$

where d_{v} is the volume equivalent diameter of the particles and ρ_{p} is the calculated particle density, which can, in turn, be expressed as

$$\rho_{\mathrm{P}} = C_{\mathrm{f}}\left(\frac{d_0}{d_{\mathrm{v}}}\right)^3, \qquad 17$$

where C_{f} is the total solids feed concentration. For a multi-component system, the true density of the shell, ρ_{sh} can be estimated using Equation 18,

$$\rho_{\mathrm{sh}} = \frac{1}{\sum_i \frac{Y_i}{\rho_i}}, \qquad 18$$

where ρ_i and Y_i are the true density and mass fraction of the component $i.$ The shell thickness of the particle, l_{sh} can then be represented as

$$l_{\mathrm{sh}} = \frac{d_{\mathrm{v}} - d_{\mathrm{sh}}}{2}, \qquad 19$$

where d_{v} is the volume-equivalent diameter of the particle at the onset of shell formation at the surface.

Using the calculated surface enrichment results, it is possible to approximate the time required for the solute surface concentration to reach true density and form the shell of the particle in the case of a constant evaporation rate. The time at which co-solidification of a multi-component amorphous mixture occurs, $t_{\mathrm{t,mix}}$, is defined as (Carrigy et al., 2019)

$$t_{\mathrm{t,mix}} = \tau_{\mathrm{D}} \left[1 - \left(\sum_{\mathrm{i}} E_{\mathrm{i}} \frac{C_{0,\mathrm{i}}}{\rho_{\mathrm{t,i}}} \right)^{\frac{2}{3}} \right], \tag{20}$$

where $C_{0,i}$, is the initial solids concentration of component i, $\rho_{\mathrm{t},i}$ is the true density of component i, and $\tau_{\mathrm{D}} = \frac{d_0^2}{\kappa}$ is the droplet lifetime.

The model assumes co-solidification to occur after the mixture reaches true density at the surface. For the calculation, the true densities of trehalose and Eudragit S100 were 1580 kg/m^{-3} (Grasmeijer et al., 2016) and 841 kg/m^{-3} (Evonik Industries, 2012), respectively.

The model was also used to estimate the particle density using the calculated volume-equivalent diameter of the particles and the true density of the mixture as calculated by Equation 18. The particle morphology can then be predicted using the ratio of particle density and the true density of the mixture (Carrigy et al., 2020). If this value is considerably smaller than 1, the particles are expected to be hollow, which may lead to their buckled or wrinkled morphologies because the shells lack mechanical strength to maintain spherical shape; the particles are also expected to have a smaller diameter than the predicted value. For values closer to 1, the particles are expected to be solid and spherical.

3.2.5. Field Emission Scanning Electron Microscopy

Particles obtained from the monodisperse droplet generator technique and spray drying were analyzed for morphology differences based on formulation differences. The dried particles produced by the monodisperse droplet generator were collected at ambient conditions using a single-nozzle impactor (Wang et al., 2017b). This custom impactor consists of several removable stages with different cutoff diameters ranging from 21 µm to 0.6 µm. Based on the predicted particle diameter, the impactor was configured with two suitable stages. The outlet of the impactor was connected to a vacuum pump which provided an air flow of 3 L/min. The dried particles impacted directly onto the surface of removable aluminum SEM pin mounts (Ted Pella, Inc.; Redding, CA, USA) covered by carbon tape, which was used for scanning electron microscopy imaging without further sample transfer. Particles produced by spray drying were manually transferred from a collection bottle to the carbon tape-covered surfaces of the aluminum mounts within a dry environment. Prior to imaging, the samples were coated with a mixture of 80% gold and 20% palladium to a thickness of approximately 10-15 nm using a sputter coater (Leica ACE600 Carbon/Metal Coater; Concord, ON, Canada). The particles were imaged by a field emission scanning electron microscope (Zeiss Sigma FESEM, Oberkochen, Germany) with an immersion lens (in-lens) detector operated at an accelerating voltage of 3.00 to 5.00 kV and using magnifications of 1000x to 5000x at a working distance of 5 mm to 6 mm.

3.2.6. Dissolution Test using Shadowgraphic Imaging Technique

A new shadowgraphic imaging method and associated instrument were used to analyze the dissolution rate of the spray-dried powders in two solutions at different pH. 300 mg of each spray-dried powder was added to 20 mL of 0.01M hydrochloric acid (pH = 2.0) and 1μM of sodium hydroxide solution (pH = 8) separately in glass vials. The suspensions were stirred with a magnetic stirrer for extended periods of time (one hour for HCl, two hours for NaOH). The imaging instrument (Wang et al., 2018) consisted of a high-resolution camera (SP-5000M-PMCL, JAI Inc., San Jose, CA, USA), fitted with a 16mm fixed-focal-length lens (Edmund Optics Inc., NJ, USA), which took sequential shadowgraphic images of the liquid samples. A 2D collimated LED backlight (Advanced Illumination Inc., Rochester, VT, USA), which was connected to a high-output strobe controller (Pulsar 320, Advanced Illumination Inc., Rochester, VT, USA) and a two-channel function generator (AFG1022, Tektronix Inc., Beaverton, OR, USA) that synchronized the camera and the LED backlight, was used to illuminate the glass vial containing the suspension in a bright field. To avoid interference from external light sources, all optical components were enclosed in a light-blocking sample chamber. The interior of the chamber was covered with light-absorbing material in order to minimize interference by reflected light rays. The acquired images were processed to obtain the normalized relative transmission intensity, $\Delta T_{t,h}^{\mathrm{N}}$, and the transmission coefficient, $\sigma(t)$, as a function of time. Normalized relative transmission intensity was calculated using the following equation (Wang et al., 2018),

$$\Delta T_{t,h}^{\mathrm{N}} = \frac{\Delta T_{t,h}}{\Delta T_{\mathrm{Clear}}^{\mathrm{a}} - \Delta T_{t_0,h}^{\mathrm{a}}}, \tag{21}$$

where $\Delta T_{t,h}$ is the measured relative transmission, $\Delta T_{\mathrm{Clear}}^{\mathrm{a}}$ is the transmission through a clear control medium and $\Delta T_{t_0,h}^{\mathrm{a}}$ is the initial transmission through the sample.

The transmission coefficient is the integral of the normalized relative transmission intensity over the sample height, h, and indicates the overall change in transmission intensity over time as a dimensionless number ranging from 0 to 1.

$$\sigma(t) = \int_{h=0}^{h=1} |\Delta T_{t,h}^{\mathrm{N}}| \; . \qquad 22$$

In cases where a sample is insoluble in a given medium, the transmission of light through the suspension will remain unchanged, resulting in a constant transmission coefficient. By contrast, when a sample slowly dissolves in a given medium, the corresponding coefficient increases with the transmission of light through the suspension. Although the associated setup is used for measuring colloidal stability of suspensions, the introduction of a stirrer canceled the effect of collected particle sedimentation and creaming, thus attributing the change in transmission coefficient to the change in suspension concentration. The change in transmission coefficient can also be attributed to other factors, such as a change in suspension concentration and particle size, and the refractive index of the particles or the fluid. The suspension concentration has an inverse relationship with the transmission coefficient, since the relative transmission of light through the glass vials, and consequently the transmission coefficient, increases as the suspension concentration decreases. However, due to the influence of the other factors mentioned, this technique is semi-quantitative. OriginLab (Northampton, MA, USA) was used to perform regression on the transmission coefficient curves.

3.2.7. Raman Spectroscopy

All suspension samples in the acidic medium were filtered after the dissolution test. The residual sludges for the cases in which the suspended particles did not dissolve completely were washed with deionized water and further filtered and dried in a vacuum chamber. To evaluate the protection of trehalose provided by a Eudragit coating in the acidic environment, a solid-phase analysis of the residual mass was conducted using a custom-designed dispersive Raman spectroscopy system (Wang et al., 2017a). Samples were loaded in the conical cavity of a rectangular metallic slide and then placed in an enclosed signal-collection chamber. The setup used a 670 nm diode-pumped solid-state laser. A continuously variable neutral-density filter was used to control the laser beam power, while a cryogenically cooled CCD sensor array was used to collect the signal. All the resulting Raman spectra were measured at temperatures of 20 to 22 ˚C and less than 2% RH. The spectra of the samples were deconvoluted for quantification of amorphous and crystalline components using methods explained elsewhere (Vehring, 2005).

3.3. Results and Discussion

3.3.1. Particle Formation in Co-solvent System

3.3.1.1 Effect of Co-solvent Ratio on Particle Formation

To apply the particle formation model, it is first necessary to determine the evaporation rate for the different solvent systems used in this study. The calculation of evaporation rate of the droplets was calculated using method explained elsewhere (Ordoubadi et al., 2019). The droplet surface area normalized by the initial droplet surface area as a function of time was determined for different ethanol contents and plotted in Figure 17. The slopes of the plots are the evaporation rates. To allow for direct comparison, the time axis was normalized by the square of the initial diameter, which is proportional to the time it takes droplets with the same evaporation rate to evaporate completely. It is apparent that the evaporation rate is a function of solvent composition and is not constant throughout the life of the droplets for most compositions. At a higher water content, the evaporation rate decreases, indicating a change in composition over time. However, as the solvent composition approaches the isocompositional point of the water-ethanol mixture, the evaporation rate becomes constant, i.e., the mixture behaves like a single-component solvent.

The multi-solvent microdroplet evaporation model also provided the average solvent composition as a function of time. Because of a lack of experimental literature data, the solubility of Eudragit at different water-ethanol co-solvent ratios was calculated using a log-linear approximation. Both solubility and ethanol mass fraction are plotted as a function of time in Figure 18. It is apparent that the solubility of Eudragit at any given point in time strongly depends on the mass fraction of ethanol remaining in the droplet. Formulations with decreasing ethanol content showed a rapid drop in the solubility of Eudragit as the mass fraction of ethanol decreased. However, for the composition at the isocompositional point, the solubility of Eudragit in the solvent was relatively high and stayed constant until the end of the drying process.

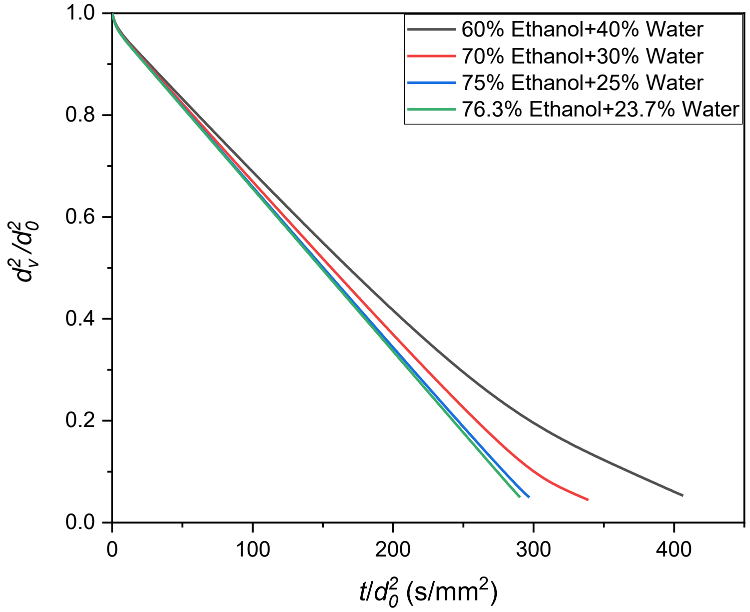

Figure 17: The normalized surface area of ethanol-water droplets at different compositions evaporating at 21 ˚C as a function of time. The slope of the curves is a measure of the evaporation rate.

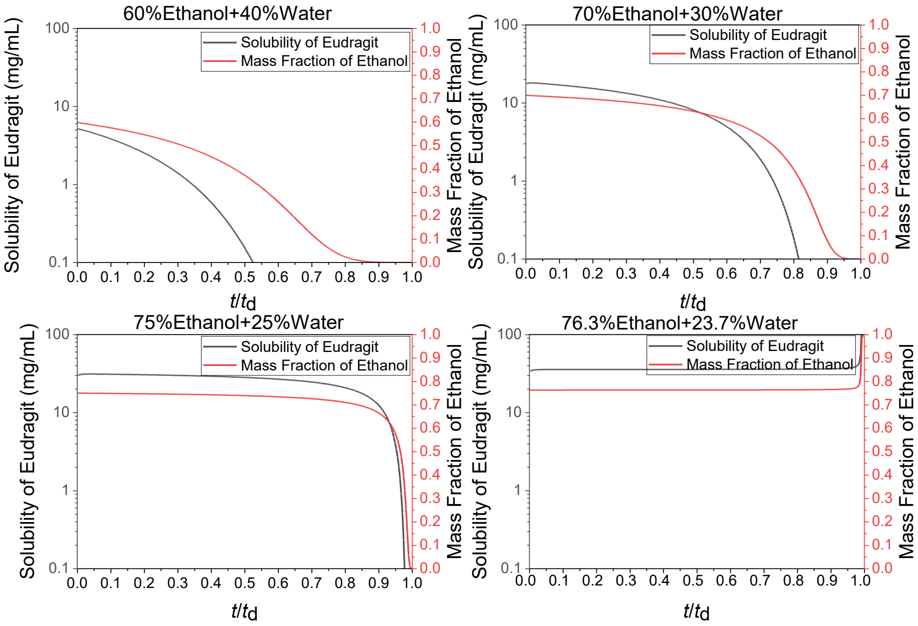

Figure 18: The effect of ethanol mass fraction in the co-solvent (red lines) on the solubility of Eudragit (black lines), shown as a function of normalized time for the evaporating droplets.

The concentration of Eudragit on the surface of the droplet was modelled to predict the onset of shell formation. Figure 19 shows the Eudragit surface enrichment, i.e., the surface concentration normalized by the average concentration, as a function of normalized time for different co-solvent compositions. A higher surface enrichment is desirable for the formation of a core-shell structure. However, the surface enrichment at the lower ethanol content showed a reduction in the later phases of evaporation, where the co-solvent composition shifted towards water and the evaporation rate decreased. This is because surface enrichment is a direct function of the Péclet number and feedstocks with lower ethanol content will lead to water-enriched droplets in the later phases of droplet drying. Despite the low solubility of Eudragit in water, the much slower

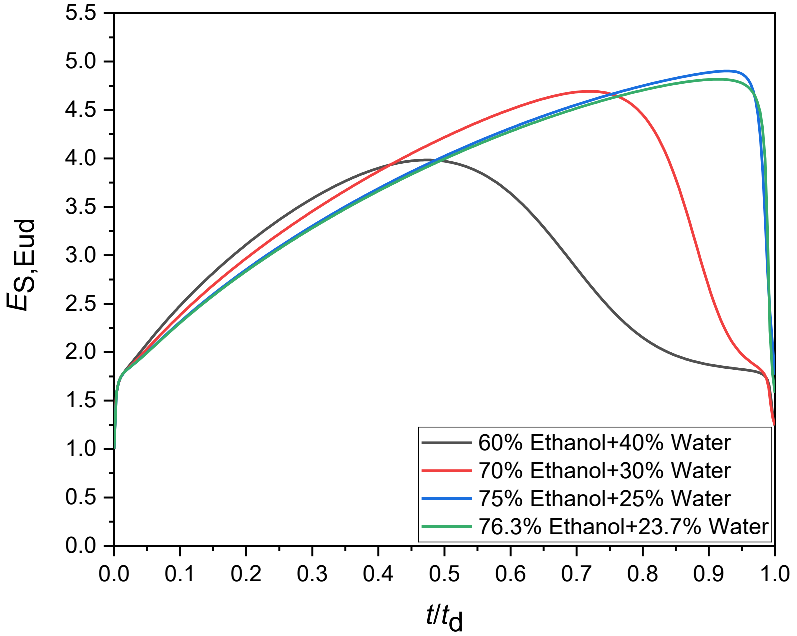

evaporation rate of water than of ethanol is primarily responsible for the reduced surface enrichment. At or near the iso-compositional point the Péclet number remained steady, resulting in a continuous increase in surface enrichment over time towards the maximum value. For proper coating of particles, a higher surface enrichment of Eudragit is required, which in turn requires a solvent prepared close to the iso-compositional point of ethanol-water mixture.

Figure 19: Surface enrichment of Eudragit at different solvent compositions as predicted by a numerical. Surface enrichment was a function of the Péclet number at any given time. The change became steady and reached a peak at the iso-compositional point of the water-ethanol mixture.

Table 6 shows various parameters related to shell formation that were calculated using the particle formation model for a Eudragit-trehalose binary system at a ratio of 50:50 dried in the monodisperse droplet chain. For these calculations, it was assumed that Eudragit remained amorphous and commenced shell formation when the true density of the mixture was reached at the surface. All the formulations took more than 90% of the droplet lifetime to reach their true density, a consequence of the low initial feed concentration. The particle density was calculated according to Equation 17. The results predicted low-density particles, especially for the co-solvent ratios at or near the iso-compositional point. The true density of the mixture of Eudragit and trehalose was estimated with Equation 18 using the predicted mass fractions of the components at the surface at the time of true density. The normalized $\rho_{\mathrm{P}}/\rho_{\mathrm{t,mix}}$ values predicted the particles to be hollow and likely wrinkled. The shell thickness was approximated using Equation 19. It decreased slightly with increasing ethanol content in the formulations.

Table 6 Results of the particle formation modeling for parameters related to shell formation for different solvent compositions and a Eudragit-trehalose ratio of 50:50. Shown are time to reach true density ($t_{\mathrm{t,mix}}$) on the surface, normalized by the droplet life time ($t_{\mathrm{t,mix}}/\tau_{\mathrm{D}}$); predicted particle density (ρ_{P}); true density of the excipient mixture ($\rho_{\mathrm{t,mix}}$); normalized particle density ($\rho_{\mathrm{P}}/\rho_{\mathrm{t,mix}}$); and estimated shell thickness of the particles.

Solvent Composition	$\frac{t_{\mathrm{t,mix}}}{\tau_{\mathrm{D}}}$	ρ_{P}	$\rho_{t,\mathrm{mix}}$	$\rho_{\mathrm{P}}/\rho_{\mathrm{t,mix}}$	**Shell Thickness**

Ethanol (%)	**Water (%)**		**(kg m^{-3})**	**(kg m^{-3})**		**(μm)**
60	40	0.99	700	1020	0.70	0.75
70	30	0.95	650	1000	0.65	0.60
75	25	0.91	300	940	0.32	0.50
76.3	23.7	0.92	300	940	0.32	0.50

Figure 20 shows the scanning electron microscopy images of the particles collected from the monodisperse droplet chain experiments corresponding to the cases listed in Table 6. Upon drying, trehalose forms smooth spherical particles. The addition of Eudragit to the formulations visibly changed the particle morphology as Eudragit enriched the particle surface. Although the particles are not spherical, they appear to be monodisperse, with consistent morphology. In all cases, the particles show a similarly folded, non-spherical structure with low particle density due to external void space, as predicted by the values of $\rho_{\mathrm{P}}/\rho_{\mathrm{t,mix}}$ in Table 6. In all considered solvent compositions, the Péclet number of Eudragit was much larger than that of trehalose. As a result, Eudragit preferentially accumulated on the surface of the droplets and subsequently formed large, hollow particles with a thin shell, as predicted. Assuming that the fold thickness of the particles in the SEMS was about twice the shell thickness, the shell thickness was estimated to be between 500 and 650 nm, a good agreement with the predictions reported in Table 6. The SEMs also reveal a visible increase in the projected particle area with increased ethanol content, demonstrating early shell formation and thinner shell thickness considering the same solid content of the formulations.

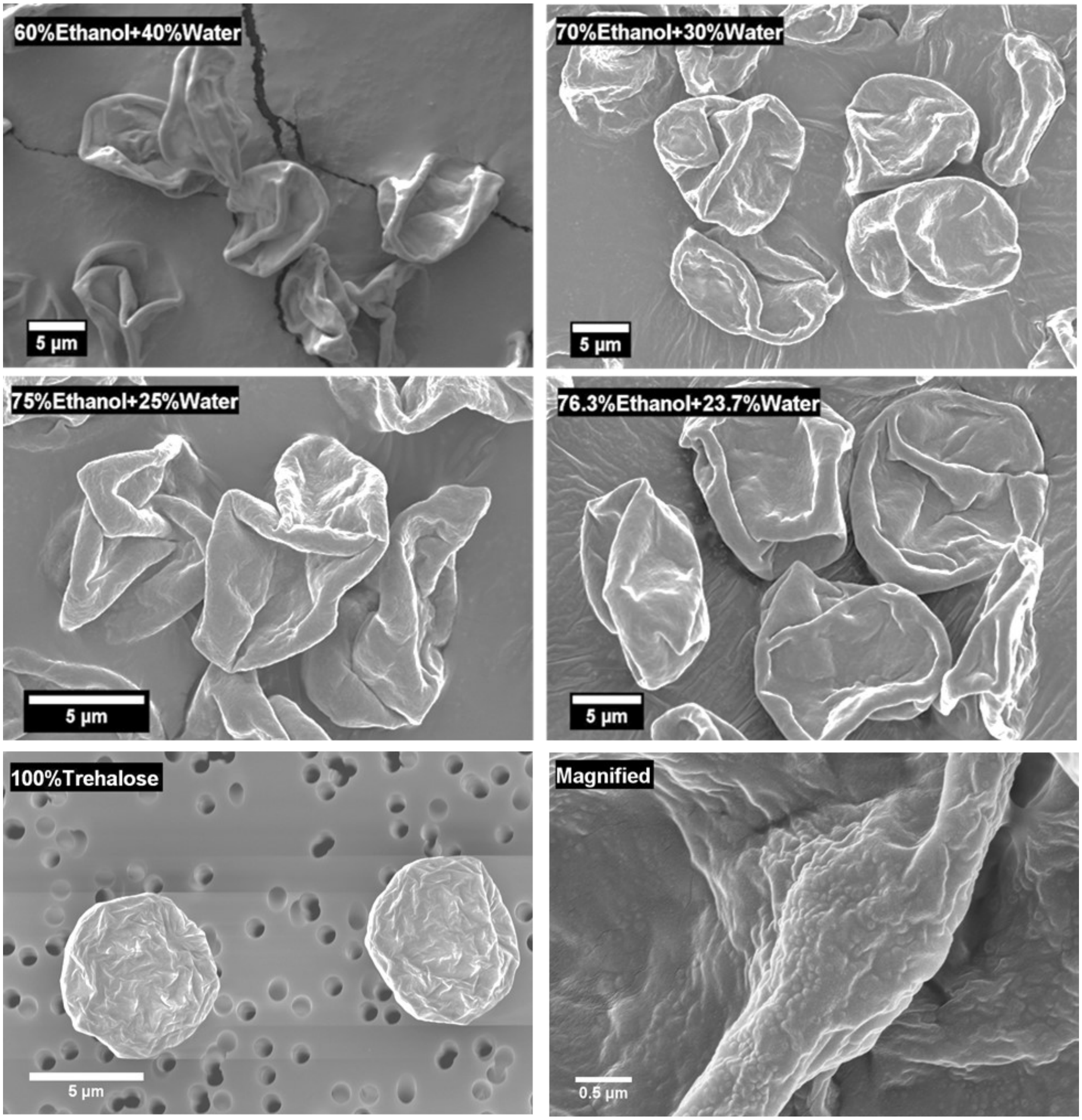

Figure 20: Scanning electron microscopy (SEM) images of particles collected from the monodisperse droplet chain dried at a gas temperature of 21 ˚C. The solvent compositions were changed keeping the total excipient concentration constant at 5 mg/mL each of Eudragit and trehalose. The external morphology showed extremely folded particles for all four solvent compositions. Comparing the SEMs to solid spherical trehalose particles suggests the presence of Eudragit at the surface of the particles. The SEM at the bottom right corner shows a magnified image of a microparticle with the thickness of the shell at the fold. Scale bars are shown separately for each image.

A particle with sufficient protection against a low pH environment must have a shell that consists primarily of Eudragit rather than trehalose. Shell composition can be predicted by modelling the concentration of the excipients as a function of radial coordinate in the droplets. Figure 21 shows the radial profiles of the mass fractions of Eudragit and trehalose within the particles at the time when shell formation is predicted to begin, calculated using the particle formation model. The radial coordinate *r* was normalized by the droplet radius, *R*. It is apparent from the figure that the highest concentrations of Eudragit at the surface were achieved with the formulation at or near the iso-compositional point. This finding indicates that this co-solvent composition is beneficial for protecting the core of the particles with Eudragit.

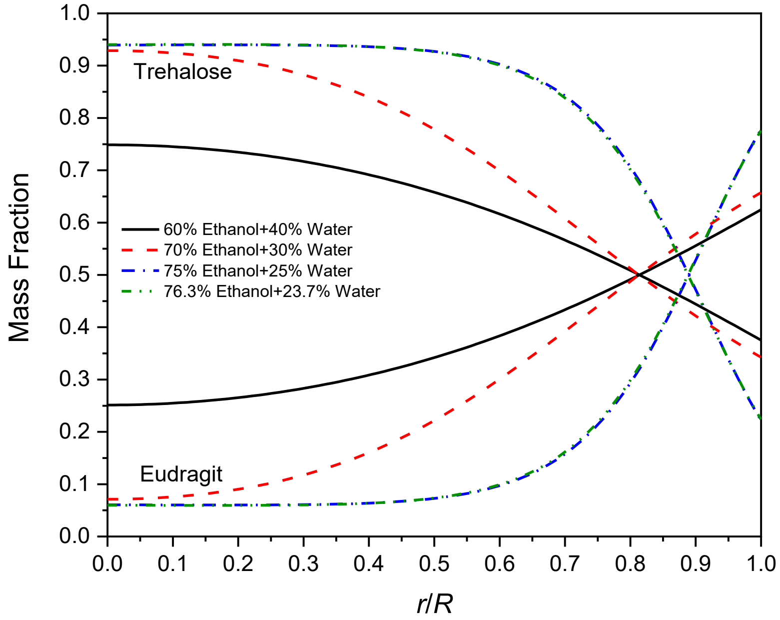

Figure 21: Radial distribution of components within the evaporating droplets for different solvent compositions at the time shell formation is predicted to commence. More Eudragit

reached the surface at higher Ethanol compositions because of higher surface enrichment.

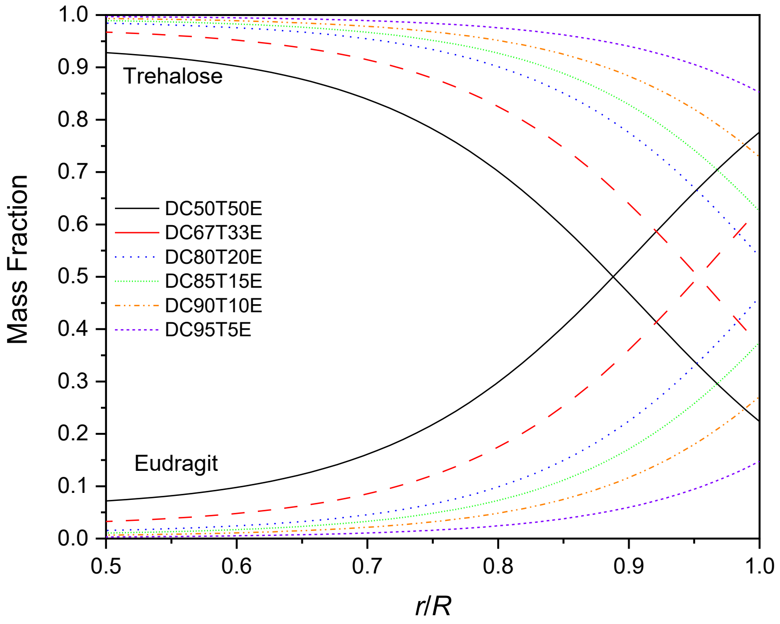

Figure 22: Radial distribution of components within the evaporating droplets in an ethanol-water co-solvent at the iso-compositional point. Particles with higher Eudragit content had more polymer at the surface.

3.3.1.2 Effect of Excipient Mass Fraction on Particle Formation

The next question that needs to be addressed is how much Eudragit in the formulation is required for the formation of a protective shell. Calculations for particle formation at the iso-compositional point for varying ratios of trehalose and Eudragit provide a deeper insight into the effect of the excipient ratio on the particle morphology. The radial distribution of the excipients within the droplets was calculated at the time the surface concentration was predicted to reach the true density of the mixture. The results as a function of normalized radius are shown for the outer regions of the droplet (*r*/*R* > 0.5) in Figure 22. With increasing trehalose fractions the Eudragit concentration at the surface gradually decreased. For the three formulations with the lowest Eudragit fraction up to 15%, trehalose remained the predominant component on the surface, a situation unlikely to lead to the formation of a Eudragit shell.

The calculations presented in Table 7 also predicted a gradually decreasing shell thickness with decreasing Eudragit fractions in the particles. Normalized particle density values, $\rho_{\mathrm{P}}/\rho_{\mathrm{t,mix}}$, predicted the particles would become more spherical with decreasing Eudragit content. All of these findings are consistent with the morphology of the particles as illustrated by the SEM images shown in Figure 23. For the case studied here, a Eudragit mass fraction of less than 15% did not lead to the desired core-shell morphology. However, this is true only for the low drying gas temperature of 21 °C used in the droplet chain apparatus; spray dryers typically use much higher drying gas temperatures.

Table 7 Results of the particle formation modeling for parameters related to shell formation for different Eudragit-trehalose ratios at the iso-compositional composition of ethanol-water. Shown are time to reach true density ($t_{t,mix}$) on the surface, normalized by the droplet lifetime, ($t_{t,mix}/\tau_D$); predicted particle density (ρ_P); true density of the excipient mixture ($\rho_{t,mix}$); normalized particle density ($\rho_P/\rho_{t,mix}$); and estimated shell thickness of the particles collected from the monodisperse droplet chain at 21 ˚C. Notations: DC = Droplet Chain, T = trehalose, E = Eudragit. Numbers following the letters represent the percentage mass fraction of the respective solute in the formulation.

Formulation	$\frac{t_{\mathrm{t,mix}}}{\tau_{\mathrm{D}}}$	ρ_{P} **(kg m^{-3})**	$\rho_{t,\mathrm{mix}}$ **(kg m^{-3})**	$\rho_{\mathrm{P}}/\rho_{\mathrm{t,mix}}$	**Shell Thickness (µm)**

DC50T50E	0.93	310	940	0.33	0.65
DC67T33E	0.94	410	1020	0.40	0.50
DC80T20E	0.95	560	1120	0.5	0.49
DC85T15E	0.96	660	1190	0.55	0.50
DC90T10E	0.97	760	1280	0.59	0.38
DC95T5E	0.97	960	1400	0.69	0.20

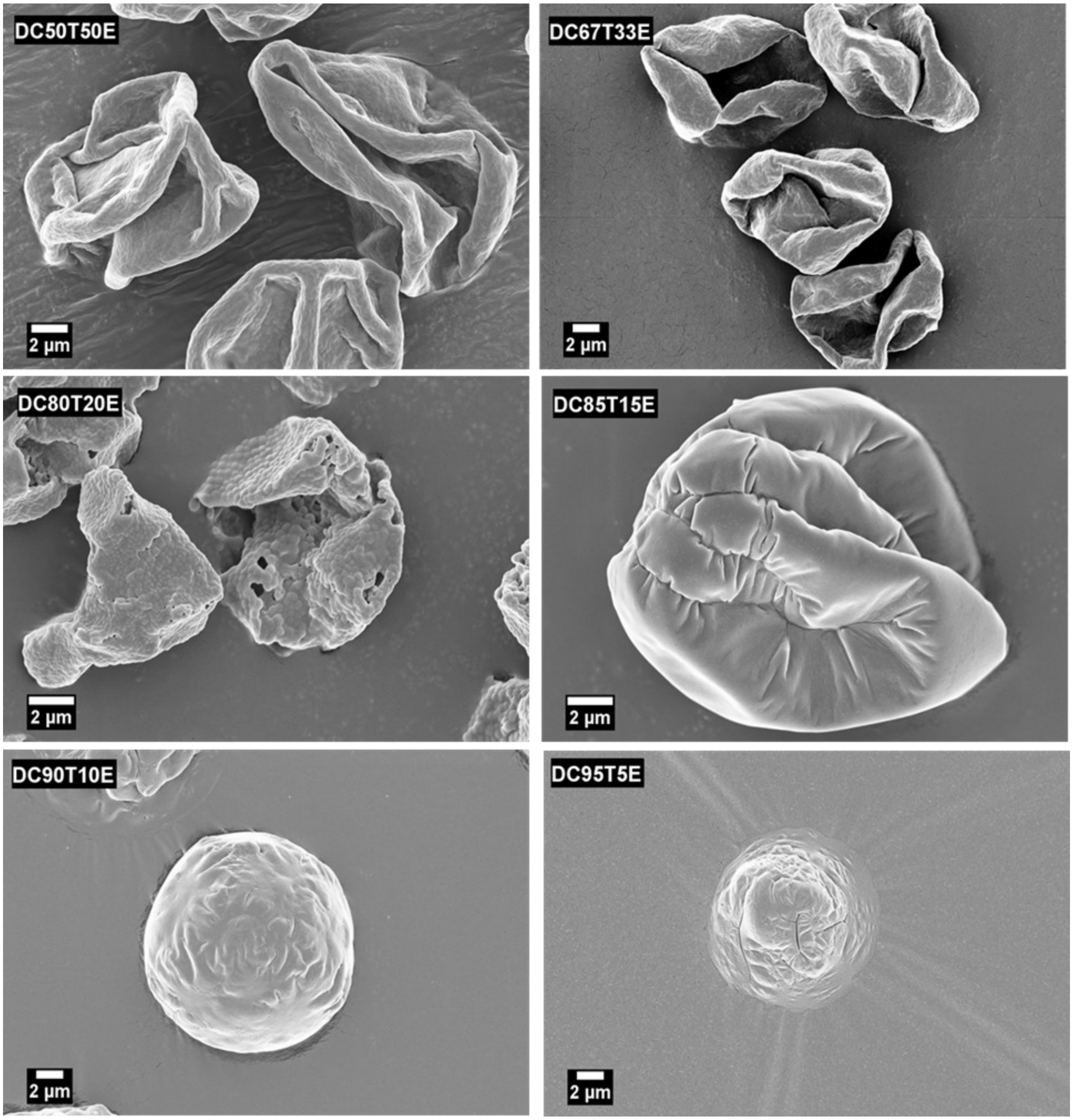

Figure 23: SEM images of particles dried from formulations made with iso-compositional ethanol-water co-solvent, collected from the monodisperse droplet chain at 21 ˚C. Preceding numbers denote the percentage fraction of component dissolved in the solvent with respect to total solids content (10 mg/mL). The images demonstrate that particle morphology is dependent on the ratio of trehalose to Eudragit. Scale bars are shown separately for each image. Notations: DC = Droplet chain, T = trehalose, E = Eudragit.

3.3.2. Particle Formation from Aqueous System

3.3.2.1 Effect of Excipient Mass Fraction on Particle Formation

For biologics that do not tolerate an organic solvent, Eudragit can also be formulated as an aqueous solution at a basic pH, which is neutralized after dissolution of the polymer. For the modeling of the particle formation process in water-based formulations, it was assumed in a first approximation that the Eudragit stays in the neutral solution in a metastable state during drying and that shell formation begins when the true density of the mixture is reached at the surface. For the low drying gas temperature of the droplet chain, the Péclet numbers of both components were lower than in the co-solvent cases, which subsequently resulted in lower surface enrichment, shown in Table 3. The effect of lower surface saturation on the radial distribution of the solids within the particles can be seen in Fig. 9. As expected, shell thickness was higher than for the iso-compositional solvent system at a higher Eudragit content, but it decreased rapidly at lower concentrations. The radial distribution profiles were comparatively flat and, for all cases except the 50:50 ratio of Eudragit and trehalose, the trehalose remained the predominant component on the surface, making the formation of a well-defined Eudragit shell under these conditions unlikely. The particle density values shown in Table 3 are consistent with particles that are fairly dense and spherical, especially at a higher trehalose content.

The morphology of the particles dried from the droplet chain did show some features that were not predicted by the model, as illustrated by the scanning electron microscopy images in Figure 25. Particles with a higher Eudragit content showed considerable folding, thus agreeing with the trends in the model predictions. Particles composed primarily of trehalose are expected to be spherical; however, morphological analysis showed that at lower Eudragit mass fractions the particles were more elongated and cylindrical. Moreover, the magnified images showed the presence of regularly shaped sub-domains on the surface. These are possibly sodium chloride crystals, the byproduct of a neutralization reaction to balancing the pH of the formulation. Crystallization of formulation excipients and alternative precipitation mechanisms like spinodal decomposition (Ordoubadi et al., 2021a) were not considered in the modeling of this case, so it is not surprising that the results provide only the general trends in morphological change with formulation and process conditions.

Table 8 Results of the particle formation modeling for parameters related to shell formation for different Eudragit-trehalose ratios in water-based formulations. Shown are the surface enrichment ($E_{ss,Eud}$), time to reach true density ($t_{t,mix}$) on the surface, normalized by the droplet lifetime, ($t_{t,mix}/\tau_D$); predicted particle density (ρ_P); true density of the excipient mixture ($\rho_{t,mix}$); normalized particle density ($\rho_P/\rho_{t,mix}$); and estimated shell thickness of the particles collected from the monodisperse droplet chain at 21 ˚C. Notations: DC = Droplet chain, T = trehalose, E = Eudragit, (W)= Water. Notations: DC = Droplet Chain, T = trehalose, E = Eudragit. Numbers following the letters represent the percentage mass fraction of the respective solute in the formulation.

Formulation	$\frac{t_{\mathrm{t,mix}}}{\tau_{\mathrm{D}}}$	$E_{ss,Eud}$	ρ_{P} **(kg m^{-3})**	$\rho_{t,\mathrm{mix}}$ **(kg m^{-3})**	$\rho_{\mathrm{P}}/\rho_{\mathrm{t,mix}}$	**Shell Thickness (µm)**
DC50T50E(W)	0.98	1.8	710	1020	0.69	0.80
DC67T33E(W)	0.98	1.79	860	1140	0.75	0.91
DC80T20E(W)	0.98	1.77	1030	1260	0.81	0.50
DC85T15E(W)	0.98	1.75	1120	1320	0.84	0.45
DC90T10E(W)	0.98	1.70	1240	1400	0.89	0.28

DC95T5E(W)	0.99	1.67	1350	1480	0.91	0.13

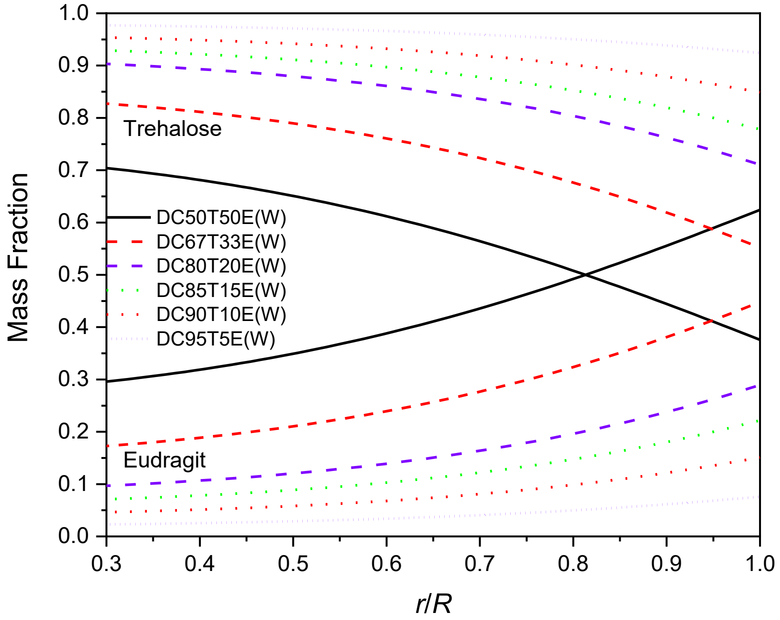

Figure 24: Radial distribution of components within the particles dried from water-based formulations at the point of predicted shell formation. Preceding numbers denote the percentage fraction of component dissolved in the solvent with respect to total solids content (10 mg/mL). A lesser amount of Eudragit reached the surface than in particles dried from ethanol-water mixtures. Notations: DC = Droplet chain, T = trehalose, E = Eudragit.

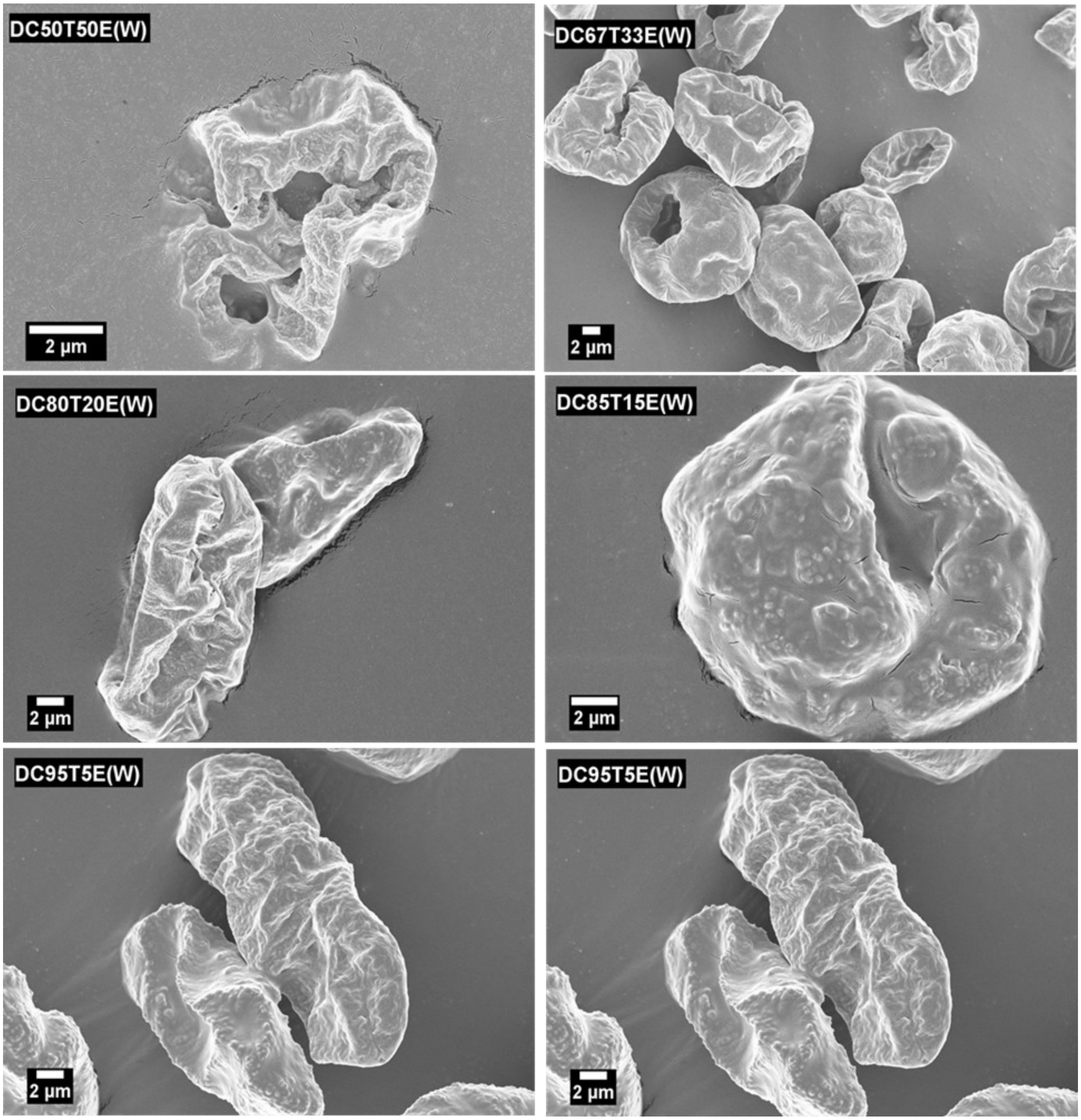

Figure 25: SEM images showing particles dried from water-based formulations produced in a monodisperse droplet chain at 21 ˚C. The particles appeared denser with decreasing Eudragit concentrations. Scale bars are shown separately for each image.

3.3.2.2 Particle Formation at Higher Drying Temperature

To scale up the production of particles for detailed analysis, spray drying of the water-based formulations was conducted at an elevated temperature of 100 ˚C, which reduced the drying time and greatly increased the evaporation rate. As a result, the Péclet numbers and surface enrichment increased. The low density of the particles, normalized by the true density of the mixture at the time of shell formation predicts a core-shell structure and folded morphology for the spray-dried formulations. The shell thickness was calculated for the mean diameter of the dry particles, i.e., 2.2 µm. For these conditions, the shells were predicted to be less than 100 nm thick.

The spray-dried particles showed a morphology consistent with the model predictions and are similar to the particles produced via the monodisperse droplet chain technique, as is evident from the SEM images shown in Figure 26. Due to the higher surface enrichment, low-density particles with a folded shell were formed. Based on their outer morphology, these particles were thought likely to exhibit the targeted core-shell morphology. Hence, they were selected for the dissolution test.

Table 9 Results of the particle formation modeling for parameters related to shell formation for different Eudragit-trehalose ratios in water-based formulations. Shown are the surface enrichment ($E_{ss,Eud}$), predicted particle density (ρ_P), true density of the excipient mixture ($\rho_{t,mix}$), normalized particle density ($\rho_P/\rho_{t,mix}$), and estimated shell thickness of the particles spray-dried at 100 ˚C. Notations: SD = spray-dried, T = trehalose, E = Eudragit. Notations: DC = Droplet Chain, T = trehalose, E = Eudragit. Numbers following the letters represent the percentage mass fraction of the respective solute in the formulation.

Formulation	$E_{ss,Eud}$	ρ_{P} **(kg m^{-3})**	$\rho_{t,\mathrm{mix}}$ **(kg m^{-3})**	$\rho_{\mathrm{P}}/\rho_{\mathrm{t,mix}}$	**Shell Thickness (nm)**

SD80T20E	3.58	315	1160	0.27	94
SD85T15E	3.58	310	1220	0.25	88
SD90T10E	3.58	310	1300	0.24	84
SD95T5E	3.57	310	1420	0.22	81
SD97T3E	3.57	310	1470	0.21	80
SD99T1E	3.57	310	1540	0.20	78

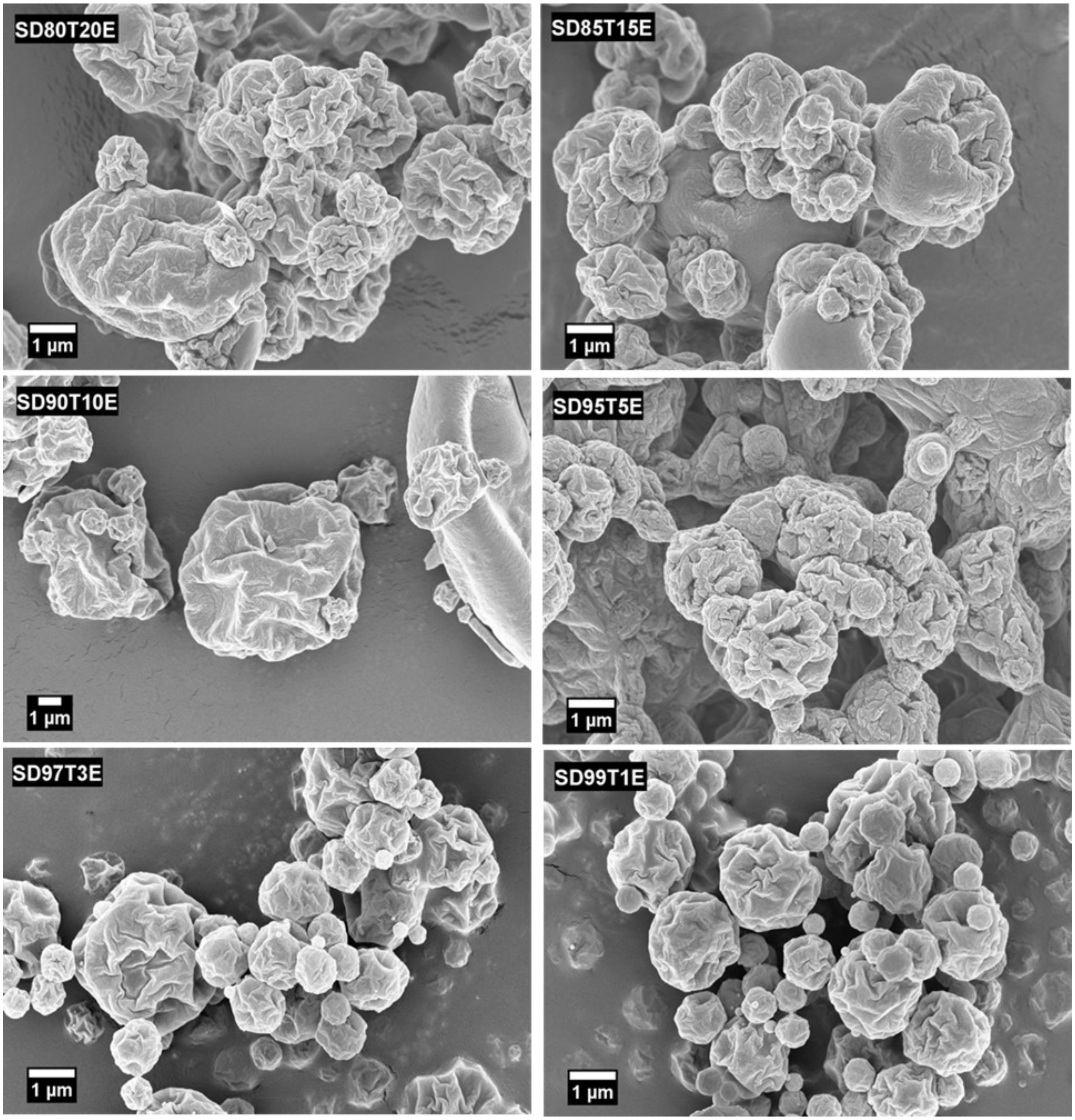

Figure 26: SEM images showing the morphology of the spray-dried particles at 100 ˚C. Preceding numbers denote the percentage fractions of components dissolved in the solvent with respect to total solids content (20 mg/mL). Scale bars are shown separately for each image. Notations: SD = Spray Dried, T = trehalose, E = Eudragit.

3.3.3. Particle Dissolution in Acidic and Alkaline Media

The purpose of conducting the dissolution test was to observe the duration and degree of survival of the particles in simulated gastric conditions. The typical pH of the human stomach ranges from 1.8 to 2.8 (Ovesen et al., 1986), whereas the pH in the intestine can range from 6 to 8 depending on specific regions (small intestine, large intestine, colon) (Evans et al., 1988; Ibekwe et al., 2008). The mean gastric emptying time in humans is 1.1 hours, but this can vary depending on different factors (Lysgård Madsen, 1992). The particles must be able to withstand the corrosive environment of the gastrointestinal tract for an extended period of time in order to successfully deliver a therapeutic to the enteric system.

The dissolution of the spray-dried aqueous formulations suspended in an HCL-water solution (pH = 2) was expressed in terms of the transmission coefficient, as shown in Figure 27. The coefficient ranges from 0 to 1, with 0 indicating no change in light intensity passing through the suspension during the test and 1 indicating total clarification of the suspension, which was interpreted as complete dissolution of the particles in the medium. As a control, Eudragit raw material was first suspended in the medium. The suspension remained unchanged after one hour of mechanical stirring, which was reflected in the relatively constant transmission coefficient. This result was expected because of Eudragit S100's insolubility at low pH values. The spray-dried powders, which were polydisperse with varying morphology and particle sizes, showed different levels of change in the transmission coefficient, depending on the Eudragit content. Particles with the largest Eudragit contents of 10 to 20% maintained a small transmission coefficient over time, indicating that most of the polydisperse particles did not dissolve. By contrast, the formulations containing 1 and 3% Eudragit showed a very sharp rise in the transmission coefficient, consistent with the almost immediate dissolution observed during the test. The case involving 5 % Eudragit showed intermediate behavior with ongoing dissolution over time.

As the Eudragit fraction in the formulations is reduced, the concentration of Eudragit at the surface decreases relative to that of trehalose. For the formulations with low Eudragit content, this makes the shell susceptible to corrosion by hydrochloric acid. However, formulations SD80T20E, SD85T15E and SD90T10E showed promising results for protection against stomach acid, as the change in transmission coefficient was very small over one hour, indicating a relatively small change in suspension concentration in the medium due to corrosion or dissolution.

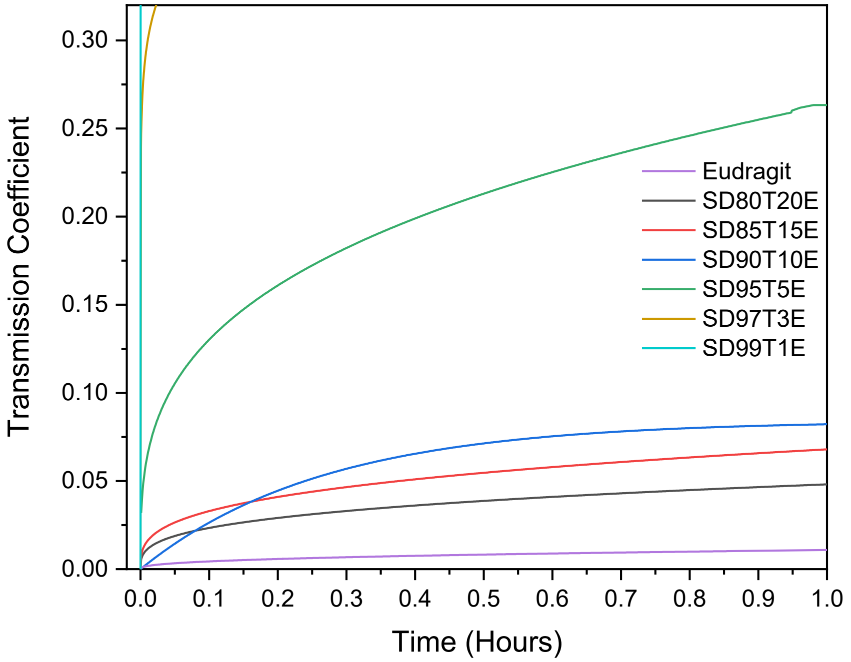

Figure 27: Dissolution behavior as approximated by the optical transmission coefficient for suspensions of different spray-dried powders in an acidic medium (pH 2). Samples with high Eudragit content (SD80T20E, SD85T15E, SD90T10E) showed a very small change in coefficient over time, while SD95T5E dissolved significantly over time, which is reflected in an intermediate value of transmission coefficient. SD97T3E; SD99T1E dissolved almost instantly.

Figure 28 shows the dissolution profiles in an alkaline medium simulating the desired dissolution of the particles in the intestines. During two hours of mechanical stirring, the transmission coefficient increased gradually for all the suspensions. Similarly, formulations with more Eudragit demonstrated a slower dissolution rate. The changes in the transmission coefficients were larger and faster than the results for the acidic medium, indicating a more rapid dissolution of particles in the alkaline medium. These results indicate that Eudragit layers on spray-dried particles can be designed to provide a specific release profile, making this approach promising for enteric delivery.

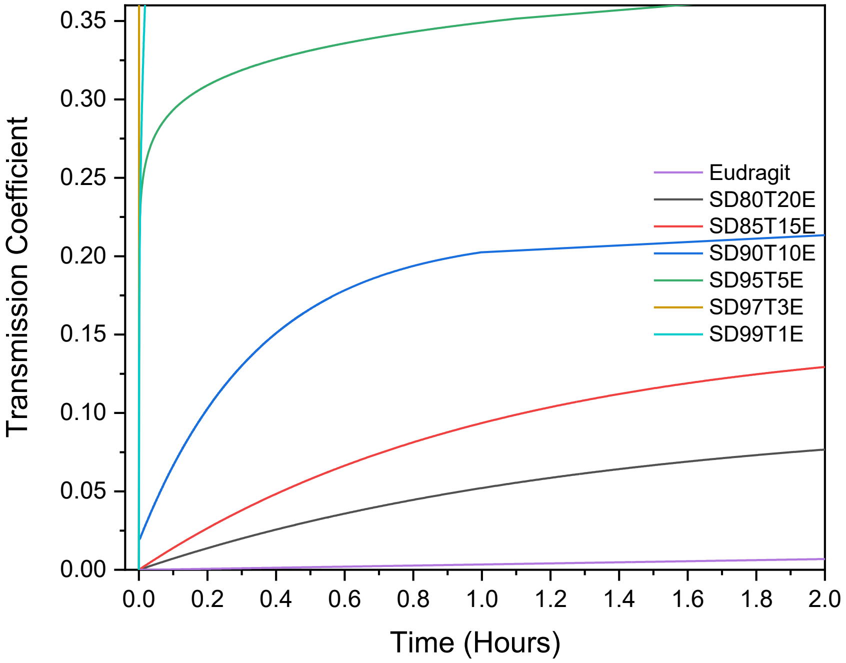

Figure 28: Dissolution behavior as approximated by the optical transmission coefficient for suspensions of different spray-dried powders in an alkaline medium (pH 8). Samples SD80T20E, SD85T15E and SD90T10E showed a gradual increase in transmission intensity over time for two hours, indicating their delayed release pattern. SD95T5E had a relatively higher transmission coefficient, whereas SD97T3E and SD99T1E dissolved in the medium instantly.

3.3.4. Analysis of Particles Subjected to Suspension in Acid

The Raman spectra of the filtered and dried suspensions were analyzed to determine the solid phase of trehalose in the residual powder that remained after the dissolution test in the acidic medium. A failure of the protective shell is expected to lead to water ingress into the trehalose core, which can, in turn, lead to trehalose crystallization or even dissolution. It is important to know if the core is exposed to moisture because a change in the solid phase of trehalose from amorphous to crystalline can inactivate biologics such as bacteriophages (Vandenheuvel et al., 2014). Figure 29 shows the reference spectra for amorphous and crystalline trehalose, and amorphous Eudragit that were used to deconvolute the measured spectra of the four dried suspensions that did not dissolve. The suspension spectra and their deconvoluted residual spectra are shown in Figure 30.

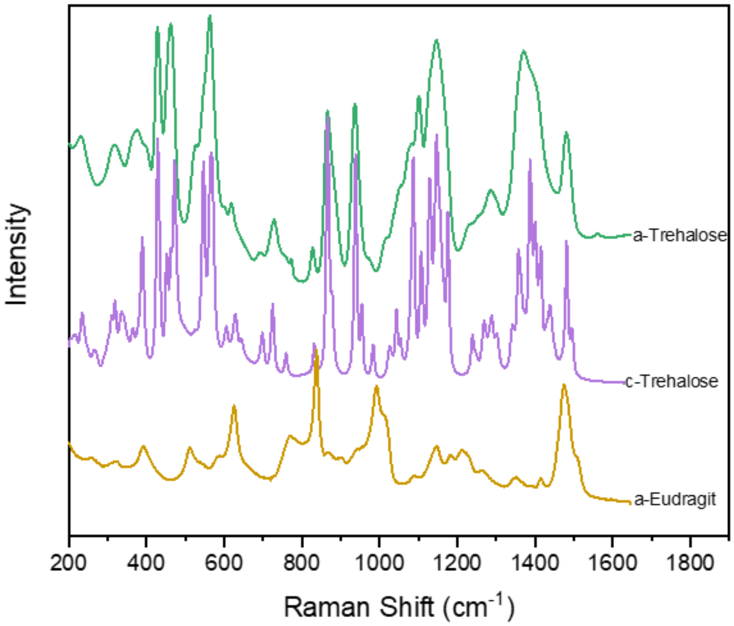

Figure 29: Reference spectra of amorphous and crystalline trehalose and amorphous Eudragit used for deconvolution.

The deconvolution of the Raman spectrum of the recovered suspension SD80T20E showed the trehalose present to be fully amorphous. The 10 and 15% Eudragit-containing formulations had only a small amount of crystalline trehalose. However, the trehalose in the 5% Eudragit formulation had predominantly converted into the crystalline form. The presence of both trehalose and Eudragit in a ratio close to the initial formulation composition in SD80T20E proved that the trehalose core of the particles stayed largely intact even after 1 hour of exposure to acidic conditions. The intensity ratios of crystalline and amorphous trehalose and amorphous Eudragit within the dried suspensions were calculated using a custom-designed dispersive Raman spectroscopy and deconvolution method described elsewhere (Wang et al., 2017a). The results are shown in Table 10. All measurements were triplicated, with the relative standard deviations representing the source of error in the calculations. The measured intensity ratios represent the presence of different components in the formulations and are proportional to the mass fraction ratios of the components, which can be related using calibration factors.

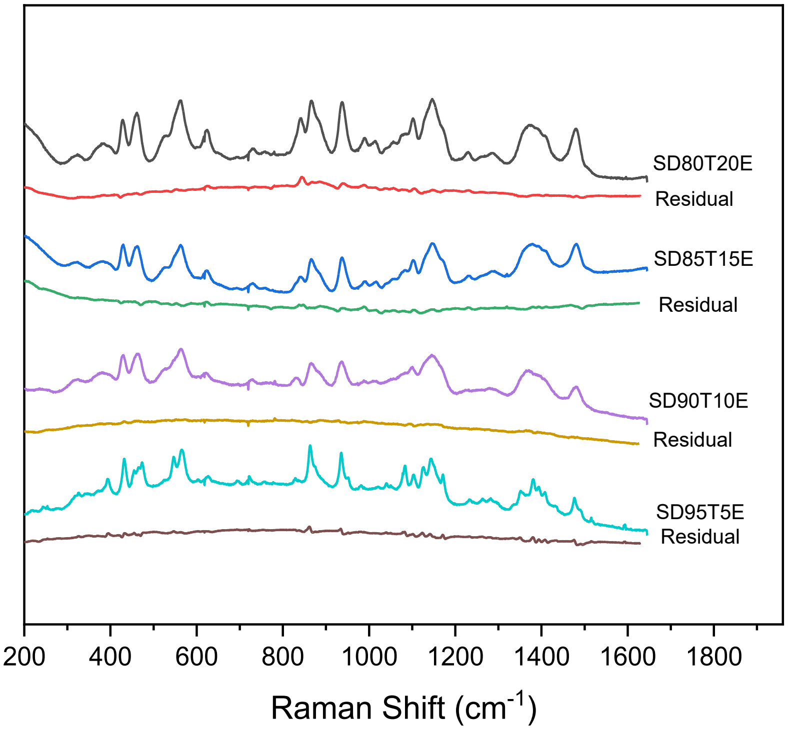

Figure 30: Residual spectra of the cured samples are shown underneath their Raman spectra. A primarily amorphous structure is seen in all samples. Deconvolution of SD85T15E and SD90T10E showed trace amounts of crystalline trehalose, whereas SD95T5E showed the presence of a high amount of crystalline trehalose.

A coating with a thickness on the order of 100 nm (cf. Table 9) in formulation SD80T20E withstood the low pH well enough to keep the core sufficiently protected from water ingress, a result that was confirmed by the absence of crystalline trehalose in the dried suspension. Formulations with lower shell thickness revealed the presence of varying amounts of crystalline trehalose. The intensity factor ratio of crystalline trehalose increases with a decrease in the amount of Eudragit in the formulations, a result that points to an increased presence of the component in the dried suspensions. In the case of formulation SD95T5E, the intensity factor ratio of amorphous trehalose decreased dramatically, whereas the increase in intensity factor ratio of crystalline trehalose was unusually high. This result confirmed that at low Eudragit content, the particle core could not be protected from water ingress after exposure to low pH, making the particles unsuitable for an enteric application.

Table 10 Data showing the intensity factor ratio of amorphous trehalose-amorphous Eudragit ($\frac{I_{a-tre}}{I_{Eud}}$) and crystalline trehalose-amorphous Eudragit ($\frac{I_{c-tre}}{I_{Eud}}$) obtained from deconvolution of the Raman spectra of powder recovered from the acidic medium after one hour of exposure. The relative standard deviation (RSD) represents the error in calculation.

Sample	$\frac{I_{\mathrm{a-tre}}}{I_{\mathrm{Eud}}}$	**RSD (%)**	$\frac{I_{\mathrm{c-tre}}}{I_{\mathrm{Eud}}}$	**RSD (%)**
SD80T20E	1.33	1.2	0	-
SD85T15E	1.67	0.5	0.10	29
SD90T10E	2.33	0.7	0.23	8
SD95T5E	1.33	1.7	0.83	6

3.4. Conclusion

This study describes the application of particle engineering principles in developing microparticles capable of encapsulating biological entities with a pH-responsive polymer via spray drying. The particle formation process of an Eudragit-trehalose system was evaluated at different co-solvent ratios of ethanol-water and in water. The effectiveness of the spray-dried particles against potentially harsh conditions of the gastrointestinal tract was tested by suspending spray-dried particles in solutions simulating gastric conditions and tracking the light transmission intensity through the suspension samples using a new shadowgraphic imaging technique. The results of the preliminary studies showed that irrespective of the type of solvent used, it is possible to manufacture particles with a trehalose core and a Eudragit shell of varying thickness. The results further showed that, as an alternative to subjecting biologics to the stresses of a multi-step tableting process, spray drying can likely simplify the coating process into a single step. The product in powdered form has the potential to provide protection for biologics and can be administered as a suspension, simplifying administration to pediatric and geriatric populations that struggle with swallowing tablets. With appropriate understanding, it appears feasible to design and produce microparticles that can protect biologics such as bacteriophages against harsh gastrointestinal conditions, and the potential demonstrated by the spray-dried powders makes them promising candidates for delivery of biologics to human or animal enteric systems via the oral route.

Because of the limitations of the lab-scale spray dryer used in this study, the particle size of the studied powders was limited to less than 5 µm, smaller than what would be appropriate for oral delivery. Pilot-scale spray driers, however, are capable of producing particles in the range of 50 µm or larger. Spray drying large particle size powders containing phages and *in vitro* stability study of the product at elevated temperature and humidity would be the next logical step in the development of this approach.

Chapter 4. Conclusion and Future Work

Enteric infections such as diarrhoea, cholera, shigella, amoebiasis and campylobacteriosis affect millions of people around the world every year. Although these diseases are prevalent in developing parts of the globe, they are not unknown in developed countries like the USA and Canada, which spend significant sums on the treatment of enteric infections every year. The rise in antibiotic resistance coupled with the slow development of new small-molecule antibiotics calls for research into alternative treatments. Delivering bacteriophages directly to the enteric region has the potential to be an excellent alternative, but challenges arise in finding a way to reduce the processing and mechanical stresses in order to encapsulate the phages with a protective coating capable of surviving the harsh chemical environment of the gastrointestinal tract. Therefore, finding the right low-stress process and proper coating material for the particles is a very important first step. Using the polymer Eudragit to coat a proven biologics stabilizer like trehalose via spray drying can potentially resolve all of the above-mentioned issues.

Prior to mass production, it is important to understand the mechanics of the particle formation process for specific droplet size and drying conditions. The monodisperse droplet chain is a highly useful instrument for this purpose. Chapter 2 discussed the modification and addition of new features to an existing monodisperse droplet chain. Appropriate parts were added to the instrument in order to use interferometric laser imaging for measuring initial droplet diameter. The accuracy and precision of the measurement were remarkably improved, reducing the average error in the calculation to less than 1%. This improvement extended to the measurement of other related properties like evaporation rate, droplet lifetime, Péclet number, etc. Using the initial droplet diameter data, the average density of the particles was calculated. The calculated density was accurate for solid, spherical particles like trehalose, with an error margin of less than 3%. Because of the scarcity of data for average particle density, the density of trehalose-leucine particles, whose sphericity decreases with increasing leucine fraction, was compared to the bulk density of trehalose-leucine powder. Although the density values did not match, the trend in change with increasing leucine fraction in the particles followed the same trajectory. For Eudragit-trehalose microparticles, which had an irregular shape with very low sphericity, calculated particle density was highly dependent on the observed aspect ratio of the particles imaged using scanning electron microscopy. The addition of a custom-designed single-nozzle impactor increased particle collection efficiency to the extent of collecting enough particles for macro-Raman spectroscopy. The measured Raman spectra of the particles collected from the monodisperse droplet chain matched the spectra of the same formulations produced in a spray dryer. The successful integration of the new modifications made the monodisperse droplet chain an effective and powerful tool for the preliminary investigation of the formation properties of inhalable and orally deliverable particles.

Chapter 3 demonstrated the application of the monodisperse droplet chain in investigating the formation process of Eudragit-trehalose microparticles. Due to the solubility properties of Eudragit, formulations of the solids were made in various ethanol-water fractions and in water by shifting its pH to facilitate the dissolution of Eudragit and trehalose. With the help of a numerical particle formation model, microparticle formation for all the solvent compositions was observed. The calculations from the particle formation model showed that irrespective of the solvent used, the particles had a Eudragit shell with a hollow trehalose core, with a shell thickness large enough to provide protection to the core from exposure to moisture. The efficacy of the formed shell was tested by suspending spray-dried particles in solutions simulating the harsh conditions of the gastrointestinal tract and then examining them using a new shadowgraphic imaging technique. The results showed that instead of subjecting the biologics to the stresses of multi-step tableting and coating processes, a single-step process with less mechanical stress like spray drying can be used as an alternative to providing similar or better protection. The powdered product is also a simpler dosage form, which can make administering the drugs to adolescent and geriatric populations much easier. The ability shown by the spray-dried powder to withstand variable pH can be applied to the formulation of deliverables such as bacteriophages in order to protect them in their passage through the gastrointestinal tract, thus making them promising candidates for the delivery of biologics to human or animal enteric systems via the oral route.

Although the upgraded monodisperse droplet chain is an excellent instrument for preliminary investigation, the operating temperature of the instrument is limited to below 100 ˚C in order to prevent the boiling of liquid formulations inside the piezoelectric dispenser. Further improvements can be made to cool the dispenser inside the drying gas flow in order to elevate the drying gas temperature and thereby extend the temperature range. The process of density measurement can be improved by the introduction of the dimensionless empirical shape factor to account for the irregular shape of the particles, the hollow core and the aspect ratio of the particles.

Because of the limitations of the lab-scale spray dryer used in this study, the particle size of the studied powders was limited to less than 5 µm, smaller than what would be appropriate for oral delivery. Pilot-scale spray-driers, however, are capable of producing particles in the range of 50 µm or larger. Spray drying large-particle sized powders containing phages and an *in vitro* stability study of the resulting product at elevated temperature and humidity would be the next logical step in the development of this approach.

References

Abdelsattar, A.S., Abdelrahman, F., Dawoud, A., Connerton, I.F., El-Shibiny, A., 2019. Encapsulation of E. coli phage ZCEC5 in chitosan–alginate beads as a delivery system in phage therapy. AMB Express 9. https://doi.org/10.1186/s13568-019-0810-9

Al-Zoubi, N., AlKhatib, H.S., Bustanji, Y., Aiedeh, K., Malamataris, S., 2008. Sustained-release of buspirone HCl by co spray-drying with aqueous polymeric dispersions. Eur. J. Pharm. Biopharm. 69, 735–742. https://doi.org/10.1016/j.ejpb.2008.01.002

Amiet-Charpentier, C., Gadille, P., Digat, B., Benoit, J.P., 1998. Microencapsulation of rhizobacteria by spray-drying: Formulation and survival studies. J. Microencapsul. 15, 639–659. https://doi.org/10.3109/02652049809008247

Año, G., Esquisabel, A., Pastor, M., Talavera, A., Cedré, B., Fernández, S., Sifontes, S., Aranguren, Y., Falero, G., García, L., Solís, R.L., Pedraz, J.L., 2011. A new oral vaccine candidate based on the microencapsulation by spray-drying of inactivated Vibrio cholerae. Vaccine 29, 5758–5764. https://doi.org/10.1016/j.vaccine.2011.05.098

Ashkenazi, S., Levy, I., Kazaronovski, V., Samra, Z., 2003. Growing antimicrobial resistance of Shigella isolates. J. Antimicrob. Chemother. 51, 427–429. https://doi.org/10.1093/jac/dkg080

Basu, S., Adhiyaman, R., 2008. Preparation and Characterization of Nitrendipine-loaded Eudragit RL 100 Microspheres Prepared by an Emulsion-Solvent Evaporation Method. Trop. J. Pharm. Res. 7, 1033–1041. https://doi.org/10.4314/tjpr.v7i3.14688

Bergman, T.L., Lavine, A.S., Incropera, F.P., DeWitt, D.P., 2011. Fundamentals of heat and mass transfer, 6th ed. Wiley, Hoboken, NJ.

Bora, D., Borude, P., Bhise, K., 2008. Taste masking by spray-drying technique. AAPS PharmSciTech 9, 1159–1164. https://doi.org/10.1208/s12249-008-9154-5

Boraey, M.A., Vehring, R., 2014. Diffusion controlled formation of microparticles. J. Aerosol Sci. 67, 131–143. https://doi.org/10.1016/j.jaerosci.2013.10.002

Carrigy, N.., Vehring, R., 2019. Engineering stable spray-dried biologic powder for inhalation, in: Anthony J. Hickey, Sandro R.P. da Rocha (Eds.), Pharmacuetical Inhalation Aerosol Technology. CRC Press, Boca Raton, pp. 291–326. https://doi.org/https://doi.org/10.1201/9780429055201

Carrigy, N.B., Liang, L., Wang, H., Kariuki, S., Nagel, T.E., Connerton, I.F., Vehring, R., 2020. Trileucine and Pullulan Improve Anti-Campylobacter Bacteriophage Stability in Engineered Spray-Dried Microparticles. Ann. Biomed. Eng. 48, 1169–1180. https://doi.org/10.1007/s10439-019-02435-6

Carrigy, N.B., Ordoubadi, M., Liu, Y., Melhem, O., Barona, D., Wang, H., Milburn, L., Ruzycki, C.A., Finlay, W.H., Vehring, R., 2019. Amorphous pullulan trehalose microparticle platform for respiratory delivery. Int. J. Pharm. 563, 156–168. https://doi.org/10.1016/j.ijpharm.2019.04.004

Cerea, M., Zheng, W., Young, C.R., McGinity, J.W., 2004. A novel powder coating process for attaining taste masking and moisture protective films applied to tablets. Int. J. Pharm. 279, 127–139. https://doi.org/10.1016/j.ijpharm.2004.04.015

Chiu, C.-H., Wu, T.-L., Su, L.-H., Chu, C., Chia, J.-H., Kuo, A.-J., Chien, M.-S., Lin, T.-Y., 2002. The Emergence In Taiwan Of Fluroquinolone Resistance In Salmonella Enterica Serotype Choleraesuis. N. Engl. J. Med. 346. https://doi.org/10.1056/NEJMoa012261.

Collier, S.A., Deng, L., Adam, E.A., Benedict, K.M., Beshearse, E.M., Blackstock, A.J., Bruce, B.B., Derado, G., Edens, C., Fullerton, K.E., Gargano, J.W., Geissler, A.L., Hall, A.J., Havelaar, A.H., Hill, V.R., Hoekstra, R.M., Reddy, S.C., Scallan, E., Stokes, E.K., Yoder, J.S., Beach, M.J., 2021. Estimate of Burden and Direct Healthcare Cost of Infectious Waterborne Diseases in the United States. Emerg. Infect. Dis. 27.

Dai, W., Guo, Y., Zhang, H., Wang, X., Zhang, Q., 2015. Sylysia 350/Eudragit S100 solid nanomatrix as a promising system for oral delivery of cyclosporine A. Int. J. Pharm. 478, 718–725. https://doi.org/10.1016/j.ijpharm.2014.11.030

Das, S., Suresh, P.K., Desmukh, R., 2010. Design of Eudragit RL 100 nanoparticles by nanoprecipitation method for ocular drug delivery. Nanomedicine Nanotechnology, Biol. Med. 6, 318–323. https://doi.org/10.1016/j.nano.2009.09.002

Davis, M., Walker, G., 2018. Recent strategies in spray drying for the enhanced bioavailability of poorly water-soluble drugs. J. Control. Release 269, 110–127. https://doi.org/10.1016/j.jconrel.2017.11.005

De Smet, R., Verschuere, S., Allais, L., Leclercq, G., Dierendonck, M., De Geest, B.G., Van Driessche, I., Demoor, T., Cuvelier, C.A., 2014. Spray-dried polyelectrolyte microparticles in oral antigen delivery: Stability, biocompatibility, and cellular uptake. Biomacromolecules 15, 2301–2309. https://doi.org/10.1021/bm5005367

Deshmukh, R.K., Naik, J.B., 2014. Aceclofenac microspheres: Quality by design approach. Mater. Sci. Eng. C 36, 320–328. https://doi.org/10.1016/j.msec.2013.12.024

Drašković, M., Medarević, D., Aleksić, I., Parojčić, J., 2017. In vitro and in vivo investigation of taste-masking effectiveness of Eudragit E PO as drug particle coating agent in orally disintegrating tablets. Drug Dev. Ind. Pharm. 43, 723–731. https://doi.org/10.1080/03639045.2016.1220572

Edward, J.T., 1970. Molecular Volumes and the Stokes-Einstein Equation. J. Chem. Educ. 47, 261–270. https://doi.org/https://doi.org/10.1021/ed047p261

El-Malah, Y., Nazzal, S., 2008. Novel use of Eudragit® NE 30D/Eudragit® L 30D-55 blends as functional coating materials in time-delayed drug release applications. Int. J. Pharm. 357, 219–227. https://doi.org/10.1016/j.ijpharm.2008.02.003

Esposito, E., Cervellati, F., Menegatti, E., Nastruzzi, C., Cortesi, R., 2002. Spray dried Eudragit microparticles as encapsulation devices for vitamin C. Int. J. Pharm. 242, 329–334. https://doi.org/10.1016/S0378-5173(02)00176-X

Evans, D.F., Pye, G., Bramley, R., Clark, A.G., Dyson, T.J., Hardcastle, J.D., 1988. Measurement of gastrointestinal pH profiles in normal ambulant human subjects. Gut 29, 1035–1041. https://doi.org/10.1136/gut.29.8.1035

Evonik Industries, 2012. Technical Information EUDRAGIT® L 100 and EUDRAGIT® S 100. Evonik Ind. AG 1–7.

Feng, A.L., Boraey, M.A., Gwin, M.A., Finlay, P.R., Kuehl, P.J., Vehring, R., 2011. Mechanistic models facilitate efficient development of leucine containing microparticles for pulmonary drug delivery. Int. J. Pharm. 409, 156–163. https://doi.org/10.1016/j.ijpharm.2011.02.049

Fuchs, N.A., 2013. Evaporation and droplet growth in gaseous media. Elsevier.

Garekani, H.A., Moghaddam, Z.F., Sadeghi, F., 2013. Organic solution versus aqueous dispersion of Eudragit RS in preparation of sustained release microparticles of theophylline using spray drying. Colloids Surfaces B Biointerfaces 108, 374–379. https://doi.org/10.1016/j.colsurfb.2013.03.012

Glantschnig, W.J., Chen, S.-H., 1981. Light scattering from water droplets in the geometrical optics approximation. Appl. Opt. 20, 2499. https://doi.org/10.1364/ao.20.002499

Glass, R.I., Huq, I., Alim a., A.R.M., Yunus, M., 1980. Emergence of multiply antibiotic-resistant Vibrio cholerae in Bangladesh. J. Infect. Dis. 142, 939–942. https://doi.org/10.1093/infdis/142.6.939

Glover, A.R., Skippon, S.M., Boyle, R.D., 1995. Interferometric laser imaging for droplet sizing: a method for droplet-size measurement in sparse spray systems. Appl. Opt. 34, 8409. https://doi.org/10.1364/ao.34.008409

Gomez, M., Ordoubadi, M., McAllister, R.A., Melhem, O., Barona, D., Gracin, S., Ajmera, A., Lechuga-Ballesteros, D., H., W.F., Vehring, R., 2018. Monodisperse Droplet Chain Technique to Support Development of Co-solvent Based Inhalation Products Mellissa, in: Dalby, R.N., Byron, P.R., Hindle, M., Peart, J., Traini, D., Youn, P.M., Farr, S.J., Suman, J.D., Watts, A. (Eds.), Respiratory Drug Delivery. Respiratory Drug Delivery (2018), Tuscon, pp. 563–568.

Grasmeijer, N., Frijlink, H.W., Hinrichs, W.L.J., 2016. Model to predict inhomogeneous protein–sugar distribution in powders prepared by spray drying. J. Aerosol Sci. 101, 22–33. https://doi.org/10.1016/j.jaerosci.2016.07.012

Hardalupas, Y., Sahu, S., Taylor, A.M.K.P., Zarogoulidis, K., 2010. Simultaneous planar measurement of droplet velocity and size with gas phase velocities in a spray by combined ILIDS and PIV techniques. Exp. Fluids 49, 417–434. https://doi.org/10.1007/s00348-009-0802-7

Hesselbacher, K.H., Anders, K., Frohn, A., 1991. Experimental investigation of

Gaussian beam effects on the accuracy of a droplet sizing method. Appl. Opt. 30, 4930. https://doi.org/10.1364/ao.30.004930

Hoe, S., Ivey, J.W., Boraey, M.A., Shamsaddini-Shahrbabak, A., Javaheri, E., Matinkhoo, S., Finlay, W.H., Vehring, R., 2014. Use of a fundamental approach to spray-drying formulation design to facilitate the development of multi-component dry powder aerosols for respiratory drug delivery. Pharm. Res. 31, 449–465. https://doi.org/10.1007/s11095-013-1174-5

Ibekwe, V.C., Fadda, H.M., McConnell, E.L., Khela, M.K., Evans, D.F., Basit, A.W., 2008. Interplay between intestinal pH, transit time and feed status on the in vivo performance of pH responsive ileo-colonic release systems. Pharm. Res. 25, 1828–1835. https://doi.org/10.1007/s11095-008-9580-9

Ivey, J., Bhambri, P., Lewis, D., Church, T., Finlay, W., Vehring, R., 2016. Dried corticosteroid particle formation from evaporating monodisperse propellant solution droplets, in: AAPS Annual Meeting and Exposition. Denver.

Ivey, J.W., Vehring, R., 2010. The use of modeling in spray drying of emulsions and suspensions accelerates formulations and process development. Comput. Chem. Eng. 34, 1036–1040. https://doi.org/https://doi.org/10.1016/j.compchemeng.2010.02.031

Jain, N.K., Roy, I., 2010. Trehalose and protein stability. Curr. Protoc. Protein Sci. 1–12. https://doi.org/10.1002/0471140864.ps0409s59

Jończyk, E., Kłak, M., Międzybrodzki, R., Górski, A., 2011. The influence of external factors on bacteriophages-review. Folia Microbiol. (Praha). 56, 191–200. https://doi.org/10.1007/s12223-011-0039-8

Kalume, A., Gong, Z., Wang, C., Santarpia, J., Pan, Y. Le, 2018. Detection and characterization of chemical and biological aerosols using laser-trapping single-particle Raman spectroscopy. WIT Trans. Ecol. Environ. 230, 323–329. https://doi.org/10.2495/AIR180301

Kim, Y.D., Morr, C. V., Schenz, T.W., 1996. Microencapsulation Properties of Gum Arabic and Several Food Proteins: Liquid Orange Oil Emulsion Particles. J. Agric. Food Chem. 44, 1308–1313. https://doi.org/10.1021/jf950391e

König, G., Anders, K., Frohn, A., 1986. A new light-scattering technique to measure the diameter of periodically generated moving droplets. J. Aerosol Sci. 17, 157–167. https://doi.org/10.1016/0021-8502(86)90063-7

Koo, J., DePaola, A., Marshall, D.L., 2000. Effect of simulated gastric fluid and bile on survival of Vibrio vulnificus and Vibrio vulnificus phage†. J. Food Prot. 63, 1665–1669. https://doi.org/10.4315/0362-028X-63.12.1665

Koo, J., Marshall, D.L., DePaola, A., 2001. Antacid Increases Survival of Vibrio vulnificus and Vibrio vulnificus Phage in a Gastrointestinal Model. Appl. Environ. Microbiol. 67, 2895–2902. https://doi.org/10.1128/AEM.67.7.2895-2902.2001

Kristmundsdóttir, T., Gudmundsson, Ó.S., Ingvarsdóttir, K., 1996. Release of diltiazem from Eudragit microparticles prepared by spray-drying. Int. J. Pharm. 137, 159–165. https://doi.org/10.1016/0378-5173(96)04509-7

Kunda, N.K., Alfagih, I.M., Miyaji, E.N., Figueiredo, D.B., Gonçalves, V.M., Ferreira, D.M., Dennison, S.R., Somavarapu, S., Hutcheon, G.A., Saleem, I.Y., 2015. Pulmonary dry powder vaccine of pneumococcal antigen loaded nanoparticles. Int. J. Pharm. 495, 903–912. https://doi.org/10.1016/j.ijpharm.2015.09.034

LeClair, D.A., Cranston, E.D., Xing, Z., Thompson, M.R., 2016. Optimization of Spray Drying Conditions for Yield, Particle Size and Biological Activity of Thermally Stable Viral Vectors. Pharm. Res. 33, 2763–2776. https://doi.org/10.1007/s11095-016-2003-4

Lee, J.H., Park, T.G., Choi, H.K., 2000. Effect of formulation and processing variables on the characteristics of microspheres for water-soluble drugs prepared by w/o/o double emulsion solvent diffusion method. Int. J. Pharm. 196, 75–83. https://doi.org/10.1016/S0378-5173(99)00440-8

Leung, S.S.Y., Parumasivam, T., Gao, F.G., Nicholas B. Carrigy, Vehring, R., Finlay, W.H., Morales, S., Britton, W.J., Kutter, E., Chan, H.-K., 2018a. Effects of storage conditions on the stability of spray dried, inhalable bacteriophage powders. Physiol. Behav. 176, 139–148. https://doi.org/10.1016/j.ijpharm.2017.01.060.Effects

Leung, S.S.Y., Parumasivam, T., Nguyen, A., Gengenbach, T., Carter, E.A., Carrigy, N.B., Wang, H., Vehring, R., Finlay, W.H., Morales, S., Britton, W.J., Kutter, E., Chan, H.K., 2018b. Effect of storage temperature on the stability of spray dried bacteriophage powders. Eur. J. Pharm. Biopharm. 127, 213–222. https://doi.org/10.1016/j.ejpb.2018.02.033

Li, L., Sun, S., Parumasivam, T., Denman, J.A., Gengenbach, T., Tang, P., Mao, S., Chan, H.K., 2016. L-Leucine as an excipient against moisture on in vitro aerosolization performances of highly hygroscopic spray-dried powders. Eur. J. Pharm. Biopharm. 102, 132–141. https://doi.org/10.1016/j.ejpb.2016.02.010

Lins, R.D., Pereira, C.S., Hünenberger, P.H., 2004. Trehalose-Protein Interaction in Aqueous Solution. Proteins Struct. Funct. Genet. 55, 177–186. https://doi.org/10.1002/prot.10632

Lock, J.A., Jamison, J.M., Lin, C.-Y., 1994. Rainbow scattering by a coated sphere. Appl. Opt. 33, 4677. https://doi.org/10.1364/ao.33.004677

López-Díez, E.C., Bone, S., 2004. The interaction of trypsin with trehalose: An investigation of protein preservation mechanisms. Biochim. Biophys. Acta - Gen. Subj. 1673, 139–148. https://doi.org/10.1016/j.bbagen.2004.04.010

Lunter, D.J., Daniels, R., 2012. New film forming emulsions containing Eudragit® NE and/or RS 30D for sustained dermal delivery of nonivamide. Eur. J. Pharm. Biopharm. 82, 291–298. https://doi.org/10.1016/j.ejpb.2012.06.010

Lysgård Madsen, J., 1992. Effects of gender, age, and body mass index on gastrointestinal transit times. Dig. Dis. Sci. 37, 1548–1553. https://doi.org/10.1007/BF01296501

Matinkhoo, S., Lynch, K.H., Dennis, J.J., Finlay, W.H., Vehring, R., 2011. Spray-Dried Respirable Powders Containing Bacteriophages for the Treatment of Pulmonary Infections. J. Pharm. Sci. 100, 5197–5205. https://doi.org/https://doi.org/10.1002/jps.22715

Mwansa, J.C.L., Mwaba, J., Lukwesa, C., Bhuiyan, N.A., Ansaruzzaman, M., Ramamurthy, T., Alam, M., Balakrish, G., 2007. Multiply antibiotic-resistant Vibrio cholerae O1 biotype El Tor strains emerge during cholera outbreaks in Zambia. Epidemiol. Infect. 135, 847–853. https://doi.org/10.1017/S0950268806007254

Nussenzveig, H.M., 1979. Complex angular momentum theory of the rainbow and the glory. J. Opt. Soc. Am. 69, 1068. https://doi.org/10.1364/josa.69.001068

Ordoubadi, M., Gregson, F.K.A., Melhem, O., Barona, D., Miles, R.E.H., D'Sa, D., Gracin, S., Lechuga-Ballesteros, D., Reid, J.P., Finlay, W.H., Vehring, R., 2019. Multi-Solvent Microdroplet Evaporation: Modeling and Measurement of Spray-Drying Kinetics with Inhalable Pharmaceutics. Pharm. Res. 36. https://doi.org/10.1007/s11095-019-2630-7

Ordoubadi, M., Gregson, F.K.A., Wang, H., Carrigy, N.B., Nicholas, M., Gracin, S., Lechuga-, Lechuga-Ballesteros, D., Reid, J.P., Finlay, W.H., Vehring, R., 2021a. Trileucine as a dispersibility enhancer of spray-dried inhalable microparticles. J. Control. Release. https://doi.org/https://doi.org/10.1016/j.jconrel.2021.06.045

Ordoubadi, M., Gregson, F.K.A., Wang, H., Nicholas, M., Gracin, S., Lechuga-Ballesteros, D., Reid, J.P., Finlay, W.H., Vehring, R., 2021b. On the particle formation of leucine in spray drying of inhalable microparticles. Int. J. Pharm. 592, 120102. https://doi.org/10.1016/j.ijpharm.2020.120102

Ovesen, L., Bendtsen, F., Tage-Jensen, U., Pedersen, N.T., Gram, B.R., Rune, S.J., 1986. Intraluminal pH in the stomach, duodenum, and proximal jejunum in normal subjects and patients with exocrine pancreatic insufficiency. Gastroenterology 90, 958–962. https://doi.org/10.1016/0016-5085(86)90873-5

Pearnchob, N., Bodmeier, R., 2003. Dry polymer powder coating and comparison with conventional liquid-based coatings for Eudragit® RS, ethylcellulose and shellac. Eur. J. Pharm. Biopharm. 56, 363–369. https://doi.org/10.1016/S0939-6411(03)00121-8

Perumal, D., 2001. Microencapsulation of ibuprofen and Eudragit RS 100 by the emulsion solvent evaporation technique 218, 1–11. https://doi.org/10.1016/s0378-5173(00)00686-4

Pradhan, R., Kim, S.Y., Yong, C.S., Kim, J.O., 2016. Preparation and characterization of spray-dried valsartan-loaded Eudragit® E PO solid dispersion microparticles. Asian J. Pharm. Sci. 11, 744–750. https://doi.org/10.1016/j.ajps.2016.05.002

Qiao, M., Luo, Y., Zhang, L., Ma, Y., Stephenson, T.S., Zhu, J., 2010a. Sustained release coating of tablets with Eudragit® RS/RL using a novel electrostatic dry powder coating process. Int. J. Pharm. 399, 37–43. https://doi.org/10.1016/j.ijpharm.2010.07.047

Qiao, M., Zhang, L., Ma, Y., Zhu, J., Chow, K., 2010b. A novel electrostatic dry powder coating process for pharmaceutical dosage forms: Immediate release coatings for tablets. Eur. J. Pharm. Biopharm. 76, 304–310. https://doi.org/10.1016/j.ejpb.2010.06.009

Rassu, G., Gavini, E., Spada, G., Giunchedi, P., Marceddu, S., 2008. Ketoprofen spray-dried microspheres based on eudragit® RS and RL: Study of the manufacturing parameters. Drug Dev. Ind. Pharm. 34, 1178–1187. https://doi.org/10.1080/03639040801974303

Reinthaler, F.F., Posch, J., Feierl, G., Wüst, G., Haas, D., Ruckenbauer, G., Mascher, F., Marth, E., 2003. Antibiotic resistance of E. Coli in sewage and sludge. Water Res. 37, 1685–1690. https://doi.org/10.1016/S0043-1354(02)00569-9

Rowe, R.C., Sheskey, P.J., Quinn, M.E., 2009. Handbook of pharmaceutical excipients, Libros Digitales-Pharmaceutical Press.

Saboo, S., Tumban, E., Peabody, J., Wafula, D., Peabody, D.S., Chackerian, B., Muttil, P., 2016. Optimized Formulation of a Thermostable Spray-Dried Virus-Like Particle Vaccine against Human Papillomavirus. Mol. Pharm. 13, 1646–1655. https://doi.org/10.1021/acs.molpharmaceut.6b00072

Sahoo, S.K., Mallick, A.A., Barik, B.B., Senapati, P.C., 2005. Microspheres of Stavudine 4, 369–375.

Sauer, D., Cerea, M., Dinunzio, J., McGinity, J., 2013. Dry powder coating of pharmaceuticals: A review. Int. J. Pharm. 457, 488–502. https://doi.org/10.1016/j.ijpharm.2013.02.032

Sauer, D., McGinity, J., 2009. Properties of theophylline tablets dry powder coated with Eudragit ® e PO and Eudragit® L 100-55. Pharm. Dev. Technol. 14, 632–641. https://doi.org/10.3109/10837450902882369

Schneider, C.A., Rasband, W.S., Eliceiri, K.W., 2012. NIH Image to ImageJ: 25 years of image analysis. Nat. Methods 9, 671–675. https://doi.org/10.1038/nmeth.2089

Schuck, P., 2002. Spray drying of dairy products: state of the art. Lait 82, 375–382.

https://doi.org/10.1051/lait

Shamsaddini-shahrbabak, A., Vehring, R., 2008. The Compression Behavior of Respirable Powders at Different Relative Humidity Measured by a Compressed Bulk Density Tester for Small Sample Masses. Rdd2012 777–780.

Skippon, S.M., Tagaki, Y., 1996. ILIDS measurements of the evaporation of fuel droplets during the intake and compression strokes in a firing lean burn engine. SAE Tech. Pap. 105, 1111–1126. https://doi.org/10.4271/960830

Slimani, F., Grehan, G., Gouesbet, G., Allano, D., 1984. Near-Field Lorenz-Mie Theory and Its Application To Microholography. Appl. Opt. 23, 4140–4148. https://doi.org/10.1364/AO.23.004140

Sóti, P.L., Bocz, K., Pataki, H., Eke, Z., Farkas, A., Verreck, G., Kiss, É., Fekete, P., Vigh, T., Wagner, I., Nagy, Z.K., Marosi, G., 2015. Comparison of spray drying, electroblowing and electrospinning for preparation of Eudragit E and itraconazole solid dispersions. Int. J. Pharm. 494, 23–30. https://doi.org/10.1016/j.ijpharm.2015.07.076

Sou, T., Morton, D.A.V., Williamson, M., Meeusen, E.N., Kaminskas, L.M., McIntosh, M.P., 2015. Spray-Dried Influenza Antigen with Trehalose and Leucine Produces an Aerosolizable Powder Vaccine Formulation that Induces Strong Systemic and Mucosal Immunity after Pulmonary Administration. J. Aerosol Med. Pulm. Drug Deliv. 28, 361–371. https://doi.org/10.1089/jamp.2014.1176

Thaker, S.M., Mahanwar, P.A., Patil, V. V., Thorat, B.N., 2010. Synthesis and spray drying of water-redispersible polymer. Dry. Technol. 28, 669–676. https://doi.org/10.1080/07373931003799152

Thakral, S., Thakral, N.K., Majumdar, D.K., 2013. Eudragit®: A technology evaluation. Expert Opin. Drug Deliv. 10, 131–149. https://doi.org/10.1517/17425247.2013.736962

Troeger, C., Blacker, B.F., Khalil, I.A., Rao, P.C., Cao, S., Zimsen, S.R., Albertson, S.B., Stanaway, J.D., Deshpande, A., Abebe, Z., Alvis-Guzman, N., Amare, A.T., Asgedom, S.W., Anteneh, Z.A., Antonio, C.A.T., Aremu, O., Asfaw, E.T., Atey, T.M., Atique, S., Avokpaho, E.F.G.A., Awasthi, A., Ayele, H.T., Barac, A., Barreto, M.L., Bassat, Q., Belay, S.A., Bensenor, I.M., Bhutta, Z.A., Bijani, A., Bizuneh, H., Castañeda-Orjuela, C.A., Dadi, A.F., Dandona, L., Dandona, R., Do, H.P., Dubey, M., Dubljanin, E., Edessa, D., Endries, A.Y., Eshrati, B., Farag, T., Feyissa, G.T., Foreman, K.J., Forouzanfar, M.H., Fullman, N., Gething, P.W., Gishu, M.D., Godwin, W.W., Gugnani, H.C., Gupta, R., Hailu, G.B., Hassen, H.Y., Hibstu, D.T., Ilesanmi, O.S., Jonas, J.B., Kahsay, A., Kang, G., Kasaeian, A., Khader, Y.S., Khan, E.A., Khan, M.A., Khang, Y.H., Kissoon, N., Kochhar, S., Kotloff, K.L., Koyanagi, A., Kumar, G.A., Magdy Abd El Razek, H., Malekzadeh, R., Malta, D.C., Mehata, S., Mendoza, W., Mengistu, D.T., Menota, B.G., Mezgebe, H.B., Mlashu, F.W., Murthy, S., Naik, G.A., Nguyen, C.T., Nguyen, T.H., Ningrum, D.N.A., Ogbo, F.A., Olagunju, A.T., Paudel, D., Platts-Mills, J.A., Qorbani, M., Rafay, A., Rai, R.K., Rana, S.M., Ranabhat, C.L., Rasella, D., Ray, S.E., Reis, C., Renzaho, A.M., Rezai, M.S., Ruhago, G.M., Safiri, S., Salomon, J.A., Sanabria, J.R., Sartorius, B., Sawhney, M., Sepanlou, S.G., Shigematsu, M., Sisay, M., Somayaji, R., Sreeramareddy, C.T., Sykes, B.L., Taffere, G.R., Topor-Madry, R., Tran, B.X., Tuem, K.B., Ukwaja, K.N., Vollset, S.E., Walson, J.L., Weaver, M.R., Weldegwergs, K.G., Werdecker, A., Workicho, A., Yenesew, M., Yirsaw, B.D., Yonemoto, N., El Sayed Zaki, M., Vos, T., Lim, S.S., Naghavi, M., Murray, C.J., Mokdad, A.H., Hay, S.I., Reiner, R.C., 2018. Estimates of the global, regional, and national morbidity, mortality, and aetiologies of diarrhoea in 195 countries: a systematic analysis for the Global Burden of Disease Study 2016. Lancet Infect. Dis. 18, 1211–1228. https://doi.org/10.1016/S1473-3099(18)30362-1

Trung, V.N., Phung, V. Le, Chinh, H. Le, Weintraub, A., 2005. Antibiotic resistance in diarrheagenic Escherichia coli and Shigella strains isolated from children in Hanoi, Vietnam. Antimicrob. Agents Chemother. 49, 816–819. https://doi.org/10.1128/AAC.49.2.816-819.2005

van den Bogaard, A.E., London, N., Driessen, C., Stobberingh, E.E., 2001. Antibiotic resistance of faecal Escherichia coli in poultry, poultry farmers and poultry slaughterers. J. Antimicrob. Chemother. 47, 763–771. https://doi.org/10.1093/jac/47.6.763

Vandenheuvel, D., Meeus, J., Lavigne, R., Van Den Mooter, G., 2014. Instability of bacteriophages in spray-dried trehalose powders is caused by crystallization of the matrix. Int. J. Pharm. 472, 202–205. https://doi.org/10.1016/j.ijpharm.2014.06.026

Vehring, R., 2008. Pharmaceutical particle engineering via spray drying. Pharm. Res. 25, 999–1022. https://doi.org/10.1007/s11095-007-9475-1

Vehring, R., 2005. Red-excitation dispersive Raman spectroscopy is a suitable technique for solid-state analysis of respirable pharmaceutical powders. Appl. Spectrosc. 59, 286–292. https://doi.org/10.1366/0003702053585318

Vehring, R., Foss, W.R., Lechuga-Ballesteros, D., 2007. Particle formation in spray drying. J. Aerosol Sci. 38, 728–746. https://doi.org/10.1016/j.jaerosci.2007.04.005

Vinner, G.K., Rezaie-Yazdi, Z., Leppanen, M., Stapley, A.G.F., Leaper, M.C., Malik, D.J., 2019. Microencapsulation of Salmonella-specific bacteriophage felix o1 using spray-drying in a ph-responsive formulation and direct compression tableting of powders into a solid oral dosage form. Pharmaceuticals 12, 1–14. https://doi.org/10.3390/ph12010043

Walz, M., Hirth, T., Weber, A., 2018. Investigation of chemically modified inulin as encapsulation material for pharmaceutical substances by spray-drying. Colloids Surfaces A Physicochem. Eng. Asp. 536, 47–52. https://doi.org/10.1016/j.colsurfa.2017.07.072

Wang, C.C., Zhang, G., Shah, N.H., Infeld, M.H., Malick, A.W., McGinity, J.W., 1997. Influence of plasticizers on the mechanical properties of pellets containing eudragit® RS 30 d. Int. J. Pharm. 152, 153–163. https://doi.org/10.1016/S0378-5173(97)00080-X

Wang, H., Barona, D., Oladepo, S., Williams, L., Hoe, S., Lechuga-Ballesteros, D., Vehring, R., 2017a. Macro-Raman spectroscopy for bulk composition and homogeneity analysis of multi-component pharmaceutical powders. J. Pharm. Biomed. Anal. 141, 180–191. https://doi.org/10.1016/j.jpba.2017.04.003

Wang, H., Bhambri, P., Ivey, J., Vehring, R., 2017b. Design and pharmaceutical applications of a low-flow-rate single-nozzle impactor. Int. J. Pharm. 533, 14–25. https://doi.org/10.1016/j.ijpharm.2017.09.047

Wang, H., Tan, P., Barona, D., Li, G., Hoe, S., Lechuga-Ballesteros, D., Nobes, D.S., Vehring, R., 2018. Characterization of the suspension stability of pharmaceuticals using a shadowgraphic imaging method. Int. J. Pharm. 548, 128–138. https://doi.org/10.1016/j.ijpharm.2018.06.053

WHO, UNICEF, 2019. Progress on household drinking water, sanitation and hygiene 2000-2017 Special focus on inequalities, Progress on Drinking Water , Sanitation and Hygiene.

World Health Organization, 2014. Antimicrobial resistance: global report on surveillance.

Yoke-Kqueen, C., Learn-Han, L., Noorzaleha, A.S., Son, R., Sabrina, S., Jiun-Horng, S., Chai-Hoon, K., 2008. Characterization of multiple-antimicrobial-resistant Salmonella enterica Subsp. enterica isolated from indigenous vegetables and poultry in Malaysia. Lett. Appl. Microbiol. 46, 318–324. https://doi.org/10.1111/j.1472-765X.2007.02311.x

Appendix A: Supplemental Data from Modifications to the Monodisperse Droplet Chain

A.1. Hardware Used for Modification of the Monodisperse Droplet Chain

Table A 1: List of components used for making necessary modifications to the monodisperse droplet chain.

No.	Manufacturer	Item	Quantity
1	Process Instruments,	Diode Laser	1
2	Thorlabs Inc	Iris diaphragm	2
3		Plano-convex lens	2
4		Fixed optic mount	4
5		Lens tube	2
6		Plano mirrors	2
7		Mirror mount	1
8		Optical posts	8
9		Mounting base (for laser)	1
10		Strobe light	1
11	Glass Shop, Department of Chemistry, UofA	Borosilicate Glass Tube	1
12	JAI	High-speed camera	1
13	Nikon	High-aperture lens	1
14	Velmax Inc.	Motorized stage	1
15	Microfab Technologies Inc	Piezoelectric dispenser	2
16	Microdrop Technologies GmbH	Electric controller	1

A.2. Processing Interference Fringes Using MATLAB GUI

The captured images of the interference patterns were processed using a custom-built MATLAB Graphic User Interface (GUI). The GUI is capable of adjusting the brightness and contrast of the images manually or automatically to increase the intensity of the fringes for easier processing.

The interface has the following panels and buttons.

Windows 1 and 2: Show the raw file and file after processing, respectively.

Load: Clicking the button allows the user to select a directory and upload any .jpg, .jpeg, or .tiff file to the interface.

Auto Balance: Automatically balances the brightness and contrast of the uploaded image and shows the converted image in a second window. Clicking the button opens the default MATLAB function “Imadjust”, which maps the intensity values in the grayscale image to the new values in the output image. By default, Imadjust saturates the bottom 1% and the top 1% of all pixel values.

Brightness: The slider can be used to change the brightness of the image manually

Contrast: Clicking this button opens the “Adjust Contrast“ dialogue box. The box shows the histogram of the greyscale image, which can be adjusted manually as needed.

After the brightness and the contrast have been adjusted, the intensity map across the image is created by using the MATLAB default function “Improfile”. Improfile retrieves the intensity values of pixels along a line or a multiline path in the grayscale, binary, or RGB image in the current axes and displays a plot of the intensity values. If the specified path consists of a single line segment, Improfile creates a two-dimensional plot of the phase function in terms of intensity value versus the distance along the line segment.

Rectangle: Allows the user to draw a rectangle around the region of interest.

Coordinates: A crosshair appears upon clicking the button. The two-dimensional Cartesian coordinate of any part of the processed image can be visualized.

Convert: Allows the user to translate the data from the plot of the phase function into a .mat file.

Curve Fitting: Opens the phase function in the Curve Fitting Tool of MATLAB. The generated phase function curves usually exhibit residual noise from the surroundings. Using predefined functions, the curves can be smoothed. The Smoothing Spline function was used in this case. The average distance between the consecutive maxima can be calculated in terms of pixels, and is later used to determine the angular fringe spacing.

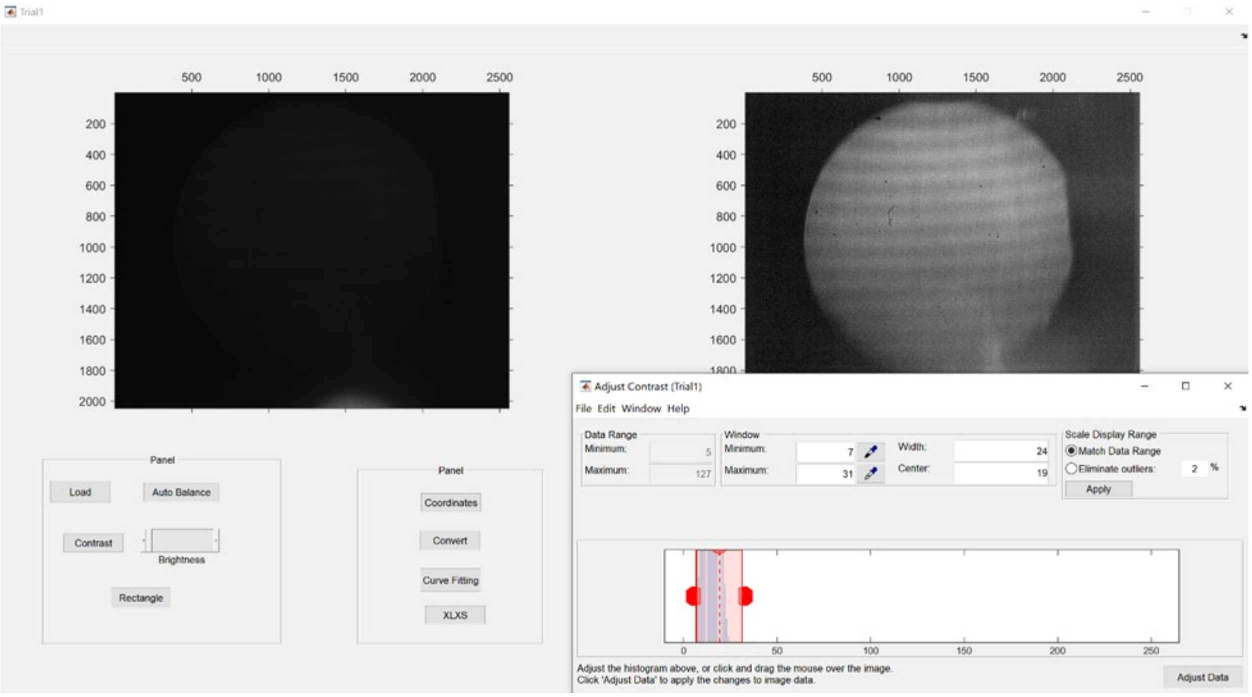

Data Range: Minimum: 5; Maximum: 127

Window: Minimum: 7; Maximum: 31; Width: 24; Center: 19

● Match Data Range

○ Eliminate outliers: 2 %

Adjust the histogram above, or click and drag the mouse over the image.
Click 'Adjust Data' to apply the changes to image data.

Figure A.1.: MATLAB Graphic User Interface (GUI) for processing images of interference fringes. The figure shows a raw image alongside a processed image. The "Adjust" control pane at the bottom right corner appears on clicking the "Contrast" button, and image contrast can be adjusted manually.

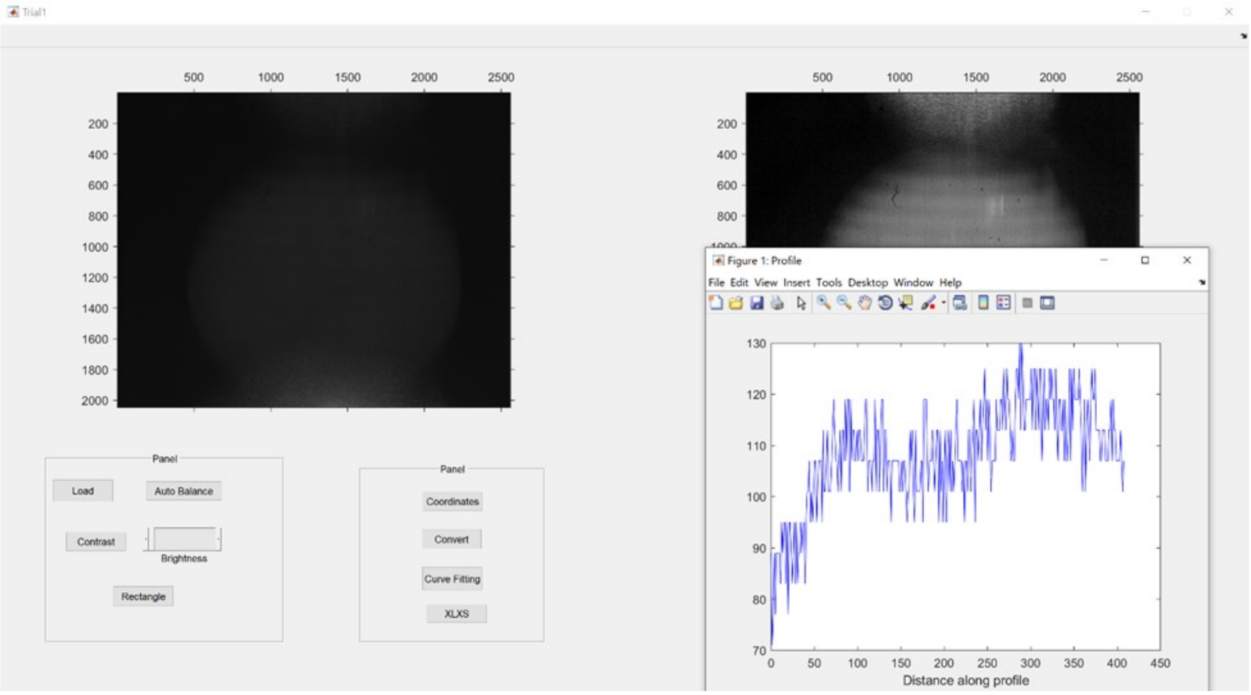

Figure A.2.: The graph at the bottom right corner showing the generated phase function curve. The noise in the curve appears from the stray light rays, reflection from the glass and surface of the dispenser tip, and the surrounding environment.

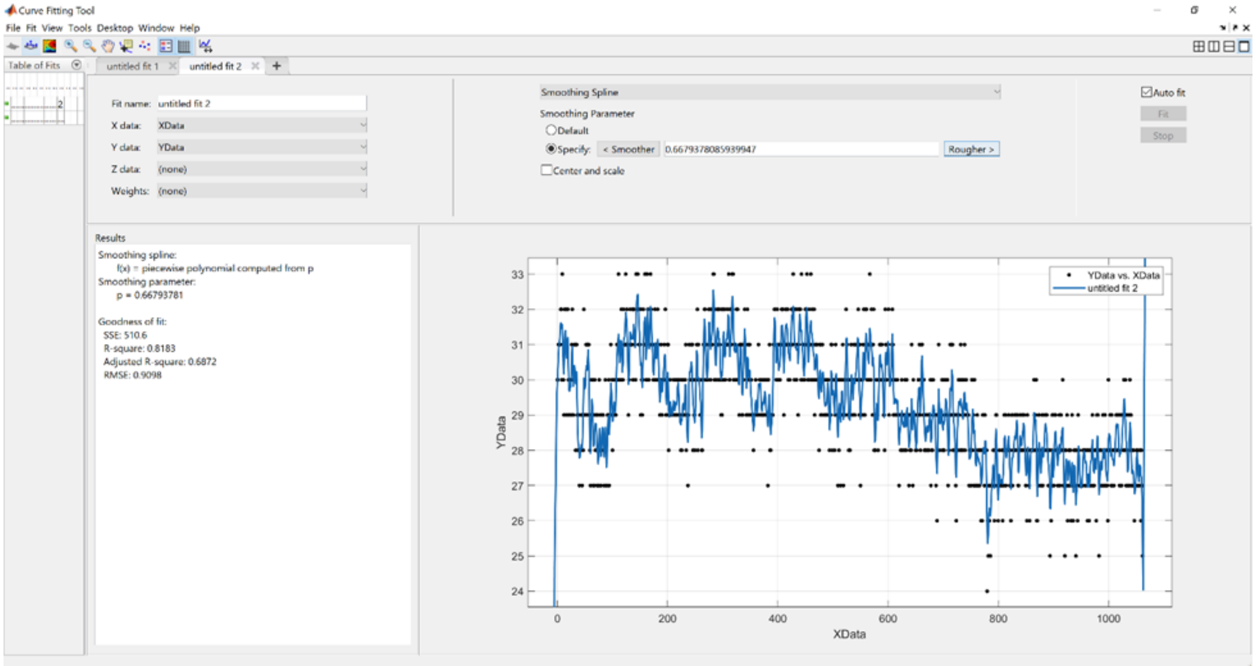

Fit name: untitled fit 2
X data: XData
Y data: YData
Z data: (none)
Weights: (none)

Smoothing Parameter
○Default
●Specify: 0.6679378085939947
☐Center and scale

Results
Smoothing spline:
f(x) = piecewise polynomial computed from p
Smoothing parameter:
p = 0.66793781

Goodness of fit:
SSE: 510.6
R-square: 0.8183
Adjusted R-square: 0.6872
RMSE: 0.9098

Figure A.3.: MATLAB Curve Fitting Tool panel used for processing the phase function curve.

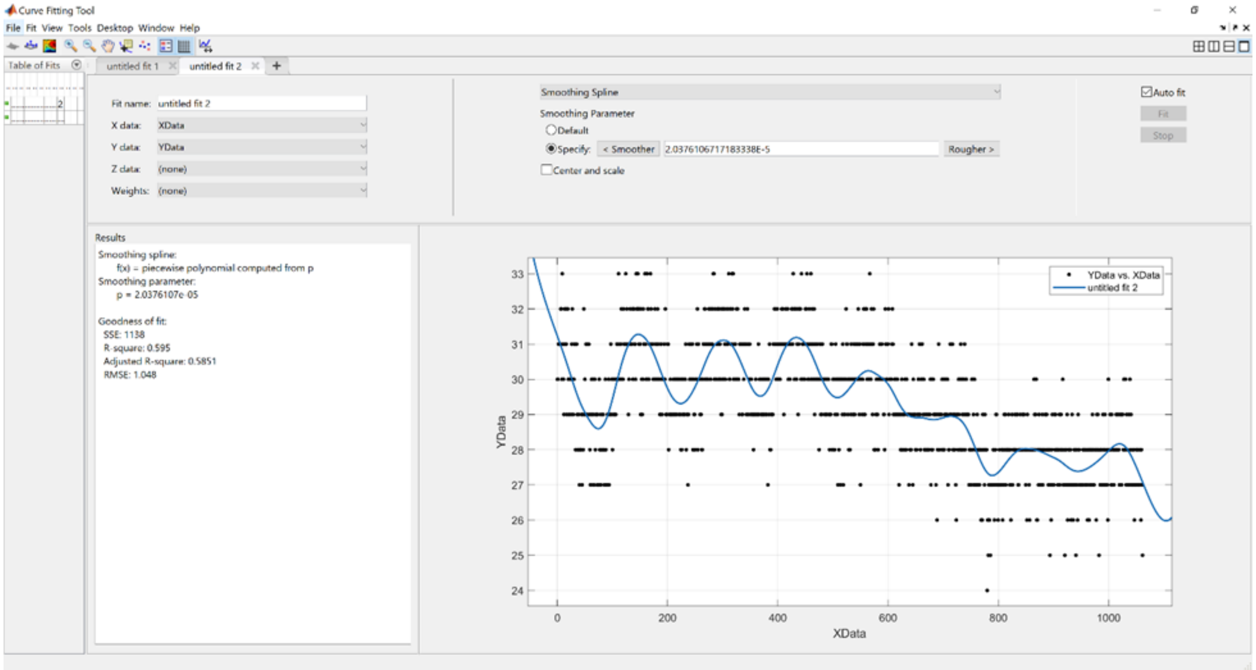

Fit name: untitled fit 2
X data: XData
Y data: YData
Z data: (none)
Weights: (none)

Smoothing Parameter
○Default
●Specify: 2.0376106717183338E-5
☐Center and scale

Results
Smoothing spline:
f(x) = piecewise polynomial computed from p
Smoothing parameter:
p = 2.0376107e-05

Goodness of fit:
SSE: 1138
R-square: 0.595
Adjusted R-square: 0.5851
RMSE: 1.048

Figure A.4.: Phase function curve post-processing. The smoothing spline function is used to generate the processed curve. The differences between adjacent maxima can be visualized in the panel and are later used to calculate the angular distance between the fringes.

Table A 2: Calculation of initial droplet diameter of water droplets generated in the droplet chain using a 40 μm piezoelectric dispenser. A drying gas flow rate of 3 L/min was maintained at 21 ˚C. A sample size of *n* = 50 was considered for calculation.

Scattering Angle (θ)	Distance Between Consecutive Maxima (Pixels)					Mean Distance (Pixels)	Standard Deviation	Mean Diameter (μm)	Mean Standard Deviation (μm)	Standard Deviation (%)
43˚	125	125.6	124.8	125	125	125.45	0.51	34.35	0.14	0.41%
	125.6	125.5	125	125.8	126.3					
	126.5	126	125	125.8	125.3					
	125.9	125.5	125.3	126.2	126					
	124.9	125	125.8	125.3	125					
	125	125.6	125.2	125.8	125					
	126	125.4	124.5	126.6	126					
	126.5	125.8	125.1	124.7	125.8					
	124.6	125.8	124.8	125	126					
	124.7	125	126	124.2	125.9					

Table A 3: Nozzle diameter (D_j), designed cutoff diameter $(d_{a,50})_d$, measured cutoff diameter $(d_{a,50})_m$ and Reynolds Number (Re) for a gas flow of 3 L/min through the single-nozzle impactor.

Stage	Gas Flow Rate, Q (L/min)	Nozzle diameter (D_j) (mm)	Designed cutoff diameter $(d_{a,50})_d$ (μm)	Measured cutoff diameter $(d_{a,50})_m$ (μm)	Reynolds Number (Re)
0		**4.95**	**21.4**	**8.6**	**850**
1		**3**	**9.92**	**4.1**	**1403**

2	**3**	**2.4**	**7.08**	**2.9**	**1754**
3		**1.9**	**4.96**	**2**	**2216**
4		1.65	4	1.6	2551
5		1.4	3.11	1.3	3007
6		1.2	2.45	1	3508
7		1	1.84	0.8	4210
8		0.85	1.43	0.6	4952
9		.7	1.05	.4	6014
10		.6	0.85	.3	7016
11		.5	0.60	.2	8419

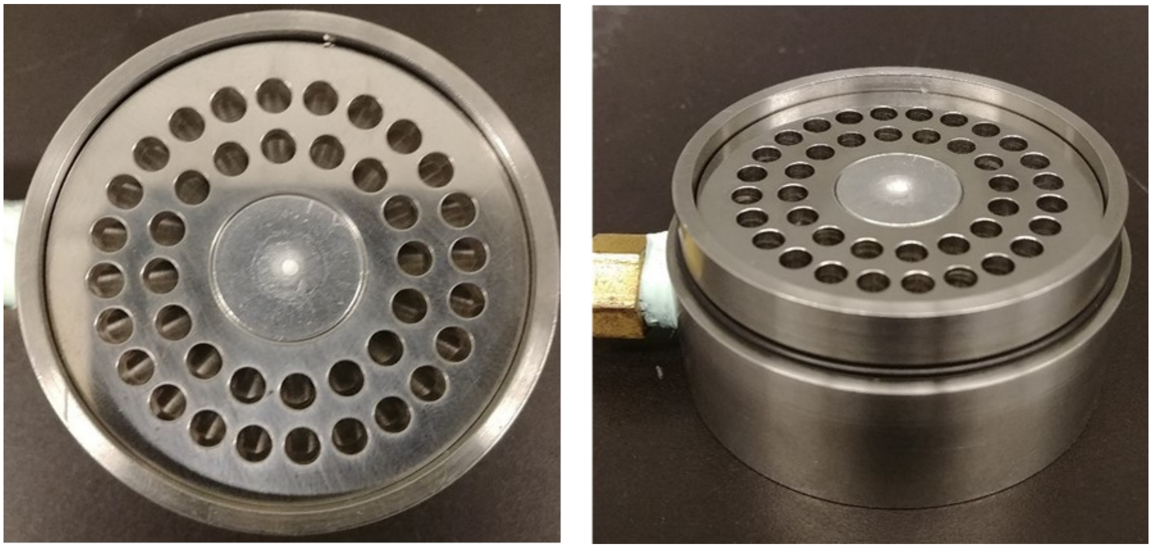

Figure A.5: Top and side views of the collection plate of Stage 2 of the single-nozzle impactor showing trehalose particles collected on the surface of an SEM stub.

Appendix B: Supplemental Data from Feasibility study of Spray-Dried Eudragit-Trehalose Microparticles for Enteric Delivery of Biologics

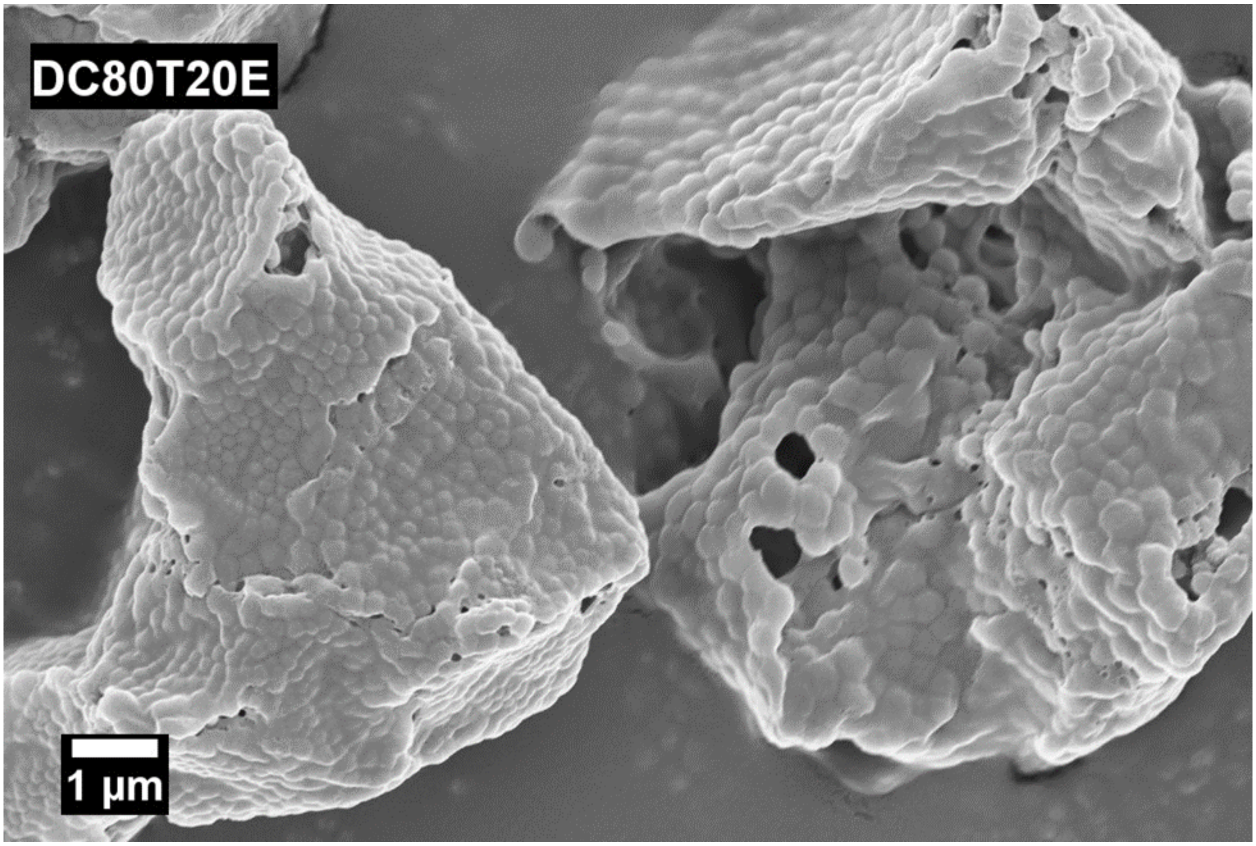

Figure B.1.: High-magnification scanning electron microscopy image of formulation DC80T20E collected from the monodisperse droplet chain at 21 ˚C prepared in an isocompositional mixture of water and ethanol. The components appear to form small colonies within the particles, which can possibly be explained using the theory of spinodal decomposition.

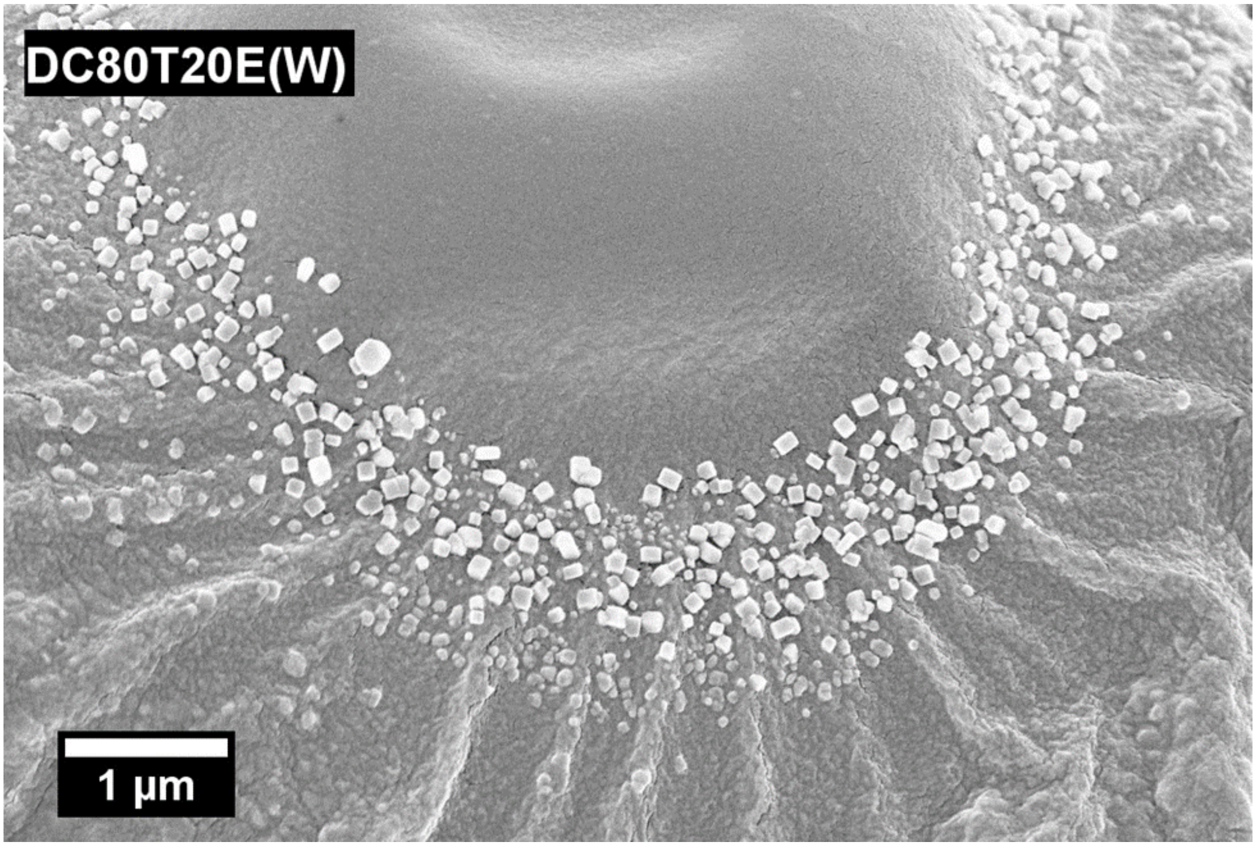

Figure B.2.: High-magnification scanning electron microscopy image of formulation DC80T20E(W) collected from the monodisperse droplet chain at 21 ˚C prepared in water by dissolving the components using a pH-shifting technique. The particle surface shows the presence of sodium chloride crystals, which are the byproduct of the neutralization reaction to balance the pH of the solvent.

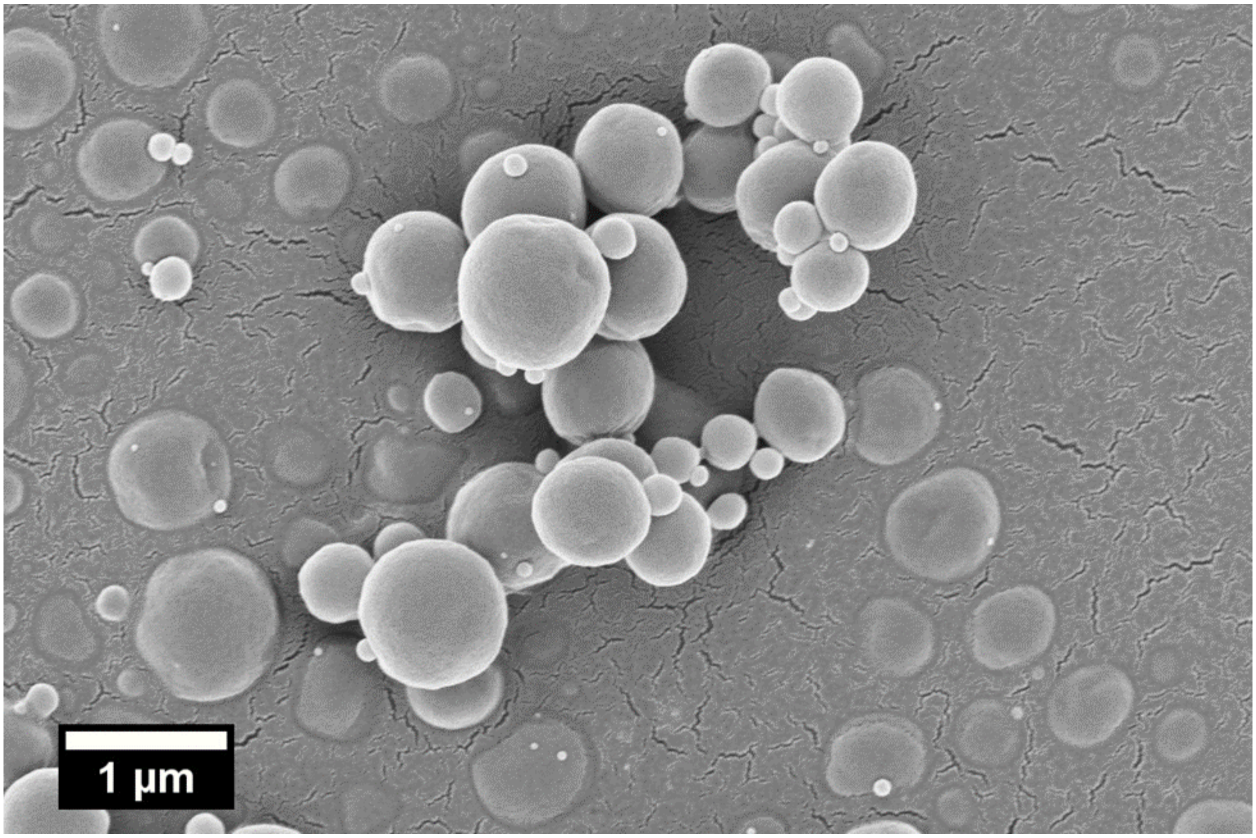

Figure B.3.: Scanning electron microscopy image of spray-dried formulation SD80T20E prepared in an isocompositional mixture of water and ethanol at 100 ˚C. The particles are small and show no visible surface roughness features, a phenomenon that might be due to faster evaporation of the droplets and the absence of sodium chloride crystals.

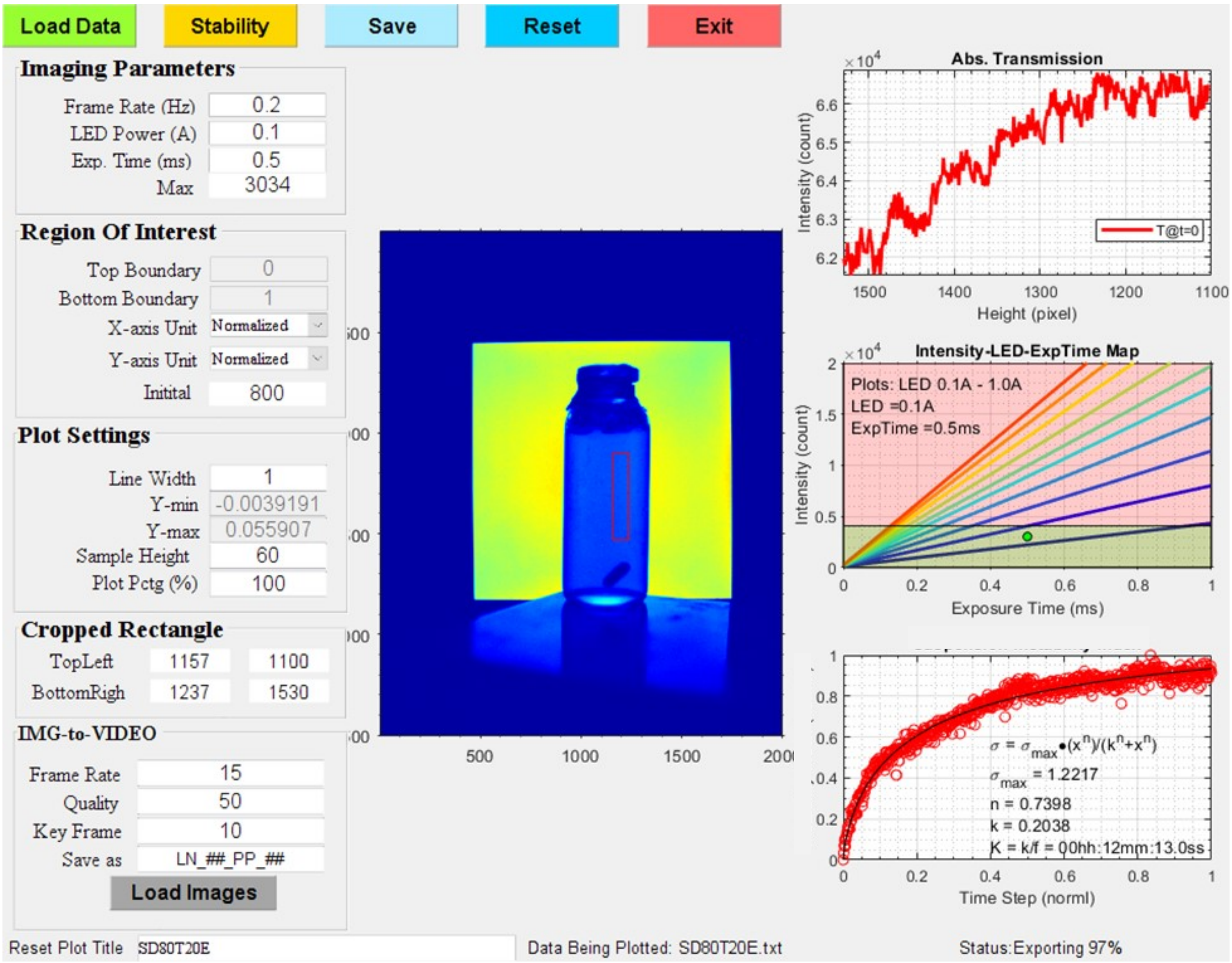
Imaging Parameters
Frame Rate (Hz) 0.2
LED Power (A) 0.1
Exp. Time (ms) 0.5
Max 3034

Region Of Interest
Top Boundary 0
Bottom Boundary 1
X-axis Unit Normalized
Y-axis Unit Normalized
Initital 800

Plot Settings
Line Width 1
Y-min -0.0039191
Y-max 0.055907
Sample Height 60
Plot Pctg (%) 100

Cropped Rectangle
TopLeft 1157 1100
BottomRigh 1237 1530

IMG-to-VIDEO
Frame Rate 15
Quality 50
Key Frame 10
Save as LN_##_PP_##

Reset Plot Title SD80T20E
Data Being Plotted: SD80T20E.txt
Status:Exporting 97%

Figure B.4.: Data panel after processing the shadowgraphic images. The left side of the panel shows the processing parameters and data of selected region of interest to generate the absolute transmission, light intensity map and transmission coefficient graphs as shown on the right.

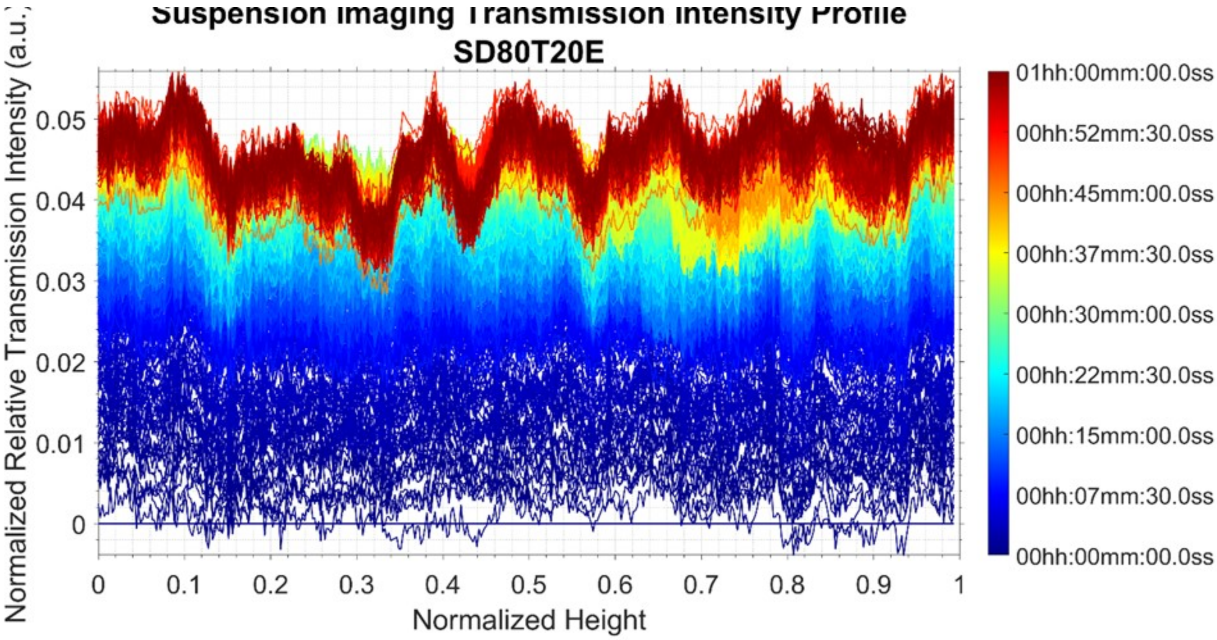

Figure B.5.: Normalized relative transmission intensity graph for spray-dried formulation SD80T20E suspended in an acidic solution of pH = 2 for one hour. Relative transmission intensity increases as time passes, indicating a decrease in density of particles in the suspension.

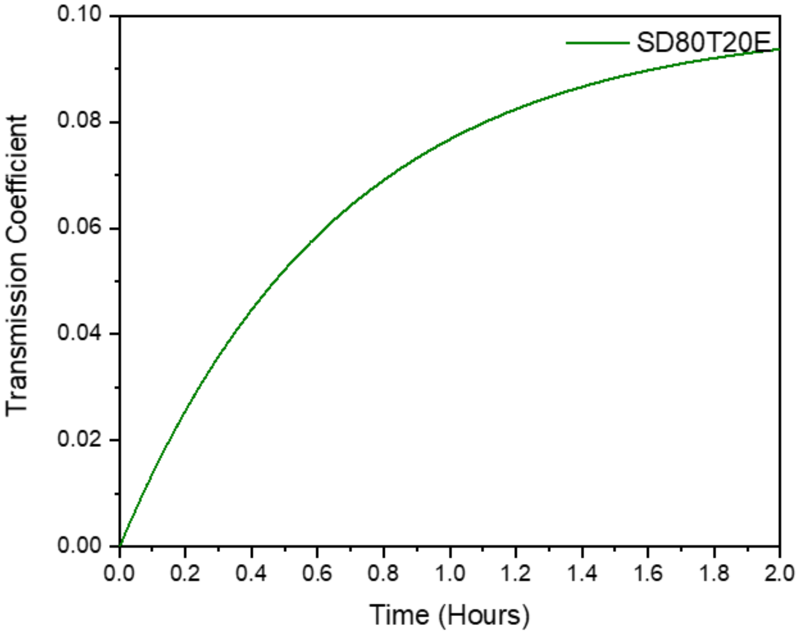

Figure B.6.: Graph showing the transmission coefficient of spray-dried formulation SD80T20E suspended in an acidic solution of pH = 2 for one hour. A gradual increase in the transmission coefficient gives a qualitative indication of loss of particles in the medium.

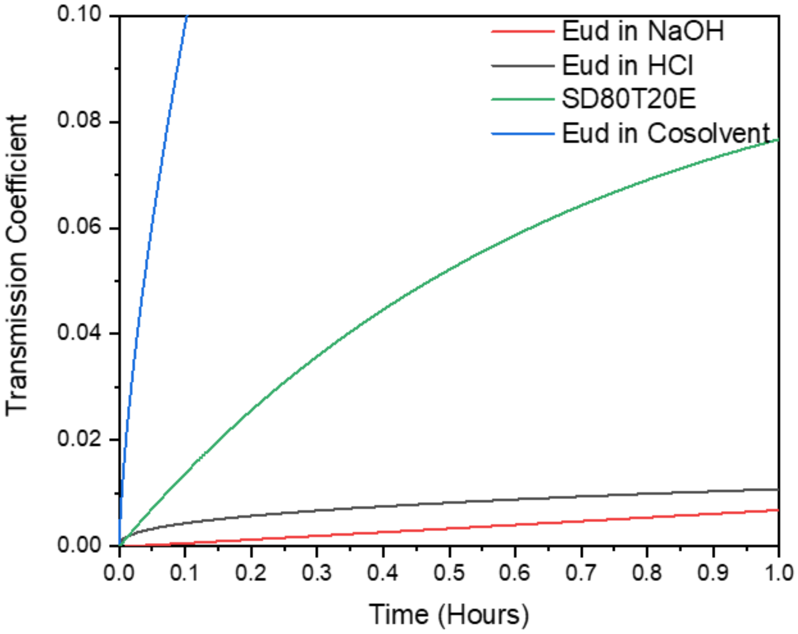

Figure B.7.: Comparison of transmission coefficients of Eudragit in different media. Because of its pH-dependent delayed dissolution property, Eudragit dissolves slowest in a sodium hydroxide solution, which is evident from the smallest change in transmission coefficient. The transmission coefficient of the hydrochloric acid solution is slightly higher, indicating corrosion of Eudragit granules in the medium. The transmission coefficient in a co-solvent system is the highest as Eudragit has high solubility in ethanol.